Certification and Design for Manufacture of Curved and Tapered Laminates

Fletcher, Timothy

Award date:
2017

Awarding institution:
University of Bath

Certification and Design for Manufacture of Curved and Tapered Laminates

Submitted by

Timothy A. Fletcher

for the degree of Doctor of Philosophy

University of Bath

Department of Mechanical Engineering

November 2016

Abstract

This thesis explores the manufacture and certification of composite laminates, which pose interesting challenges, unique to their anisotropic, layered design. The aerospace industry is using composite materials more extensively with each new generation of aircraft, and there is a need to reduce cost and increase rate of production, particularly going forward with smaller, short-range airliners.

A C-section laminate with novel, anti-symmetric stacking sequences is designed and manufactured using automated fibre placement (AFP) and autoclave cure. The layup is designed to improve consolidation and reduce warpage, whilst minimising the requirement for interim de-bulking. It is shown not only that anti-symmetric laminates can be successfully industrially manufactured, but that they provide significant potential benefit over more conventional balanced, symmetric laminates. Compared against such a baseline, the novel laminate is found to increase consolidation by 8.7% and achieve a cured ply thickness closer to the nominal value quoted by the manufacturer. It is also found to reduce twisting warpage by 48%. The use of an anti-symmetric layup is key to this success, since there are found to be more than an order of magnitude more fully uncoupled anti-symmetric sequences than symmetric. The increased design space allows for a 'protected zone', into which plies that would otherwise restrict consolidation are positioned.

Industrial components are typically certified by testing narrow witness specimens, cut from their ends. These specimens have exposed free edges, which have been found to significantly reduce the 3D strength. This is known as the edge effect and means this certification method does not truly represent the full-size component, which is typically very wide and built into surrounding structure. A new treatment process is developed, whereby a layer of resin is applied to the free edges. This significantly reduces the edge effect, increasing strength by as much as 22% and improving the repeatability of experimentally tested laminates. Accurate prediction of resin treated laminate strength is achieved by modelling finite-thickness interface layers between plies, and using a combination of Camanho and Christensen failure criteria.

Acknowledgements

This work has been supported by a University Research Studentship (URS) from the University of Bath and additional funding from GKN Aerospace. I am also grateful to employees of GKN Aerospace for supplying materials and facilitating the use of industrial equipment.

I have been fortunate to have many friends at Bath, especially the members of Richard's composites group, making my time there very enjoyable. I am grateful for the excellent technical assistance from Stephen Thomas, Nick Gathercole and Andy Francis. Most of all, I owe a great deal of thanks to my supervisors, Prof. Richard Butler and Prof. Giles Hunt, whose knowledge and wisdom has been invaluable.

I would also like to express a huge thank you to my parents, sister Fiona, and Charlotte. I am very lucky to have their incredible support, and when necessary patience, allowing me the freedom to pursue my interests.

Contents

List of Figures

Chapter 2

Chapter 3

Chapter 4

Chapter 5

Chapter 7

List of Tables

Chapter 4

Chapter 5

Nomenclature

Abbreviations

AFP	Automated fibre placement.
CFRP	Carbon fibre reinforced plastic.
CPT	Cured ply thickness.
CT	Computed tomography.
FE(A)	Finite element (analysis).
FIL	Fully isotropic laminate.
GFRP	Glass fibre reinforced plastic.
GUI	Graphical user interface.
HDD	Hard disk drive.
HTCS	Hygrothermally curvature stable.
NDI/T	Non-destructive inspection/testing.
PZ	Protected zone.
RAM	Random access memory.
RT	Resin treatment.
SD	Standard deviation.
SSD	Solid state drive.

Characters and Symbols

It is unavoidable that in some cases the same characters are assigned to different variables, or that the same variable is assigned a different character in different sections of the thesis. The meaning should always be clear from the context however.

$\boldsymbol{A}$	Laminate in-plane (membrane) stiffness matrix.
$\boldsymbol{B}$	Laminate coupling stiffness matrix.
c	Consolidation as a proportion of pre-consolidation laminate thickness.
$\boldsymbol{D}$	Laminate bending (out-of-plane) stiffness matrix.
E	Elastic modulus.
G	Shear modulus.

l	Length.
$M_{\square}$	Moment.
N	Total number of plies in a laminate.
$N_{\square}$	Force.
$\boldsymbol{Q}$	In-plane stiffness matrix in local ply co-ordinate system.
$\overline{\boldsymbol{Q}}$	In-plane stiffness matrix in global laminate co-ordinate system.
R	Ramp rate of tapered laminate.
$\boldsymbol{T}$	Transformation matrix to convert between local and global co-ordinate system.
t	Thickness.
U	Number of fully uncoupled sequence vectors.
y	Vertical position relative to tool surface in pad-up region.
z	Through-thickness distance between reference plane and top of layer.
$\bar{z}$	Through-thickness distance between reference plane and layer mid-plane.
α	Opening angle of curved laminate.
β	Size of sequence vector (number of rows).
ε	Strain.
ρ	Through-thickness distance as proportion of total laminate thickness.
σ	Direct stress.
τ	Shear stress.
ϕ	Angle between fibres in a ply and global reference axis.
$\boldsymbol{\varphi}$	Number of possible entries per row of sequence vector.
$+$	Positive angle-ply.
$-$	Negative angle-ply.
○	90° cross-ply.
●	0° cross-ply.

Subscripts

$\square_{1,\,2,\,3}$	Local ply co-ordinates, 1 is fibre direction, 2 is transverse to fibres (in-plane) and 3 is out-of-plane.
$[...]_2$	2 (3, 4 etc.) multiples regarding stacking sequence.
$[...]_{\mathrm{A}}$	Repeated anti-symmetrically regarding stacking sequence.
$\square_A$	Anti-symmetric sequences.
$\square_f$	Far-field laminate.

$\square_{fib}$	Fibrous layer.
$\square_{fib+int}$	Fibrous and resin interface layer combined.
$\square_{int}$	Resin interface layer.
$\square_{k}$	k^{th} layer.
$\square_{p}$	Pad-up laminate.
$\square_{post}$	Post-consolidation.
$\square_{pre}$	Pre-consolidation.
$\square_{r}$	Ramp of tapered laminate.
$\square_{r,\,\theta,\,l}$	Radial, tangential and length-direction in global cylindrical co-ordinates, applicable to curved laminates.
$[...]_{\text{S}}$	Repeated symmetrically regarding stacking sequence.
$\square_{S}$	Symmetric sequences.
$\square_{x,\,y,\,z}$	x, y, and z-direction in global cartesian co-ordinates.
$\square_{+}$	Positive angle-plies only.
$\square_{-}$	Negative angle-plies only.

1 INTRODUCTION

Innovation in engineered structures often comes from the use of new materials or using existing materials in a new, more efficient manner. Aircraft designs typically balance minimising the structural weight of an airframe against improving its aerodynamic profile. Early designs were commonly built from ply wood, with fabric forming an aerodynamic skin. There was a steady progression in the performance of gliders manufactured in such a manner, until the Schleicher Ka6E in 1965 for the 15m wingspan class. There was then a step change in performance for the Glasflügel Standard Libelle (1967) and Schempp-Hirth Standard Cirrus (1968) gliders, which were constructed from glass fibre reinforced plastic (GFRP): a composite material. The higher specific strength of the material allowed for thinner wing and fuselage sections, improving aerodynamics, especially at higher speeds. The introduction of metals, such as aluminium, produced durable, lightweight airframes for military aircraft and commercial airliners, such as the first production commercial jetliner: the de Havilland Comet, introduced in 1952.

High-performance carbon fibres were first produced in the late 1950s. The process was refined until in 1963 their significant strength potential was realised. Carbon fibre composites, in particular those with polymeric matrices, saw steadily increasing use in the decades following and have become the dominant advanced composite material within the aerospace industry, as well as a wide range of other applications. Their attractive mechanical properties include high in-plane strength and modulus, particularly in relation to their weight. The manufacture of carbon fibre reinforced plastic (CFRP) laminates consists of building up layers of material in an additive process, rather than machining stock material down to shape and size, as is common practice for metals. This results in significantly less waste material. CFRP is also more corrosion resistant, which is also highly desirable to commercial airline companies since it has been estimated almost 25% of the life cycle cost of an aircraft can be attributed to inspection and maintenance [1].

There are stringent certification requirements and the aerospace industry exercises caution when introducing new materials and technologies, owing to the potentially severe consequences should an airframe structure fail. There has therefore been a conservative, incremental increase in use of composite materials from generation to generation of large commercial airliners, culminating in a step change for the latest large commercial aircraft to enter service: the Boeing 787 Dreamliner and Airbus A350 XWB. These long-range aircraft are built from, respectively, 50% [2] and 53% [3] composite materials by weight. Significantly, primary structures of the wings and fuselage are built from CFRP.

Where possible, the integrity of a laminate is verified by means of non-destructive inspection and testing (NDI/NDT). This allows all manufactured components to be checked for defects. In certain cases, however, the performance and integrity must be proven by means of a destructive test. The strength of large laminated components is commonly certified by the extraction of witness specimens from the ends of the component, outside engineering edge of part: the section that will eventually fly on the aircraft. As a representative section of the component, these specimens are then put in a rig and tested to destruction. The relatively narrow specimens have exposed free edges where they are cut. This is not the case for the production part, which is commonly built into surrounding structure at its ends. Failure during test of the narrow specimens typically initiates at the free edges, significantly reducing the strength of the 3D part, as compared with the 2D (plane strain) analysis that effectively does not have free edges. The narrow specimens are therefore not fully representative of the production part and this method of certification is unreasonably conservative.

The singularity at the free edge makes FE analysis challenging. Since failure is dominated by the free edge, studying the influence of defects in narrow test specimens is also difficult. A new treatment process is developed in this thesis, whereby a thin layer of resin is applied to the free edges of test specimens. The free edge effect is driven by the fact that stresses normal to the free edge surface must become zero at the free edge. The resin edge treatment mitigates this by providing support and allowing for non-zero stress components in this direction. The effect and overall benefit of the resin treatment is explored both by computational analysis and experimental testing.

The in-service benefits of CFRP are well documented; however, another significant cost driver is the manufacturing process. This is relatively complex, involving various stages before producing a finished composite component. Modern

automated fibre placement (AFP) machines commonly use tows of fibres that have been pre-impregnated with the matrix material that binds the fibres together during cure. This material, known as prepreg, is laid onto a mould in such a way as to create the desired laminate shape, thickness and fibre orientation. Typically at interim stages during the lay-up, the laminate is de-bulked: removing trapped air and compacting the layers of prepreg together. Regular de-bulking adds significant time and cost to the process but is used to help control the movement of material and avoid defects, such as fibre wrinkling and voids, especially for large laminates with complex geometry. Once the lay-up process is complete, the laminate is cured at elevated temperature, typically in an autoclave with the laminate enclosed in a vacuum bag and external pressure applied.

The manufacturing process therefore causes significant changes in the laminate, from thermal expansion and contraction, to movement of material as it conforms to the shape of the mould tool surface. If not carefully managed, this can lead to defects in the laminate, potentially requiring large components to be scrapped at the cost of hundreds of thousands of pounds. There are many forms that defects can take, including: resin rich zones, where the fibre and matrix material are not evenly distributed throughout the material; voids, where pockets of trapped air are not properly removed during de-bulk; fibre wrinkles, which weakens and reduces stiffness of the laminate as the fibres are not properly aligned in the desired direction; poor consolidation, where the material does not compact sufficiently to reach the nominal cured ply thickness; and warpage, which can take many forms, such as the bending or twisting of a laminate out-of-plane, resulting in a deformed shape without the desired performance characteristics.

The tendency of a laminate to warp as a result of thermal and moisture changes is highly dependent on the stacking sequence: the order in which plies with fibres in different orientations are stacked together to form a laminate. This is as a result of the strong contrast between mechanical properties parallel to the fibre direction, and those transverse to the fibre direction. A common industrial practice is to use symmetric stacking sequences. This removes the coupling between in-plane deformations, which can for example be caused by thermal expansion, and out-of-plane deformations: bending and twisting. Balanced laminates are those with an equal number of negative angle-plies and positive angle-plies, removing the tendency to shear as a result of extensive load or vice versa. Balanced, symmetric laminates therefore exhibit relatively benign behaviour overall, by removing the majority of the coupling terms between

different types of deformation: extension, shearing, bending and twisting. Coupling these makes performance analysis more complex but can be desirable for certain applications, such as altering the angle of attack of helicopter rotor blades at different rotor speeds. It is possible to design stacking sequences that are non-symmetric or that couple different forms of deformation, yet do not warp during manufacture. Such laminates are said to be hygro-thermally curvature stable (HTCS). The requirement for a stacking sequence to be symmetric severely restricts the design space. It is found in this thesis, for a given number of plies, there are typically an order of magnitude more fully uncoupled anti-symmetric stacking sequences than there are symmetric. Anti-symmetric stacking sequences require a positive angle-ply to be mirrored by a negative angle-ply and vice versa, whereas symmetric stacking sequences require a positive angle-ply to be mirrored by a positive angle-ply. The benefits of a fully uncoupled anti-symmetric laminate are shown theoretically and experimentally, by the design and manufacture of a novel demonstrator laminate, compared against a balanced, symmetric baseline laminate.

The level of consolidation during manufacture is partly dependent on various process parameters, such as interim de-bulks, autoclave pressure, temperature and cure time. However, the design of the laminate stacking sequence can also influence the tendency of a laminate to conform to the tool surface and consolidate well, in particular for laminates with complex geometry. It is common for aerostructures to change thickness along their length in order to accommodate stress concentrations, such as landing gear and engine attachment points along the wings. This is simulated by the inclusion of tapered regions in the demonstrator laminate design in this thesis. It is believed, from analysis, that long fibres running the full length of a component, through tapered regions, are generally most resistant to consolidation movement and restrict conformity to the tool surface. Plies oriented in this way are defined as 0° plies. A 'protected zone' in the stacking sequence is developed, into which all long 0° plies are positioned for the novel demonstrator laminate. The effect on consolidation behaviour is then observed and compared with the baseline laminate. The resistance of 0° plies becomes more significant the greater the movement during a single de-bulk. This can be partly mitigated by including regular interim de-bulks as each layer of the laminate is laid down, reducing the movement per de-bulk; however, this adds significant time and cost to the manufacturing process and so is undesirable.

The in-service performance, such as low fuel burn, is more important for long-range aircraft than it is for smaller, short-range aircraft. The time taken to perform

the manufacturing process becomes more critical for large production volumes, typical of smaller commercial aircraft, the size of the Boeing 737 and Airbus A320 families. Although the 787 and A350 aircraft do represent an improvement comparted with their predecessors, the full potential of composite materials has not yet been realised. Further improvements in manufacturing processes and reduction of airframe weight are possible, with a subsequent reduction in manufacturing and operating costs.

1.1 Scope

There are two facets of composite laminates considered in this work: their manufacturability and their performance. These are both affected by many factors and can be measured against various metrics. It is therefore necessary to focus on particular aspects within manufacture and performance and, as such, the findings presented in this work should form part of a wider design consideration when developing composite laminates.

This thesis sets out to understand how the design of laminates can improve their manufacture, by achieving good consolidation and minimising warpage. In particular, the effect of laminate stacking sequence on the behaviour of tapered laminates and complex (non-flat) geometries is to be considered. The performance of curved laminates is assessed experimentally by means of a 4-point bending test in the context of industrial component certification, with subsequent analysis of the influence of laminate stacking sequence.

The effect of exposed free edges on the strength of narrow, curved laminate specimens is explored. A resin treatment for minimising this effect is developed, with the aim of aiding certification of composite laminates using witness specimens. Modelling of the 4-point bending test and strength prediction is to be applicable to different laminate geometries and stacking sequences. To show the resin treatment can be applied more generally, to different laminates geometries, an analysis of flat laminates with and without treatment is conducted to complement the primary work, which is focused on curved laminates.

1.2 Objectives

The following objects are set to fulfil the scope of the thesis:

1. Identify key factors relating to laminate design that impact the consolidation and warping behaviour during manufacture.

2. Investigate the special properties of symmetric and anti-symmetric stacking sequences, with regard to uncoupling the stiffness matrix and designing laminates that do not exhibit a tendency to warp during manufacture.

3. Manufacture a laminate according to novel design rules, specifically intended to improve consolidation and reduce warp; alongside a baseline, designed according to typical industrial practices.

4. Identify the mechanism causing the edge effect and develop a technique or edge treatment that minimises its influence on specimen strength.

5. Experimentally test laminates with and without the edge treatment, in order to assess its success or otherwise.

6. Develop a model that predicts the 4-point bending strength of curved laminates with the newly developed edge treatment and compare accuracy against experimental results.

7. Assess the overall advantages and disadvantages of the novel laminate design with regard to manufacturability and performance.

1.3 Thesis Overview

This section provides an overview of each Chapter and its content, as a reference to help guide the reader towards areas of specific interest.

Chapter 2: Manufacture

In this chapter, the influence of stacking sequence on the stiffness coupling of a laminate is explored. Stiffness coupling has a strong influence over the tendency of a laminate to warp during the temperature changes of manufacture and is therefore an important consideration to fulfil Objective 1. Formulas for fully uncoupling symmetric and anti-symmetric laminates are developed, as well as for specific industrial applications, fulfilling Objective 2. The geometrical effects in tapered laminates are found to affect consolidation behaviour, and are therefore an important part of fulfilling Objective 1. The design of a 'protected zone' is developed and stacking sequences that accommodate this, as well as being fully uncoupled, are generated for a novel demonstrator laminate. This is subsequently manufactured alongside a more conventional baseline laminate, fulfilling Objective 3. Finally, a co-ordinate measuring machine (CMM) is used to record laminate geometry before and after the de-bulking and curing processes, in order to assess the manufacturability of the novel design as part of Objective 7.

Chapter 3: Corner Unfolding

4-point bending tests in the context of curved laminate certification are introduced. Experimental test results for curved laminate specimens without free edge treatment are presented as part of Objective 5. Analytical and numerical models for the prediction of curved beam strength (CBS) are reviewed and developed, including the selection of a suitable failure criterion (referred to as Camanho failure criterion), as a precursor to Objective 6. However, it is found that the free edge effect dominates the performance of narrow test specimens without edge treatment, making analytical models unsuitable and causing a numerical singularity that makes FE modelling challenging.

Chapter 4: Edge Effect and Treatment

The initiation of failure of curved laminate specimens from the free edge is investigated and an explanation for this edge effect is presented, as part of Objective 4. Techniques proposed in the literature for the mitigation of the edge effect are reviewed. These have been applied primarily to flat laminates and many are unsuitable for retrospective application to witness specimens cut from larger production parts for component certification. Two original free edge protection treatments are developed. A resin edge treatment proves to be most suitable and is applied to a range of specimen types, fulfilling Objective 4. These treated specimens are experimentally tested and the results compared with untreated results from Chapter 3, completing Objective 5. Finally, the FE model and failure prediction is improved, using two failure criteria: Camanho criterion identified in Chapter 3, and Christensen failure criterion. This results in a conservative but accurate prediction of all specimen types with resin edge treatment, fulfilling Objective 6. The level of defects within the experimental specimens is also presented.

Chapter 5: Analysis of Resin Treated Laminates

The effect of the resin treatment on near-edge stresses is analysed in more detail, with varying resin mechanical properties. The confidence in the FE modelling is assessed with a series of sensitivity studies. It is noted that for particular specimen types and resin edge material, failure of the resin edge may occur first, rather than failure initiating within the CFRP laminate. Failure of the resin edge is an important consideration and an alternative resin edge material that delays failure is analysed and tested experimentally. Results are compared against a baseline (untreated) laminate and a laminate treated with the resin used in Chapter 4. The broader applicability of the resin edge treatment, beyond curved laminates subjected to 4-point bending, is shown by FE analysis of flat laminates subjected to axial loading, which is in line with the case presented in the literature for other edge protection techniques.

Chapter 6: Discussion

Key aspects of the work presented in this thesis are highlighted and discussed. The overall manufacturability and performance of the novel laminate design is discussed, as compared against the more typical industrial design, completing Objective 7.

Chapter 7: Conclusion

The most notable and interesting findings of this thesis are summarised. The success of the novel laminate design is discussed, with regard to improving manufacturability and performance. The benefits of the newly developed resin edge treatment are highlighted, together with the modelling and analysis methods, which provide a means for predicting the strength of treated specimens. A few potential avenues for future work are also briefly explored.

1.4 Work Undertaken by Author

This section outlines the work that was carried out independently by the author of this thesis. It also details how other parties were involved in supporting the author's research.

Manufacture of Composite Laminates

The author personally performed hand layup of prepreg material for an investigation into the behaviour of prepreg during the curing process. The cure was performed in the autoclave at The University of Bath, operated by Stephen Thomas, who also assisted with the vacuum bagging.

The design of the demonstrator laminate stacking sequences and drop-off pattern was produced independently by the author. The layup and cure of the material was performed using industrial equipment at the National Composites Centre, operated by NCC staff.

CMM Data

The author discussed the requirements for the measurements with Andy Francis. The CMM machine was operated by Andy Francis, who also gathered the raw data and presented it in spreadsheet format. The author then extracted the relevant data in order to determine the laminate thickness, consolidation, spring-in and twist.

Experimental Testing

For the investigation into the behaviour of prepreg during the curing process, the author designed a bespoke test rig. The author sourced the raw materials and personally carried out the machining process, under the supervision of technicians at The University of Bath.

Specimens were cut to size for 4-point bending by Nick Gathercole, to the author's specification. The author designed the 4-point bend rig. Manufacture of the rig was performed by Nick Gathercole and technicians at The University of Bath. The rig was then used by the author, who personally tested all G39, S24, S44, N24 and N44 specimens, initially under the supervision of Nick Gathercole until the author became

familiar with the equipment. The G64 specimens were tested by staff at Exova plc, under the supervision of the author.

Resin Edge Treatment

Plasma treatment (to prepare the edges of specimens for application of resin) was performed by staff at the NCC, under the guidance of the author. Initially, the resin was then applied to the specimens by the author. Once the process had been developed, later specimens were treated either by Stephen Thomas at The University of Bath, or staff at GKN Aerospace.

Visualisation and Scanning

Grinding of the specimens (for micrograph preparation) was performed by the author, as was operation of the microscope, both initially under the supervision of Nick Gathercole until the author became familiar with the equipment.

The X-ray CT scanner was operated by Clare Ball at The University of Bath, in order to capture the raw data. The data was then processed by the author using Avizo software to analysis the specimens and produce images.

Analysis

All Matlab scripts used to find fully uncoupled stacking sequences and to generate the demonstrator laminate stacking sequences and drop-off patterns, were created by the author. The FE models of curved laminate specimens were also created and analysed by the author, as were the Python scripts used to manipulate the models.

1.5 Publications

The work presented in this thesis has been formed from a number of papers that have been published in international journals and conference proceedings.

The following papers have been published in international journals:

- Fletcher TA, Kim T, Dodwell TJ, Butler R, Scheichl R, Newley R. Resin treatment of free edges to aid certification of through thickness laminate strength. Composite Structures 2016; 146: 26-33.
- Fletcher TA, Butler R, Dodwell TJ. Anti-symmetric laminates for improved consolidation and reduced warp of tapered C-sections. Advanced Manufacturing: Polymer and Composite Science 2015; 1(2): 105-111.

The following papers have been published in conference proceedings:

- Fletcher TA, Reinarz AK, Dodwell TJ, Butler R, Scheichl R, Newley R. Efficient modelling and accurate certification of curved aerospace laminates. In: Proceedings of the 17th European Conference on Composite Materials (ECCM17), Munich, Germany, 26-30 June 2016.
- Fletcher TA, Butler R. The influence of free edges on curved beam strength. In: Proceeding of the 20th International Conference on Composite Materials (ICCM20), Copenhagen, Denmark, 19-24 July 2015.
- Kim T, Fletcher TA, Dodwell TJ, Butler R, Scheichl R, Ankersen J, Newley R. The effect of free edges on inter-laminar performance of curved laminates. In: Proceedings of the 56th AIAA/ASCE/AHS/ASC Structures, Structural Dynamics, and Materials Conference, Kissimmee, Florida, USA, 5-9 January 2015.
- Fletcher TA, Butler R, Dodwell TJ, Erland S. Non-symmetric stacking sequences to aid manufacture. In: Proceedings of the 16th European Conference on Composite Materials (ECCM16), Seville, Spain, 22-26 June 2014.

1.6 Industrial Impact

Development of a resin edge treatment is presented in this thesis. The treatment protects the exposed free edges of witness specimens, used to certify the strength of the production components from which they are extracted. As well as increasing specimen strength, making it a closer representation of the full-size part, the repeatability of experimental testing is improved, meaning there are fewer weak outliers. This work is aiding certification in industry, in particular by reducing the number of concessions.

> *"GKN will benefit from reduction in concessions. We will save in the value of assets to be sacrificed for future test programmes. Through this understanding of numerical correlation with failure criterion, GKN is positioned to drive method improvement which will bring benefits to wider supply base of our customer."*
> Vijay Sahadevan, Stress Technical Authority, GKN Aerospace [4].

2 MANUFACTURE

In this chapter, the influence of stacking sequence on the stiffness coupling of a laminate is explored. Formulas for fully uncoupling symmetric and anti-symmetric laminates are derived, and the implications of industrial applications on stiffness coupling investigated. The effect of tapered regions on consolidation is also considered. From these theoretical studies, a novel anti-symmetric laminate is designed to increase consolidation and reduce warp, and subsequently manufactured alongside a baseline balanced, symmetric laminate. A co-ordinate measuring machine (CMM) is used to record laminate geometry before and after the de-bulking and curing processes, to assess the level of consolidation and warp for the two laminates.

2.1 Stacking Sequence

2.1.1 Laminate Stiffness Matrix

The well-known classical laminate theory is commonly used to describe the response to load of a laminate. It states that for a 3D Cartesian co-ordinate system in x, y and z,

$$\begin{bmatrix} N_x \\ N_y \\ N_z \\ N_{xz} \\ N_{yz} \\ N_{xy} \\ M_x \\ M_y \\ M_z \\ M_{xz} \\ M_{yx} \\ M_{xy} \end{bmatrix} = \begin{bmatrix} A_{11} & A_{12} & A_{13} & A_{14} & A_{15} & A_{16} & B_{11} & B_{12} & B_{13} & B_{14} & B_{15} & B_{16} \\ & A_{22} & A_{23} & A_{24} & A_{25} & A_{26} & B_{12} & B_{22} & B_{23} & B_{24} & B_{25} & B_{26} \\ & & A_{33} & A_{34} & A_{35} & A_{36} & B_{13} & B_{23} & B_{33} & B_{34} & B_{35} & B_{36} \\ & & & A_{44} & A_{45} & A_{46} & B_{14} & B_{24} & B_{34} & B_{44} & B_{45} & B_{46} \\ & & & & A_{55} & A_{56} & B_{15} & B_{25} & B_{35} & B_{45} & B_{55} & B_{56} \\ & & & & & A_{66} & B_{16} & B_{26} & B_{36} & B_{46} & B_{56} & B_{66} \\ & & & & & & D_{11} & D_{12} & D_{13} & D_{14} & D_{15} & D_{16} \\ & & & & & & & D_{22} & D_{23} & D_{24} & D_{25} & D_{26} \\ & & s & y & m. & & & & D_{33} & D_{34} & D_{35} & D_{36} \\ & & & & & & & & & D_{44} & D_{45} & D_{46} \\ & & & & & & & & & & D_{55} & D_{56} \\ & & & & & & & & & & & D_{66} \end{bmatrix} \begin{Bmatrix} \varepsilon_x \\ \varepsilon_y \\ \varepsilon_z \\ \gamma_{xz} \\ \gamma_{yz} \\ \gamma_{xy} \\ \kappa_x \\ \kappa_y \\ \kappa_z \\ \kappa_{xz} \\ \kappa_{yz} \\ \kappa_{xy} \end{Bmatrix}, \tag{2.1}$$

which equates a forces/moments vector to a strain/curvature vector via a stiffness matrix. However, for thin laminates, through thickness (z-direction) stresses are

assumed to be negligible and ignored. This means all z-direction terms are removed to simplify the expression to

$$\begin{bmatrix} N_x \\ N_y \\ N_{xy} \\ M_x \\ M_y \\ M_{xy} \end{bmatrix} = \begin{bmatrix} A_{11} & A_{12} & A_{16} & B_{11} & B_{12} & B_{16} \\ & A_{22} & A_{26} & B_{12} & B_{22} & B_{26} \\ & & A_{66} & B_{16} & B_{26} & B_{66} \\ & & & D_{11} & D_{12} & D_{16} \\ & sym. & & & D_{22} & D_{26} \\ & & & & & D_{66} \end{bmatrix} \begin{Bmatrix} \varepsilon_x \\ \varepsilon_y \\ \gamma_{xy} \\ \kappa_x \\ \kappa_y \\ \kappa_{xy} \end{Bmatrix} . \tag{2.2}$$

The stiffness matrix in Eq. (2.2) is commonly referred to as the ABD matrix and also describes the elastic coupling behaviour of a laminate. For example, the A_{16} and A_{26} terms describe the extension-shear coupling since they link loads N_x and N_y to shear strain γ_{xy}, and shear load N_{xy} to strains ε_x and ε_y. A full list of coupling terms is summarised in Table 2.1. If these coupling terms are zero, it indicates that a laminate will not exhibit the corresponding coupling behaviour.

Term(s)	**Elastic Coupling**
A_{16}, A_{26}	Extension-shear
B_{11}, B_{12}, B_{22}	Extension-bending
B_{16}, B_{26}	Extension-twist and shear-bending
B_{66}	Shear-twist
D_{16}, D_{26}	Bend-twist

Table 2.1 Elastic coupling terms.

Calculation of the ABD matrix for a laminate is performed by combining the contribution of each ply. The stiffness matrix describing the response of a ply to in-plane loading is given by

$$\boldsymbol{Q} = \begin{bmatrix} Q_{11} & Q_{12} & 0 \\ Q_{12} & Q_{22} & 0 \\ 0 & 0 & Q_{66} \end{bmatrix} , \tag{2.3}$$

where

$$\begin{aligned} Q_{11} &= \frac{{E_{11}}^2}{E_{11} - {v_{12}}^2 E_{22}} , & Q_{12} &= \frac{v_{12} E_{11} E_{22}}{E_{11} - {v_{12}}^2 E_{22}} , \\ Q_{22} &= \frac{E_{11} E_{22}}{E_{11} - {v_{12}}^2 E_{22}} , & Q_{66} &= G_{12} , \end{aligned} \tag{2.4}$$

E_{11} is the in-plane ply modulus in the fibre direction, E_{22} is the in-plane ply modulus transverse to the fibre direction, v_{12} is the in-plane Poisson's Ratio and G_{12} is the in-plane shear modulus. $\boldsymbol{Q}$ is in the local ply co-ordinates. Before summing the contribution of a ply to the laminate stiffness matrix, this must be converted into the

global laminate co-ordinate system using a transformation matrix. The transformation matrix is given by

$$\boldsymbol{T} = \begin{bmatrix} \cos^2\phi & \sin^2\phi & \sin\phi\cos\phi \\ \sin^2\phi & \cos^2\phi & -\sin\phi\cos\phi \\ -2\sin\phi\cos\phi & 2\sin\phi\cos\phi & \cos^2\phi - \sin^2\phi \end{bmatrix} \quad , \tag{2.5}$$

where ϕ is the angle between the fibre direction within the ply and the laminate reference axis. The stiffness matrix of a ply in the global laminate co-ordinate system is then given by

$$\overline{\boldsymbol{Q}} = \boldsymbol{T}^T \boldsymbol{Q} \boldsymbol{T} \quad . \tag{2.6}$$

The ABD matrix can then be computed by summing for all layers

$$\boldsymbol{A} = \sum_{k=1}^{N} \overline{\boldsymbol{Q}}_k (\ z_k - z_{k-1}\ ) \tag{2.7a}$$

$$\boldsymbol{B} = \frac{1}{2} \sum_{k=1}^{N} \overline{\boldsymbol{Q}}_k (\ {z_k}^2 - {z_{k-1}}^2) \tag{2.7b}$$

$$\boldsymbol{D} = \frac{1}{3} \sum_{k=1}^{N} \overline{\boldsymbol{Q}}_k (\ {z_k}^3 - {z_{k-1}}^3) \quad , \tag{2.7c}$$

where N is the total number of plies in the laminate, z_k is the distance from laminate mid-plane to the top of ply k and z_{k-1} is the distance from laminate mid-plane to the top of ply $k-1$ (see Fig. 2.1).

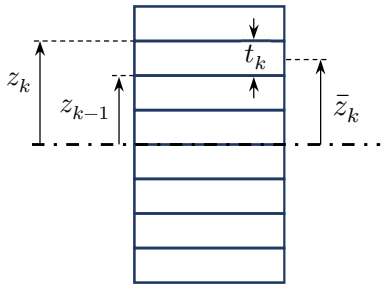

Figure 2.1 Cross-section of 8 ply laminate, indicating ply thickness and lever arm terms about mid-plane.

There is also another way to express Eq. (2.7) using the ply thickness, t_k, and mean ply lever arm, $\bar{z}_k$, (see Fig. 2.1) where

$$\begin{aligned} t_k &= z_k - z_{k-1} \\ \bar{z}_k &= \frac{z_k + z_{k-1}}{2} \quad . \end{aligned} \tag{2.8}$$

Consider the following term from Eq. (2.7b), which can be reformulated as

$$\frac{1}{2}\Big({z_k}^2 - {z_{k-1}}^2 \Big)$$

$$= \Big(z_k - z_{k-1} \Big) \Big(\frac{z_k + z_{k-1}}{2} \Big) \tag{2.9}$$

$$= \Big(t_k \Big) \Big(\bar{z}_k \Big) \quad .$$

Now consider the following term from Eq. (2.7c), which can also be reformulated as

$$\frac{1}{3}\Big({z_k}^3 - {z_{k-1}}^3 \Big) = \frac{1}{12}\Big(4{z_k}^3 - 4{z_{k-1}}^3 \Big)$$

$$= \Big(z_k - z_{k-1} \Big) \Big(\frac{z_k + z_{k-1}}{2} \Big)^2 + \frac{1}{12}\Big(z_k - z_{k-1} \Big)^3 \tag{2.10}$$

$$= t_k \ {\bar{z}_k}^2 + \frac{{t_k}^3}{12} \quad .$$

A complete list of calculation steps for Eq. (2.10) is shown in Appendix A. This means Eq. (2.7) can be expressed as

$$\boldsymbol{A} = \sum_{k=1}^{N} \overline{\boldsymbol{Q}}_k \, t_k \tag{2.11a}$$

$$\boldsymbol{B} = \sum_{k=1}^{N} \overline{\boldsymbol{Q}}_k \, t_k \, \bar{z}_k \tag{2.11b}$$

$$\boldsymbol{D} = \sum_{k=1}^{N} \overline{\boldsymbol{Q}}_k \left(t_k \, {\bar{z}_k}^2 + \frac{{t_k}^3}{12} \right) \quad . \tag{2.11c}$$

2.1.2 Uncoupled Stacking Sequences

Bartholomew [5] investigated the origins of elastic coupling and how it is dependent on the particular stacking sequence of a laminate. Mathematical proofs for the existence (or otherwise) of particular forms of elastic coupling in different categories of laminates are developed. The equations used in [5] are in the form of Eq. (2.7). Laminates with even and odd numbers of plies are examined, up to a total of 21 layers for symmetric laminates and 16 layers for anti-symmetric laminates. The research lists fully uncoupled solutions and searches for patterns within them. For example, the anti-symmetric laminate $[+/-/-/+/-/+/+/-]$ is fully uncoupled, as is a laminate consisting of two such laminates put together, $[+/-/-/+/-/+/+/-]_2$. Mathematical proofs for these patterns are not covered.

York [6,7] presents symmetric and anti-symmetric laminates that are fully uncoupled or exhibit particular forms of elastic coupling. Non-symmetric stacking sequences are investigated as well as symmetric and anti-symmetric, up to 21 plies thick. Feasible domains of lamination parameters are presented for each coupling response and a list of stacking sequence solutions is compiled. Vannucci and Verchery [8] present a method for designing fully isotropic laminates (FILs). They indicate parameters which must be set in order to achieve isotropy and consider layer orientations other than the standard 0°, 90° and ±45°. FILs are a special case of uncoupled laminate because two or more FILs can be stacked together, with any angle between them, and remain isotropic. However, stipulating that a laminate be isotropic is more limiting than being fully uncoupled.

The majority of the literature, such as [5-8], use the equations for finding the ABD matrix in the form of Eq. (2.7). Using the equations in the form of Eq. (2.11) leads to different insights into elastic coupling and are investigated as part of this research.

Symmetric and Anti-symmetric Stacking Sequences

The stiffness matrix of cross- and angle-plies in the global laminate co-ordinate system can be summarised as

$$\overline{\boldsymbol{Q}}_{0,90} = \begin{bmatrix} + & + & 0 \\ + & + & 0 \\ 0 & 0 & + \end{bmatrix} \quad \overline{\boldsymbol{Q}}_{+\phi} = \begin{bmatrix} + & + & + \\ + & + & + \\ + & + & + \end{bmatrix} \quad \overline{\boldsymbol{Q}}_{-\phi} = \begin{bmatrix} + & + & - \\ + & + & - \\ - & - & + \end{bmatrix} \quad , \tag{2.12}$$

where + indicates some positive value and − a negative value. Equation (2.7) can be formulates as

$$[\boldsymbol{A}, \boldsymbol{B}, \boldsymbol{D}] = \int \overline{\boldsymbol{Q}} \{1, z, z^2\} \, dz \quad , \tag{2.13}$$

indicating that the **A** matrix is independent of the position of plies within a stack, **B** depends on the first lever arm and **D** on the second lever arm. From Eq. (2.12) all $\square_{16}$ and $\square_{26}$ coupling terms are dependent only on angle-plies. From (2.13), there must be an equal number of $+\phi^\circ$ and $-\phi^\circ$ plies for $A_{16} = A_{26} = 0$, in which case a laminate is said to be balanced. This is the case by definition for an anti-symmetric laminate since every $+\phi^\circ$ angle ply with lever arm $+\bar{z}_k$ is mirrored by a $-\phi^\circ$ angle ply with lever arm $-\bar{z}_k$. Both symmetric and anti-symmetric laminates result in symmetry of cross-plies, such that these will not contribute to any **B** coupling terms. Since $\overline{Q}_{11}$,

$\overline{Q}_{12}$, $\overline{Q}_{22}$ and $\overline{Q}_{66}$ for a $+\phi^\circ$ angle ply are the same as for a $-\phi^\circ$ angle ply, these will also cancel in Eq. (2.13) for **B**, whether a laminate is symmetric or anti-symmetric.

Removal of the remaining **B** coupling terms (B_{16}, B_{26}) requires that

$$\sum_{k=1}^{N} \left(\bar{z}_k \right)_{+\phi} = \sum_{k=1}^{N} \left(\bar{z}_k \right)_{-\phi} = 0 \quad , \tag{2.14}$$

which is the case by definition for symmetric laminates, since every $\pm\phi$ ply with lever arm $+\bar{z}_k$ is mirrored by the same with lever arm $-\bar{z}_k$. In anti-symmetric laminates, the position of the $+\phi^\circ$ angle plies below the mid-plane is dictated by the $-\phi^\circ$ angle plies above the mid-plane. This leads to the condition

$$\sum_{k=1}^{N} \left(\bar{z}_k \right)_{+\phi} = \sum_{k=1}^{N} \left(\bar{z}_k \right)_{-\phi} \quad , \tag{2.15}$$

which if satisfied for the half-laminate (i.e. above the mid-plane), indicates an anti-symmetric laminate is fully uncoupled.

Removal of the **D** coupling terms requires that

$$\sum_{k=1}^{N} \left(\bar{z}_k{}^2 \right)_{+\phi} = \sum_{k=1}^{N} \left(\bar{z}_k{}^2 \right)_{-\phi} \quad , \tag{2.16}$$

since $\overline{\boldsymbol{Q}}_{16}$ and $\overline{\boldsymbol{Q}}_{26}$ are equal and opposite for $+\phi^\circ$ and $-\phi^\circ$ plies and will cancel. Equation (2.16) is always satisfied for an anti-symmetric laminate but not necessarily for symmetric.

Coupling Terms	**Symmetric**	**Anti-symmetric**
A_{16}, A_{26}	Balanced	By definition
B_{11}, B_{12}, B_{22}, B_{66}	By definition	By definition
B_{16}, B_{26}	By definition	$\sum_{k=1}^{N} \left(\bar{z}_k \right)_{+} = \sum_{k=1}^{N} \left(\bar{z}_k \right)_{-}$
D_{16}, D_{26}	$\sum_{k=1}^{N} \left(\bar{z}_k{}^2 \right)_{+} = \sum_{k=1}^{N} \left(\bar{z}_k{}^2 \right)_{-}$	By definition

Table 2.2 Coupling terms that are zero (by definition) for symmetric and anti-symmetric stacking sequences, and the conditions required to remove those that are not necessarily zero.

A summary of the coupling terms that are zero (by definition) for symmetric and anti-symmetric stacking sequences is shown in Table 2.2. For coupling terms that are not necessarily zero, the condition required to remove them is listed.

Results using MATLAB Code

Use of a computer to search for fully uncoupled stacking sequences is required for large laminates as the number of possible stacking sequences grows exponentially. A MATLAB script has been written to find fully uncoupled laminates that fit certain conditions, such as being symmetric or anti-symmetric and with a given number of plies. For the particular cases of symmetric and anti-symmetric laminates, it is possible to significantly reduce the computational work required, since only half the stack need be considered, with the other half implied by symmetry or anti-symmetry. Since cross plies do not contribute to any coupling of symmetric or anti-symmetric laminates, these can effectively be ignored. Laminates consisting of cross plies and one angle of angle plies ($\pm\phi^\circ$) are considered when searching for fully uncoupled stacking sequences. $+\phi^\circ$ angle plies are represented by $+1$, $-\phi^\circ$ angle plies as -1 and both 0° and 90° are represented by 0 in the MATLAB script. Some example stacking sequences and how they would be represented in the script are shown in Table 2.3.

Example #	Stacking sequence	Sequence vector
1	$[+32/\text{-}32/\text{-}32/+32]_{\text{A}}$	[+1; -1; -1; +1]
2	$[+45/90/0/\text{-}45/0/90]_{\text{S}}$	[+1; 0; 0; -1; 0; 0]
3	$[+45/0/90/\text{-}45/90/0]_{\text{S}}$	[+1; 0; 0; -1; 0; 0]

Table 2.3 Example stacking sequences, showing how they would be stored in the code when searching for fully uncoupled laminates.

Notice that examples 2 and 3 in Table 2.3 are represented by the same sequence vector in the MATLAB script. This is because only 0° and 90° plies have been switched and are both represented by 0. The size of the sequence vector is half the number of layers in the laminate. The script performs an exhaustive search of possible stacking sequences by first setting all sequence vector entries to -1 and then incrementing the entries through 0 and 1, one at a time. An example regime is shown in Table 2.4.

Iteration	Sequence vector
1	[-1; -1; -1; -1]
2	[-1; -1; -1; 0]
3	[-1; -1; -1; +1]
4	[-1; -1; 0; -1]
5	[-1; -1; 0; 0]
6	[-1; -1; 0; +1]
7	[-1; -1; +1; -1]

Table 2.4 First 7 iterations of sequence vector for example 8 layer laminate.

For each iteration, the sequence vector is checked against the relevant condition for a fully uncoupled laminate – Eq. (2.16) for symmetric laminates and Eq. (2.15) for anti-symmetric laminates. The number of iterations that the script must cycle through is given by

$$Iterations = \varphi^{\beta} \quad , \tag{2.17}$$

where β is the size of the sequence vector and φ is the number of different entries each row can be assigned. There are 3 possible entries in Table 2.4: -1, 0 or +1. It is highly beneficial to represent both 0° and 90° plies as 0 in the sequence vector, thereby meaning $\varphi = 3$, rather than 4. It also vastly reduces computational effort by considering only half the laminate, meaning $\beta = N/2$, rather than N, where N is the number of plies in the laminate. For a 20 ply laminate, for example, these savings reduce the number of iterations from $\sim 10^{12}$ to $\sim 10^{5}$.

The script is used to find the number of fully uncoupled sequence vectors for symmetric and anti-symmetric laminates with an increasing even number of plies, summarised in Table 2.5. The zero sequence vector (i.e. representing a laminate consisting of only 0° and 90° plies) is a fully uncoupled solution for all laminate sizes but since this result is not interesting it is omitted from Table 2.5. Note that there is always an even number of solutions since for any given fully uncoupled sequence vector, reversing the $+\phi^{\circ}$ and $-\phi^{\circ}$ plies will also result in a fully uncoupled laminate. Moreover, setting the first row in the sequence vector (representing the outer most ply) to 0 is in effect the same as reducing the number of plies by 2, by limiting the design space. This means a further 3-fold saving in computational effort is possible since it is not necessary to iterate the first row of the sequence vector through 0 and +1. It is only necessary to consider -1, doubling the number of solutions and then adding the result from the previous number of plies.

It can be seen from Table 2.5 that there are significantly more fully uncoupled solutions for anti-symmetric laminates than there are for symmetric laminates with the same number of layers. The difference between them as a factor is also indicated. The reason there are many more anti-symmetric solutions becomes clear when considering the previously derived conditions that the stacking sequences must satisfy in order to be fully uncoupled. An anti-symmetric laminate is balanced by definition and must only satisfy Eq. (2.15) to be fully uncoupled, while a symmetric laminate is not necessarily balanced and must also satisfy Eq. (2.16) to be fully uncoupled. Mathematically, Eq. (2.15) is much more readily satisfied, such that the sum of the lever arm terms is equal, than Eq. (2.16), which requires the sum of the lever arm terms squared is equal. There are therefore many more sequences that satisfy the condition for a fully uncoupled anti-symmetric laminate than that of a symmetric laminate.

The script is then used to find the number of fully uncoupled sequences for laminates with an odd number of plies. The results are shown in Table 2.6. The central ply (on the mid-plane) must be a 0° or 90° ply in order for a symmetric or anti-symmetric laminate with an odd number of plies to be fully uncoupled. The difference between the number of fully uncoupled sequences for symmetric and anti-symmetric laminates of the same size is significantly greater for an odd number of plies than an even number. However, the difference factor initially reduces with increasing laminate size and then steadily increases for both even and odd ply numbers.

No. Plies	Uncoupled sequences		$\frac{U_A}{U_S}$
	U_S	U_A	
2	0	0	-
4	0	0	-
6	0	0	-
8	0	2	∞
10	0	8	∞
12	2	20	10.0
14	8	48	6.0
16	20	116	5.8
18	46	294	6.4
20	96	760	7.9
22	212	1 992	9.4
24	474	5 260	11.1
26	1 070	14 024	13.1
28	2 576	37 698	14.6
30	6 316	102 150	16.2
32	15 744	278 586	17.7
34	39 522	764 144	19.3

Table 2.5 Number of fully uncoupled sequence vectors for symmetric (U_S) and anti-symmetric (U_A) laminates of increasing size (even number of plies only), omitting the zero sequence vector solution.

No. Plies	Uncoupled sequences		$\frac{U_A}{U_S}$
	U_S	U_A	
3	0	0	-
5	0	0	-
7	0	2	∞
9	0	6	∞
11	0	14	∞
13	0	34	∞
15	2	86	43.0
17	10	216	21.6
19	22	546	24.8
21	54	1 416	26.2
23	112	3 734	33.3
25	242	9 910	41.0
27	556	26 512	47.7
29	1 334	71 580	53.7
31	3 118	194 680	62.4
33	7 866	532 480	67.7
35	19 602	1 464 028	74.7

Table 2.6 Number of fully uncoupled sequence vectors for symmetric (U_S) and anti-symmetric (U_A) laminates of increasing size (odd number of plies only), omitting the zero sequence vector solution.

Whether a laminate has an even or an odd number of plies is important because it determines what pattern the lever arm terms, $\bar{z}_k$, follow. Moving away from the mid-plane, even laminates follow the pattern 0.5, 1.5, 2.5 etc., while odd laminates proceed as 1, 2, 3 etc. This in turn has significant consequences when satisfying Eq. (2.16) or Eq. (2.15). The result is visible in Figure 2.2. The difference between even and odd laminates is most significant for symmetric laminates, where it appears an even number of plies is beneficial for yielding fully uncoupled sequences, relative to the size of the laminate. For anti-symmetric laminates it appears an odd number of plies is marginally beneficial.

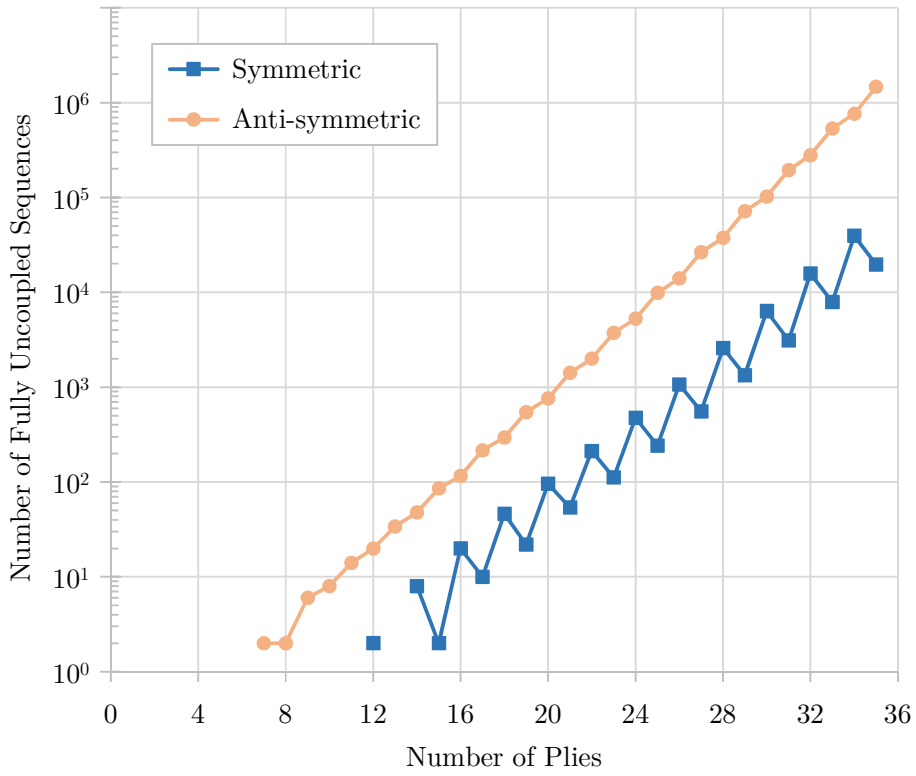

Figure 2.2 Number of fully uncoupled sequences, plotted on a logarithmic scale, against number of plies for symmetric and anti-symmetric laminates.

2.1.3 Implications of Industrial Applications

Joining Laminates

Industrial products typically consist of multiple laminates, which are joined together, either by adhesion or mechanical fastening, such as skin and stiffener laminates in an aircraft wing. When two laminates are stacked they effectively form one larger laminate, which can exhibit significantly different coupling behaviour from the two constituent laminates. This is driven by a shift in the laminate reference plane, away from the mid-plane of the two constituent laminates, to the mid-plane of the combined laminate. This changes the lever arm ($\bar{z}$) terms for each ply. The implications of shifting the reference plane are explored to determine the change in coupling behaviour that laminates may exhibit when joined.

The in-plane stiffness matrix is unaffected by a shift in the reference plane, since Eq. (2.11a) does not depend on $\bar{z}$. Therefore the combined laminate will not exhibit extension-shear coupling provided the constituent laminates do not exhibit it. The

coupling stiffness matrix does depend on $\bar{z}$. Assuming the reference plane is shifted by a distance $\Delta\bar{z}$ through thickness, Eq. (2.11b) can be reformulated to

$$\boldsymbol{B} = \sum_{k=1}^{N} \overline{\boldsymbol{Q}}_k \, t_k \left(\bar{z}_k + \Delta\bar{z} \right) \quad . \tag{2.18}$$

Considering the contribution from the shift in the reference plane only, and assuming equal thickness for every ply,

$$\Delta\boldsymbol{B} = t \; \Delta\bar{z} \sum_{k=1}^{N} \overline{\boldsymbol{Q}}_k \quad . \tag{2.19}$$

Since $\overline{Q}_{11}$, $\overline{Q}_{12}$, $\overline{Q}_{22}$ and $\overline{Q}_{66}$ are positive and finite regardless of fibre orientation, the corresponding extension-bending and shear-twist couplings always change with a shift in the reference plane. This change must be equal and opposite for two constituent laminates, in order for the combined laminate to not exhibit these couplings, assuming the constituent laminates do not exhibit them. However, $\overline{Q}_{16}$ and $\overline{Q}_{26}$ are zero for cross-plies and equal and opposite for positive and negative angle-plies. Therefore, for a balanced laminate (with an equal number of positive and negative angle-plies), a shift in the reference plane does not affect the extension-twisting / shear-bending coupling; a combined laminate inherits the sum of these couplings from the constituent laminates. If this is zero for the constituent laminates, the combined laminate in uncoupled in this sense.

Similarly, Eq. (2.11c) can be reformulated to

$$\boldsymbol{D} = \sum_{k=1}^{N} \overline{\boldsymbol{Q}}_k \left(t_k \; \left(\bar{z}_k + \Delta\bar{z} \right)^2 + \; \frac{{t_k}^3}{12} \right) \tag{2.20}$$

and considering the contribution from the shift in the reference plane,

$$\Delta\boldsymbol{D} = t \; \Delta\bar{z}^{\,2} \sum_{k=1}^{N} \overline{\boldsymbol{Q}}_k \; + \; 2t \; \Delta\bar{z} \sum_{k=1}^{N} \bar{z}_k \; \overline{\boldsymbol{Q}}_k \quad . \tag{2.21}$$

Only angle-plies contribute to bend-twist coupling (D_{16} and D_{26}) since $\overline{Q}_{16}$ and $\overline{Q}_{26}$ are zero for cross-plies and equal and opposite for positive and negative angle-plies as previously stated. This implies $\sum \overline{Q}_{16,k} = \sum \overline{Q}_{26,k} = 0$ for balanced laminates and Eq. (2.21) becomes

$$\begin{aligned} \Delta D_{16} &= 2t \; \Delta\bar{z} \sum_{k=1}^{N} \bar{z}_k \; \overline{Q}_{16,k} \\ \Delta D_{26} &= 2t \; \Delta\bar{z} \sum_{k=1}^{N} \bar{z}_k \; \overline{Q}_{26,k} \end{aligned} \tag{2.22}$$

for the bend-twist coupling terms. These coupling terms are therefore zero if $\sum \bar{z}_k = 0$ for both positive and negative angle-plies. As discussed in Section 2.1.2, this is the case by definition for symmetric laminates. This is also the only condition that must be satisfied to produce a fully uncoupled anti-symmetric laminate.

The result is that joining two fully uncoupled symmetric or anti-symmetric laminates, has only the potential to produce extension-bending and shear-twist coupling. If the constituent laminates are not fully uncoupled and $\sum \bar{z}_k \neq 0$ for any orientation of angle-ply, then bend-twist coupling can also arise, whether or not it is present in the constituent laminates. An assumption made throughout these calculations is that the constituent laminates are joined in a way that does not allow slip. In many industrial applications, laminates are joined with mechanical fasteners rather than adhesion and so this assumption may not be entirely valid in those cases.

Stiffener Blade

Stiffeners are attached to thin components to increase the second moment of area out-of-plane. This increases the capacity of the component to carry bending loads and resist buckling under axial compression. T-shaped stiffener blades are commonly employed in airframe structures, for example stringers that are used to stiffen skin panels and run along the span of the wing. The exposed free edge of the blade tip illustrated in Fig. 2.3a is susceptible to damage and initiating delamination of the laminate. Therefore, the blade tip is typically protected by folding the laminate over as illustrated in Fig. 2.3b. This has an interesting consequence in that the stiffener blade has an anti-symmetric stacking sequence since angle-plies are reversed (positive becoming negative and vice versa) by the action of folding the laminate. The fold does not affect cross-plies, which remain in the same orientation either side of the blade laminate.

It is shown in section 2.1.2 that, by default, anti-symmetric laminates eliminate all coupling terms except extension-twist/shear-bending (B_{16} and B_{26}). In the case of Fig. 2.3b, the blade laminate can be considered as two laminates joined together: the base laminate and an anti-symmetric version of the base laminate. As discussed previously, B_{16} and B_{26} are unaffected by a shift in the reference plane provided there is an equal number of positive and negative angle-plies. Therefore, the blade laminate inherits these coupling terms directly from the base laminate and if they are zero in the base laminate, the blade laminate is fully uncoupled. In section 2.1.2 it is shown that

symmetric laminates do not exhibit B_{16} and B_{26} by default. Therefore if the base laminate of a folded T-shaped stiffener is symmetric, the blade will be fully uncoupled, i.e. $[[...]_S]_A$ is fully uncoupled, where '...' represents any stacking sequence.

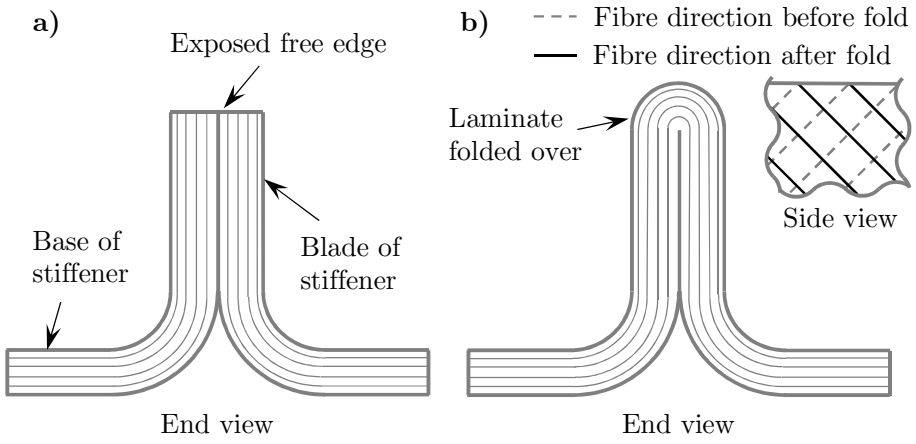

Figure 2.3 T-shaped stiffener. **a)** With exposed blade tip. **b)** With folded blade tip, showing effect on fibre angle of angle-plies.

Curved Laminates

Curved laminates are another common feature required in industrial applications. Curvature generally shifts the neutral plane away from the mid-thickness of a laminate, towards the inner radius of the curve. This is apparent from corner unfolding analysis, discussed later in Chapter 3 and Chapter 4. As discussed previously in this section for the joining of laminates, the potential for a shift in neutral plane to cause a change in coupling terms can be limited to extension-bending and shear-twist for fully uncoupled stacking sequences. Industrial components often have flat sections and curved sections, with a common laminate running through both. A laminate that remains uncoupled with a shift in reference plane is therefore useful for these applications.

2.2 Tapered Laminates

Industrial structures frequently include components with changes in thickness along their length. This accounts for the variation in load, such as that caused by attachment points for other components, whilst reducing weight where possible. High stress concentrations associated with step changes in thickness are avoided by introducing tapered regions to smoothly transition between thin and thick sections. This is

relatively straightforward for isotropic materials, such as metal, however tapering composite laminates requires the addition or removal of discrete plies along their length. In order to make the tapered region as smooth as possible, plies can be added or removed one or two at a time, however even in this case there are small step changes in the laminate stacking sequence. Since individual plies are highly anisotropic, the addition of a single ply to a laminate is likely to change the balance of a laminate, affecting the level of elastic coupling, according to Eq. (2.11) as discussed previously. The design of tapered regions is therefore important to the performance of a laminate once cured, but it also has an influence over the consolidation behaviour during manufacture.

2.2.1 Consolidation of Prepreg in Tapered Laminates

Composite laminate material is used in different forms during manufacture. One form commonly used within industry is that of prepreg material. Long, narrow strips or "tows" of fibrous material that have been pre-impregnated with resin material are laid down onto the laminate before being de-bulked and cured to produce the finished article. During the de-bulking process, trapped air is removed from the laminate and the resin is re-distributed more evenly throughout the laminate. As this occurs the laminate is said to consolidate, with a reduction in thickness of typically 10-15%. Through-thickness movement as a result of consolidation is towards the tool surface, which is fixed. The effect of consolidation within a tapered laminate is illustrated in Fig. 2.4.

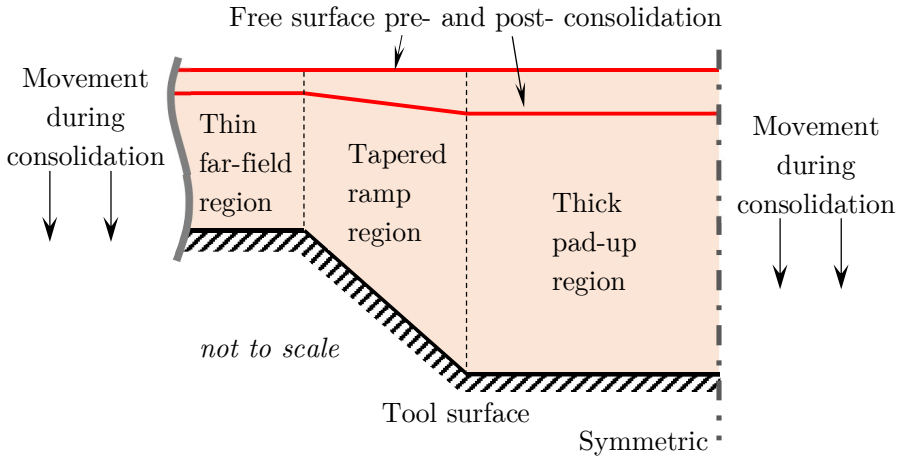

Figure 2.4 Tapered laminate showing the effect of consolidation, which is proportional to thickness, resulting in greater movement in the thick region.

Since consolidation is generally proportional to laminate thickness, the thicker the laminate, the greater the absolute movement. In tapered laminates this creates a mismatch between the thin and thick regions, most evident at the free surface (farthest away from the tool), where movement is greatest. Consider the free surface in Fig. 2.4. This spans a greater distance from left to right post-consolidation than it does pre-consolidation, as a result of the angle change in the tapered ramp region. This implies that during consolidation the surface ply must either stretch or draw in length from the far-field.

The significance of this apparent length change can be assessed by assuming the tapered ramp region stretches and analysing the resulting level of strain. Consider the position of a single ply running through the tapered region, highlighted in Fig. 2.5. Assuming the ply-drops in the tapered region are evenly distributed throughout the thickness, it can be expected that the ply will be in the same position relative to total laminate thickness in both thin and thick laminates. The distance between a single ply and the tool surface as a proportion of laminate thickness is given by ρ. The absolute distance is therefore given by ρt_f and ρt_p for thin and thick laminates respectively, where t_f and t_p are the total thickness of the (thin) far-field and (thick) pad-up laminates respectively. The change in laminate thickness is Δt and occurs over a longitudinal distance, l_r, in the tapered region. Initially it is assumed that the laminate is laid up such that the free surface is flat pre-cure, as illustrated in Fig. 2.4 and Fig. 2.5.

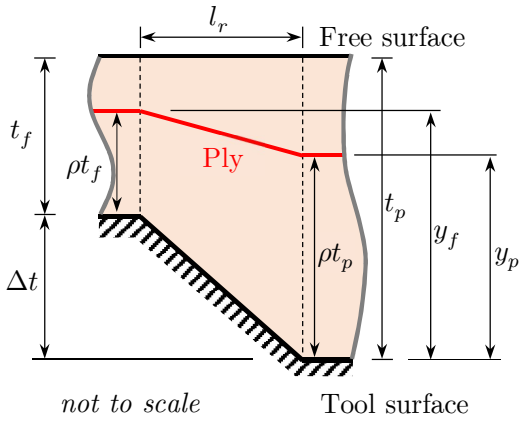

Figure 2.5 Tapered region pre-consolidation, highlighting the position of a single ply (in red) within the stack. Key dimensions are labelled.

The tool surface of the thick laminate (RHS Fig. 2.5) is taken as the vertical datum. The vertical position of the ply in the thin laminate is therefore given by

$$y_f = \Delta t + \rho t_f \tag{2.23}$$

and its vertical position in the thick laminate is

$$y_p = \rho t_p \quad . \tag{2.24}$$

The pre-consolidation length of the ply in the tapered region is then

$$l_{pre} = \sqrt{{l_r}^2 + (y_f - y_p)^2} \quad . \tag{2.25}$$

If c is the consolidation as a proportion of laminate thickness, the post-consolidation thickness of the thin laminate is given by

$$t'_f = t_f(1-c) \tag{2.26}$$

and that of the thick laminate by

$$t'_p = t_p(1-c) \quad . \tag{2.27}$$

The post-consolidation length of the ply is given by

$$l_{post} = \sqrt{{l_r}^2 + \left(y'_f - y'_p\right)^2} \quad . \tag{2.28}$$

The engineers' strain associated with the change in length of the ply during consolidation is therefore, with a full list of calculation steps given in Appendix A,

$$\begin{aligned} \varepsilon &= \frac{l_{post}}{l_{pre}} - 1 \\ &= \frac{\sqrt{{l_r}^2 + \left(y'_f - y'_p\right)^2}}{\sqrt{{l_r}^2 + (y_f - y_p)^2}} - 1 \\ &= \frac{\sqrt{{l_r}^2 + \left(\Delta t(1-\rho+\rho c)\right)^2}}{\sqrt{{l_r}^2 + \left(\Delta t(1-\rho)\right)^2}} - 1 \end{aligned} \quad . \tag{2.29}$$

If the gradient of the tapered region (or ramp rate) is defined as

$$R = \frac{l_r}{\Delta t} \quad , \tag{2.30}$$

Eq. (2.29) can be rewritten as, with a full list of calculation steps given in Appendix A,

$$\varepsilon = \frac{\sqrt{(R\Delta t)^2 + \left(\Delta t(1-\rho+\rho c)\right)^2}}{\sqrt{(R\Delta t)^2 + \left(\Delta t(1-\rho)\right)^2}} - 1$$
$$= \frac{\sqrt{R^2 + (\ 1-\rho+\rho c\ )^2}}{\sqrt{R^2 + (\ 1-\rho\ )^2}} - 1 \quad . \tag{2.31}$$

From Eq. (2.31), the two key parameters that affect the amount a ply has to change length are the ramp rate, R, and level of consolidation, c. If these are known, it is possible to plot the consolidation induced strain through the entire thickness of a tapered laminate ($\rho = 0 \rightarrow 1$). The level of strain is shown in Fig. 2.6 for 3 different ramp rates, assuming 12% consolidation. These are representative of tapered regions commonly employed within industry. As shown, the level of strain increases exponentially as the ramp becomes steeper ($R \rightarrow 0$).

It is common practice to lay-up a laminate pre-consolidation with a small bulge in the free surface, such that is becomes flat post-consolidation, accounting for the movement illustrated in Fig. 2.4. The effect this has on the induced strains is shown in Fig. 2.7, where a laminate that has a free surface that is flat post-consolidation is compared with one where the free surface is flat pre-consolidation. This reverses the sign of the strain at the free surface, from +72 μstrain to -72 μstrain and reduces the peak level of strain near the mid-thickness.

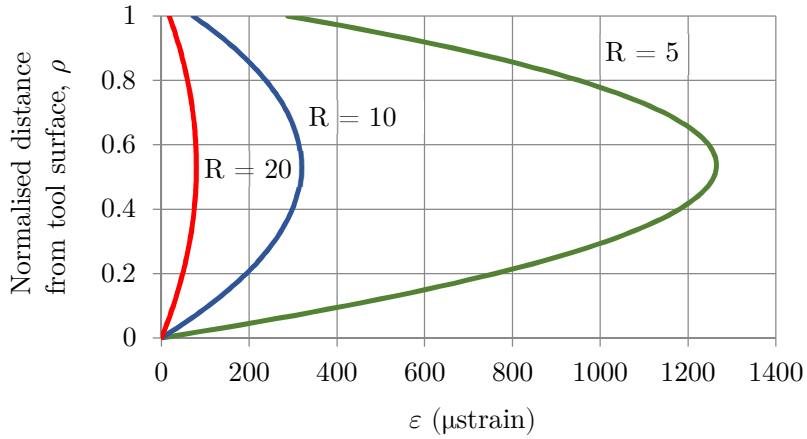

Figure 2.6 Consolidation induced strain for 3 different ramp rates. This assumes 12% consolidation and that length change is accommodated by plies stretching in the tapered region.

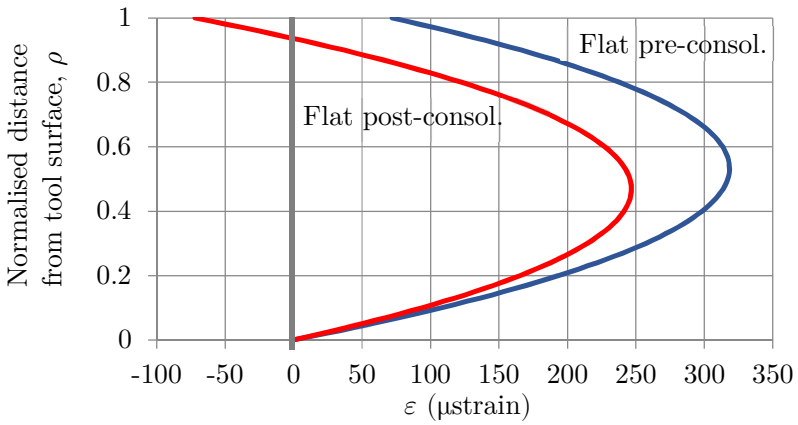

Figure 2.7 Comparison of consolidation induced strain for a laminate free surface that is flat post-consolidation with one that is flat pre-consolidation. A ramp rate of 10 and consolidation of 12% is assumed in both cases.

2.2.2 Protected Zone in Tapered Laminates

From Fig. 2.6 and Fig. 2.7 the potential level of strain induced by consolidation of tapered laminates can be significant. In practice there is likely to be some level of 'slip', whereby plies slide over each other, dragging in length from the far-field and reducing the level of induced strain. The movement between plies of uncured prepreg material has been investigated by Erland et al. [9] and Larberg and Åkermo [10]. If the induced length change is accommodated neither by strain nor slip of the ply, the result is reduced consolidation. Slip can be significantly impeded by high inter-laminar traction and large consolidation pressures, effectively clamping plies together [9]. This is particularly significant for plies with fibres that travel a long distance into the far-field, up to several metres for large components. These plies are defined as 0° plies, i.e. with fibres running left to right in Fig. 2.4. 0° plies are also stiff in the direction of induced length change due to consolidation, discussed in 2.2.1. Therefore, continuous 0° plies offer the most resistance and can lead to poor consolidation during manufacture.

This effect can be mitigated by designing the tapered laminate in such a way that the continuous 0° plies are not required to change length during consolidation. This is achieved by ensuring such plies remain equidistant from the tool surface throughout the tapered region, which implies no discontinuous plies are added or removed between the continuous 0° plies and the tool surface. The result is a 'protected zone' of continuous plies adjacent to the tool surface, illustrated in Fig. 2.8.

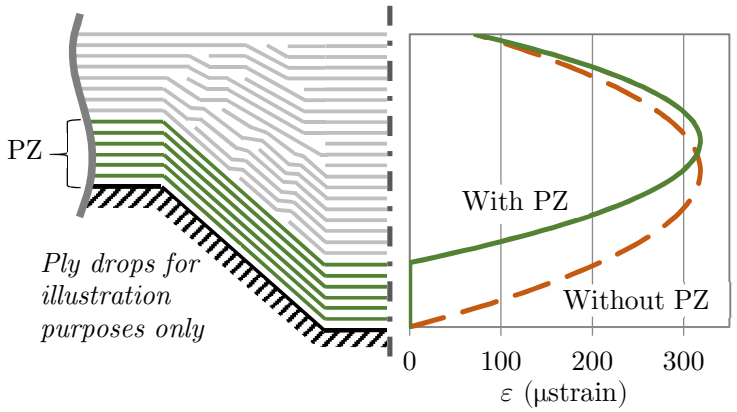

Figure 2.8 Protected zone (PZ) of continuous plies that remain equidistant from tool surface throughout tapered region, left. Effect of PZ on consolidation induced strain through thickness, compared with a laminate without a PZ, right.

The graph in Fig. 2.8 shows that there is no consolidation induced strain in the protected zone. Above this the maximum strain is the same as within a laminate without a protected zone, showing there is no significant penalty elsewhere in the laminate. This assumes the continuous plies outside the protected zone spread out evenly into the thicker laminate, i.e. a ply mid-thickness of the unprotected zone in the thin laminate transitions through the tapered region into the mid-thickness of the unprotected zone in the thick laminate. It is therefore believed that in large laminates with long 0° plies running through tapered regions, designing the laminate with a protected zone will help improve consolidation.

2.3 Demonstrator Tapered C-section Laminates

2.3.1 Design of Laminates

Two demonstrator laminates were designed and manufactured to validate the design considerations discussed in sections 2.1 and 2.2. One laminate was intended as a baseline, using conventional industrial practices, such as laminate symmetry and a diamond drop-off pattern. The other was designed using a novel approach, intended to improve consolidation and reduce warpage during manufacture.

Geometry

The C-section laminates consisted of 24 plies in the (thin) far-field and were laid up on a male tool illustrated in Fig. 2.9. The 3 recesses formed pad-up regions in the laminates, where an additional 20 plies produced a total of 44 in the stack. The tapered regions (ramps) stepped into the tool by 4 mm over a longitudinal distance of 40 mm, giving a ramp rate of 1:10. The angle between the web and two flange sections was 90°, with a surface radius of 29 mm in the far-field and 25 mm in the pad-up regions.

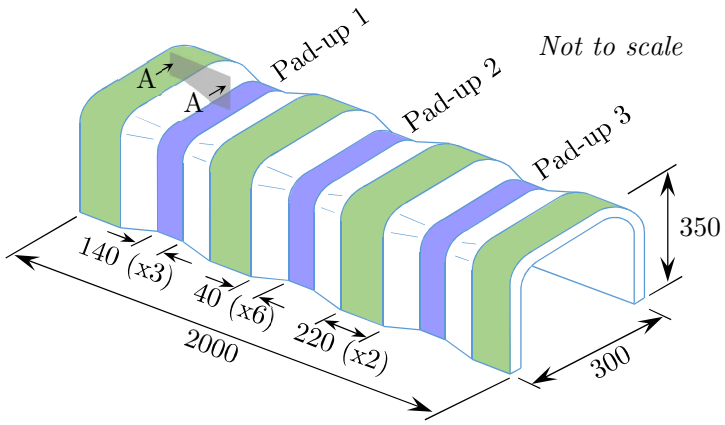

Figure 2.9 Isometric view of lay-up tool. A-A highlights one of the 1:10 ramps associated with the pad-ups. All 3 pad-ups have identical geometry; however, the inner 2 thin sections are shorter than the outer 2. Dimensions in mm.

Baseline Laminate

The baseline laminate was designed according to conventional rules used in industry [11,12]. Balanced, symmetric stacking sequences were used for both the far-field and pad-up regions, with ±45° plies positioned in pairs. The three plies adjacent to the tool and free surfaces remain continuous throughout the tapered region, with ply drops sequenced in a 'diamond' pattern, illustrated in Fig. 2.10. Note that it was not possible to maintain exact symmetry throughout the tapered region and the intermediate stacking sequences were non-symmetric. The far-field and pad-up stacking sequences were:

Far-field: $[+/-/\bigcirc/+/-/\bullet/+/-/\bigcirc/-/+/\bullet]_s$

Pad-up: $[+/-/\bigcirc/\bullet/+/-/+/-/\bullet/\bigcirc/+/-/+/-/\bigcirc/\bullet/+/-/+/-/\bigcirc/\bullet]_s$

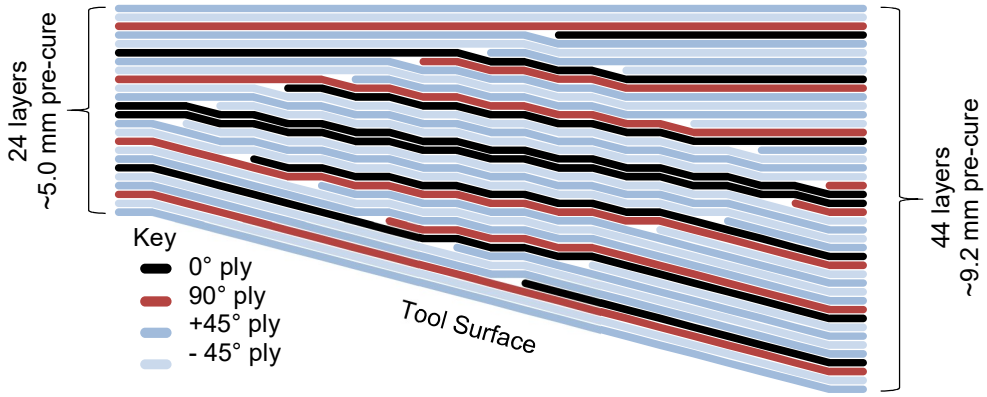

Figure 2.10 Section A-A from Fig. 2.9 for baseline laminate, showing (thin) far-field and (thick) pad-up stacking sequences, as well as the diamond drop-off pattern in the transition between thin and thick laminates.

Novel Laminate

The primary purpose of the novel laminate was to improve consolidation by positioning all continuous 0° plies within a protected zone adjacent to the tool surface. Furthermore, the novel laminate was to minimise warpage during manufacture by using fully uncoupled stacking sequences for the far-field and pad-up regions. First, the far-field stacking sequence was defined. It was determined that the 0° plies needed to be as close to the tool surface as possible in order to have as many continuous plies above the protected zone as possible to interleave with the dis-continuous plies in the pad-up. In the case of symmetric and anti-symmetric laminates, however, positioning 0° plies adjacent to the tool surface would also require the positioning of corresponding 0° plies adjacent to the free surface. This would increase the size of the protected zone, since the 0° ply furthest from the tool surface dictates its size. Therefore 0° plies were positioned close to the mid-plane of the far-field laminate. Positioning four or more identical plies adjacent to one another can increase interlaminar stresses as a result local anisotropy and is not recommended [11,12]. Therefore, the four 0° plies in the far-field were unblocked by a pair of plies, giving their final location shown on LHS of Fig. 2.11.

Having determined the position of the 0° plies, a MATLAB script was written to position the ±45° and 90° plies, such that the far-field laminate was fully uncoupled. 212 fully uncoupled anti-symmetric were found, compared with 14 symmetric. The requirement for a protected zone dictates a large portion of the pad-up stacking sequence, which must correspond with the far-field sequence within the protected zone

(the 15 plies adjacent to the tool surface on the RHS of Fig. 2.11 are identical to those on the LHS). With this constraint, no fully uncoupled symmetric stacking sequences were found for the pad-up laminate. Therefore, it was determined that an anti-symmetric laminate would be more suitable for the novel laminate. The MATLAB script was again used to find a suitable, fully uncoupled stacking sequence for the pad-up laminate, which was identical to that of the far-field laminate adjacent to the tool surface, facilitating a protected zone. The stacking sequences were:

Far-field: $[+/-/\bigcirc/+/-/+/-/\bigcirc/-/\bullet/\bullet/+]_A$

Pad-up: $[+/-/\bigcirc/+/-/+/-/\bigcirc/-/\bullet/\bullet/+/-/\bullet/\bullet/+/\bigcirc/+/-/+/\bigcirc/-]_A$

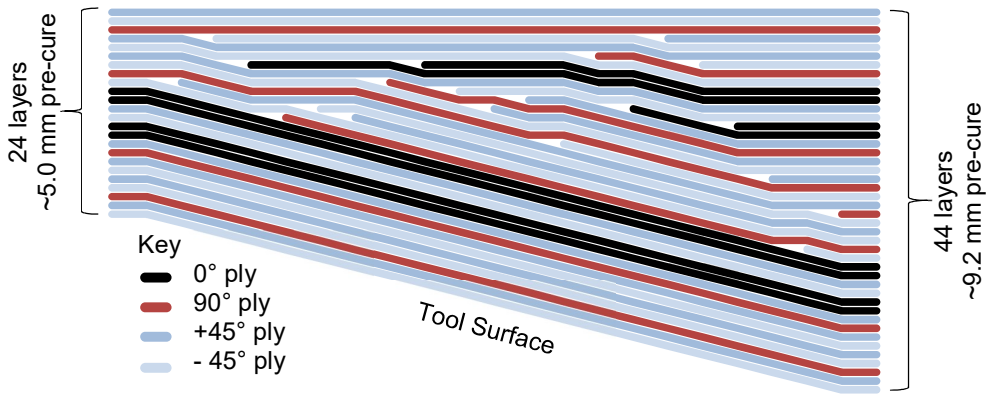

Figure 2.11 Section A-A from Fig. 2.9 for novel laminate, showing (thin) far-field and (thick) pad-up stacking sequences. The protected zone is visible in the band of 15 continuous plies that remain equidistant from the tool surface.

The ply drop-off pattern shown in Fig. 2.11 was defined by maintaining ply percentages and minimising elastic coupling. Note that it was not possible to maintain anti-symmetry throughout the tapered region and the intermediate stacking sequences were non-symmetric. Using a MATLAB script starting with the pad-up laminate, for each ply drop it was first determined whether a 0°, ±45° or 90° ply should be removed in order to cause the least deviation in ply percentages. Having done this, exactly which ply to remove was then selected as the option that produced the minimum elastic coupling, first considering in-plane to in-plane coupling as most important, then in-plane to out-of-plane, finally with out-of-plane to out-of-plane coupling considered least important. Figure 2.12 summarises the entire design process for the novel laminate.

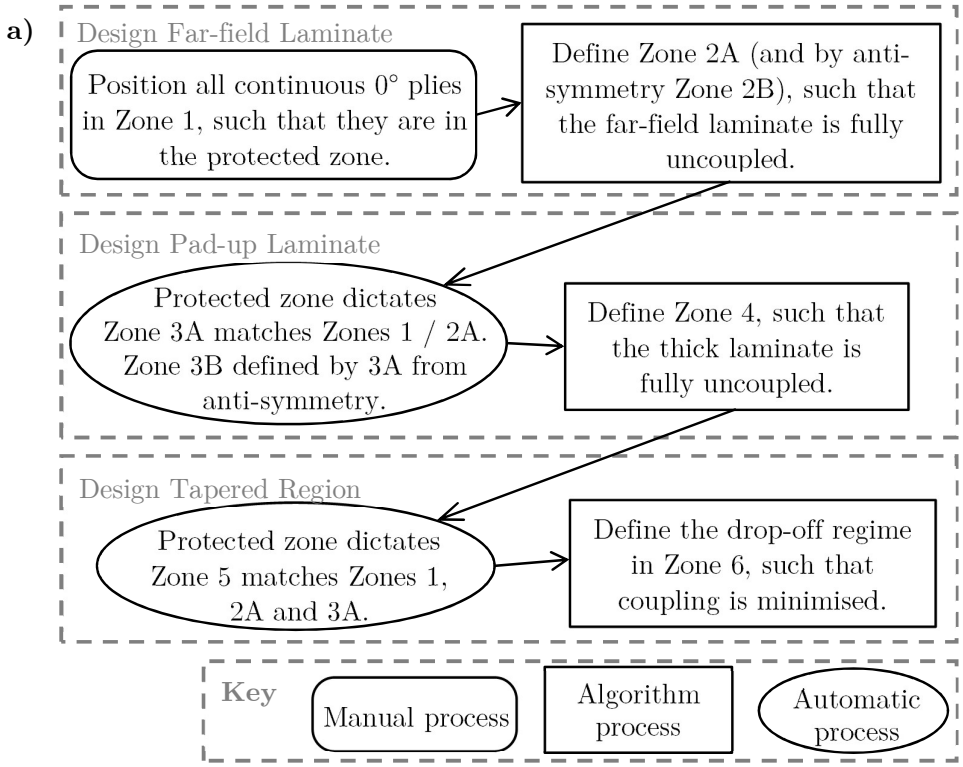

Figure 2.12 Novel laminate design process. **a)** Flow chart showing sequence of design steps. **b)** Illustration of laminate zones referred to in the flow chart. Note that the stacking sequences in Zones 1-4 are anti-symmetric, whilst Zones 5 and 6 are non-symmetric.

2.3.2 Manufacture of Laminates

The demonstrator laminates were manufactured using the same material, equipment and process. The lay-up tool was made from woven carbon fibre material such that it had similar thermal expansion properties to that of the laminates. Bagging material was laid onto the tool surface, followed by a picture frame of glass fibre (outside edge-of-part), to aid with adhesion of the first laminate ply. The laminate plies were unidirectional 8552/AS4 (194 gsm) prepreg carbon fibre, supplied by Hexcel [13]. The nominal cured ply thickness was 0.18 mm, thinner than the standard 8552/AS4 material. Deposition was performed using a Corriolis AFP machine at room temperature, with a single de-bulk after the first ply to ensure good adhesion to the tool surface. The remaining plies were all deposited before a final de-bulk, which produced the maximum consolidation movement. Interim de-bulks reduce the consolidation movement but add significant time and cost to the process so are not desirable. It was believed that the novel laminate design would tolerate this large consolidation movement better than the baseline, resulting in improved consolidation. The final de-bulk was carried out in an autoclave at 55°C with full vacuum applied for 15 minutes immediately prior to the start of the cure cycle, which was the standard cycle recommended by the manufacturer [13] and is shown in Fig. 2.13. Four vacuum ports were used to draw vacuum during the de-bulks and cure cycle; 2 on either flange of the C-section laminates, as shown in Fig. 2.14. This was to promote even consolidation and eliminate any bias towards either end of the laminate or towards one flange.

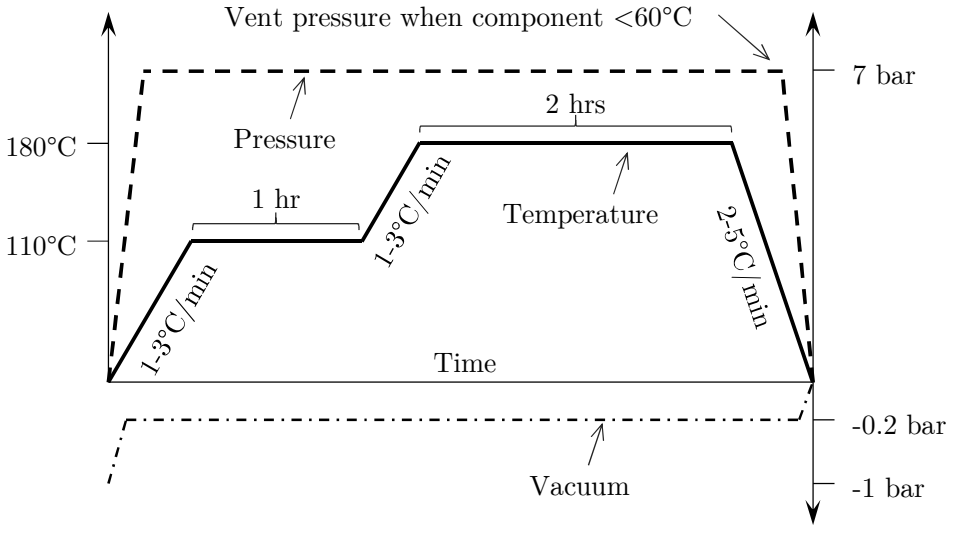

Figure 2.13 8552/AS4 cure cycle [13].

Figure 2.14 Demonstrator spar under breather clothe and vacuum bag, showing location of two vacuum ports near corners of a flange. Another two vacuum ports (out of view) are in the same location on the other flange.

2.3.3 Results

Consolidation

The C-section laminates were measured using a Brown & Sharpe CMM (co-ordinate measuring machine), using Modus software, produced by Renishaw. The data was then post-processed in SpatialAnalyzer metrology software, produced by New River Kinematics, to determine the laminate thickness using a CAD model of the tool as a reference. This was performed before and after they were de-bulked and cured in order to assess the overall change in thickness and hence the amount of consolidation. This was performed for the 3 pad-up sections and the 2 thinner sections in between the pad-ups. See Fig. 2.9 for an illustration of the 3 pad-up design. Figure 2.15 shows the thickness measurement along the length of a flange for both the novel and baseline laminates. The accuracy of the measurement equipment was ± 8 µm so the scatter seen in Fig. 2.15 is primarily caused by the surface roughness of the laminates. The amount of consolidation in the flange and web is recorded in Table 2.7 for each of the 5 flat sections (labelled in Fig. 2.15) of both laminates. The average thickness for each section in Fig. 2.15 is used to produce the consolidation data in Table 2.7, thus smoothing the apparent scatter.

Analysing Table 2.7, the novel laminate consolidated more in the majority of sections. For the few locations that the novel laminate consolidated less, it is observed that in the corresponding web/flange section, consolidation was vastly higher. For example, referring to Table 2.7, consolidation decreased by 8.6% in section 5 of the web. However, in section 5 of the flange it increased by 37.5%. It can be said of all 5 sections that overall, across the web and flange, the novel laminate showed increased consolidation. It is thought that high consolidation in a web/flange section is at the

expense of that in the adjacent web/flange of that same section. This is because edge bars were not used during the manufacture of the demonstrators. Edge bars can be positioned along the free edge of the material in the flanges to alleviate bag pressure. These help facilitate the movement of material around the C-section during consolidation by shedding excess at the free edge. Since the material was highly constrained during manufacture of the demonstrators, excess material may have been trapped. If a web or flange section consolidated particularly highly, this might be an indication that the excess material bulk was taken up in the adjacent web/flange section, causing poor consolidation in that region. Overall, the novel laminate increased consolidation by 8.7%, compared proportionately to the baseline.

Cured Ply Thickness

The consolidation data is important to understand the movement of material during the de-bulking process. This is affected by the state of the laminate both pre-consolidation and post-consolidation. However, the end objective when manufacturing composite laminates is to achieve a high quality product post-consolidation. This includes achieving the nominal cured ply thickness, which is indicative of the correct fibre volume fraction and a well-formed laminate structure.

Using the CMM data, the average cured ply thickness for each section along the novel and baseline laminates is shown in Table 2.8. The novel laminate appears to have achieved a cured thickness closer to the nominal value quoted by the manufacturer of 0.180 mm. It is important to bear in mind the accuracy of the CMM measurements of ± 0.008 mm, however it is thought since thousands of data points were taken, this error should average out in the overall results summarised in Table 2.8, as should the surface roughness of the laminates. Although the difference in cured ply thickness is relatively small between the novel and baseline laminates, the demonstrators are also relatively short (1.6 m) compared with many industrial components, which can be in excess of 10 m. It is believed the difference in cured ply thickness would be exacerbated for longer parts, where the effect of long fibres inhibiting consolidation would be greater.

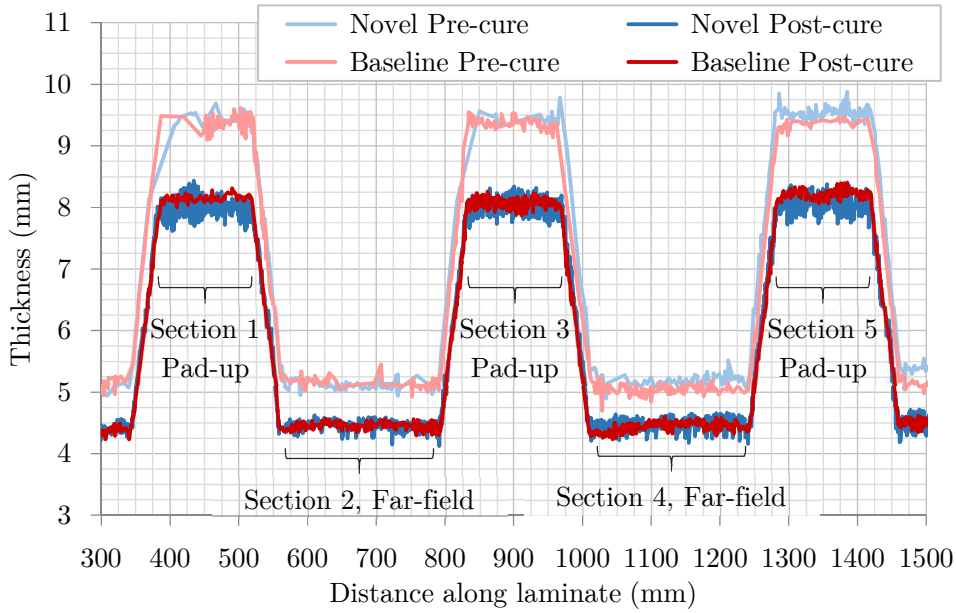

Figure 2.15 Thickness measurements along the length of a flange of the novel and baseline laminates pre- and post-consolidation and cure. The scatter is caused by surface roughness and measurement error.

	Section*	Thickness (# plies)	Consolidation (%)		$\frac{c_N}{c_B} - 1$ (%)
			c_N	c_B	
Web	1	Pad-up (44)	11.5	11.8	-2.7
	2	Far-field (24)	14.5	11.8	22.6
	3	Pad-up (44)	11.9	11.2	6.4
	4	Far-field (24)	14.7	13.9	5.9
	5	Pad-up (44)	11.3	12.4	-8.6
Flange	1	Pad-up (44)	15.6	14.3	9.6
	2	Far-field (24)	12.7	14.1	-9.8
	3	Pad-up (44)	14.9	13.5	10.5
	4	Far-field (24)	13.0	10.5	23.4
	5	Pad-up (44)	14.9	10.9	37.5
		Average	**13.5**	**12.4**	**8.7**
*refer to Fig. 2.15 for section locations.					

Table 2.7 Comparison of consolidation data for novel and baseline laminates.

Section*	Thickness (# plies)	CPT (mm)	
		Novel	Baseline
1	Pad-up (44)	0.183	0.185
2	Far-field (24)	0.180	0.184
3	Pad-up (44)	0.182	0.185
4	Far-field (24)	0.181	0.183
5	Pad-up (44)	0.183	0.185
Average	**Far-field (24)**	**0.180**	**0.183**
	Pad-up (44)	**0.183**	**0.185**
*refer to Fig. 2.15 for section locations.			

Table 2.8 Comparison of average cured ply thickness (CPT) for novel and baseline laminates.

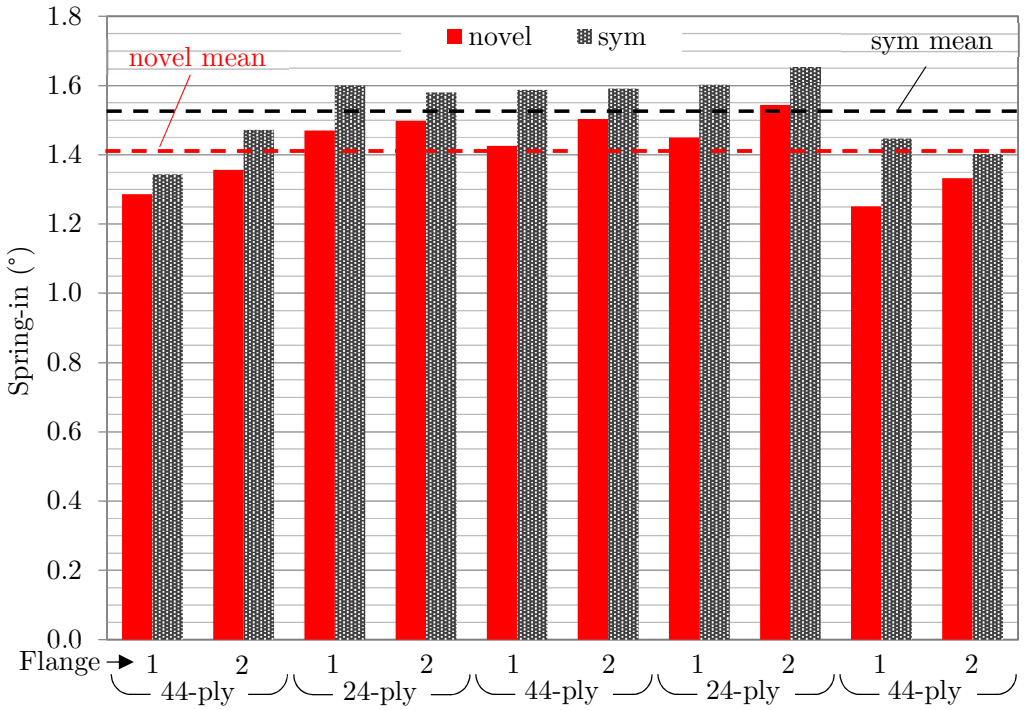

Figure 2.16 Spring-in measured in 5 sections along the length of each laminated C-section for both flanges (1 and 2).

Warpage, Spring-in and Twist

After the two laminates were cured and removed from the tool, a series of measurements were taken from their inner faces, using the same CMM equipment and software as for the consolidation measurements discussed previously. Multiple planes were created along the length of the C-sections, representing the inner faces of the web and flanges. Each plane was generated from approximately 70 data points from the CMM measurements, with a typical RMS error of 5-10 μm. The angle between the web and two flange planes could then be calculated and compared against the tool angle of 90°. This was done for 5 sections along the length of each C-section, with the results shown in Fig. 2.16. Both laminates were found to have sprung-in; the novel (mean 1.41°) slightly less than the baseline symmetric (mean 1.53°).

The level of twist of the two laminates was assessed using the planes generated from the web. Comparing the angle of each plane along the length of the C-sections produces the plot in Fig. 2.17. The observed section in Fig. 2.17 is approximately half the length of each C-section, spanning 2 thin and 2 pad-up sections. This was the maximum length that could be scanned without moving the laminate and hence disturbing the reference, potentially increasing measurement error. However, Fig. 2.17 is representative of the level of twist for the full length of each C-section. It is shown that the novel laminate exhibited approximately half the level of twist as compared with the baseline. Taking the average level of twist from Fig. 2.17 gives κ_{xy} equal to $3.3\text{x}10^{-6}$ rad/mm for the novel and $6.4\text{x}10^{-6}$ rad/mm for the baseline C-sections. This large difference is primarily as a result of bend-twist coupling present in the baseline, symmetric laminate, but which is eliminated in the constant thickness sections of the novel, anti-symmetric laminate.

Using classical laminate theory, where there is a null **B** matrix (as is the case for both demonstrator laminates), it can be stated from Eq. (2.2) that

$$M_{xy} = D_{16}\ \kappa_x + D_{26}\ \kappa_y + D_{66}\ \kappa_{xy} \quad . \tag{2.32}$$

Since there is no applied twisting moment, M_{xy}, and no x-curvature, κ_x, this can be simplified and rearranged to find

$$\kappa_{xy} = -\frac{D_{26}}{D_{66}}\ \kappa_y \quad . \tag{2.33}$$

The ratio of D_{26} and D_{66} therefore described how much the laminate will twist as a result of curvature in the y-direction, caused primarily by spring-in for the demonstrator laminates. Equation (2.33) describes a general principle that will apply

to all laminates and therefore the results of the two demonstrator laminates are likely to be representative of the general case. The ratio is approximately 9% and 6% respectively for the thin and thick sections of the baseline laminate. Since both thin and thick sections of the novel laminate are fully uncoupled and D_{26} is zero, the ratio is also zero, causing significantly reduced twist, as seen in Fig. 2.17. However, in the tapered ramp sections, where single ply terminations exist, it is not possible to maintain zero D_{26} terms. Moreover, in the presence of the corner features, the shift in neutral plane for the laminates will lead to a non-zero **B** matrix, leading to twist as a result of thermal load after manufacture.

These factors, combined with manufacturing imperfections, are likely to be the cause of the novel laminate also exhibiting twist, albeit less than the baseline. As a result of the relative level of spring-in and twist for the two demonstrator laminates, significant force was required to remove the baseline laminate from the tool, post-cure. In contrast, the novel laminate was readily removed, which is a practical testimony to the CMM data subsequently recorded.

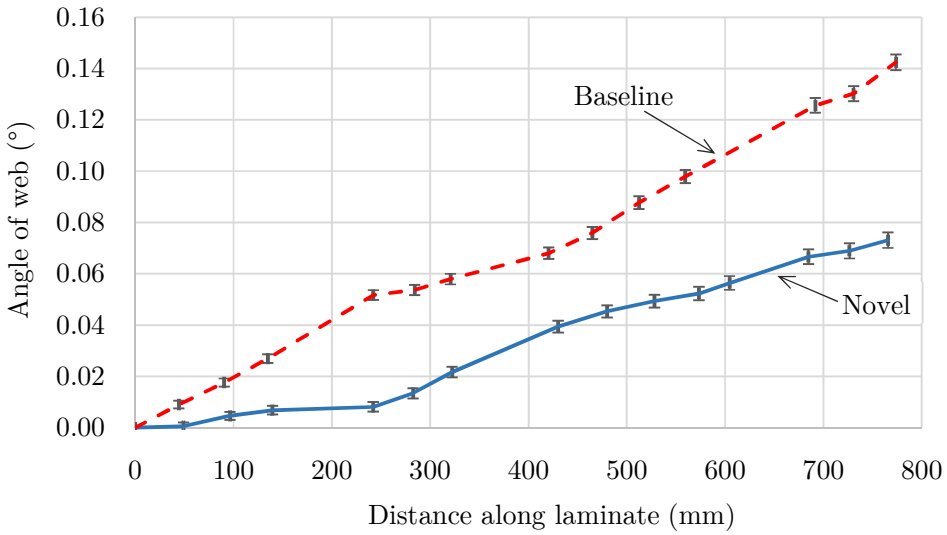

Figure 2.17 Level of twist of the two demonstrator laminates, illustrated by plotting the angle of the web along the length of the C-section, relative to the starting location. In general, the novel laminate exhibits half the level of twist compared with the baseline. Measurement error bars are shown.

2.4 Closing Remarks

The influence of symmetric and anti-symmetric stacking sequences on stiffness coupling is investigated. Equation (2.16) and Eq. (2.15) are derived as conditions that must be satisfied to produce a fully uncoupled symmetric or anti-symmetric laminate respectively. Since Eq. (2.15) is more readily satisfied mathematically, there are found to be vastly more fully uncoupled anti-symmetric stacking sequences than symmetric.

The geometrical implications of tapered regions on consolidation are studied and it is found that continuous 0° plies, running the length of a laminate, are most likely to resist consolidation. It is proposed that positioning these plies in a protected zone, such that they remain equidistant from the tool surface throughout the tapered region, will mitigate this effect. Two demonstrator laminates are designed with a web and two flanges, forming a C-section, and taper from 24 to 44 plies along their length: one with typical balanced, symmetric stacking sequences, forming a baseline; and one with more novel anti-symmetric sequences and a protected zone. The novel laminate is fully uncoupled in the 24 and 44-ply sections and the inclusion of a protected zone is only possible with the use of anti-symmetric stacking.

The two demonstrator laminates are laid up using AFP and cured in an autoclave. The novel laminate is found to increase consolidation by 8.7%, achieving a cured ply thickness closer to the nominal value quoted by the prepreg manufacturer. It also significantly reduces warpage, with 7.8% less spring-in at the flange-web corners and 48% less twisting along the length of the web. Overall the use of a novel laminate design is shown to have significant benefits for manufacturability. The performance of the novel laminate also needs to be compared against the baseline, however, which is undertaken in Chapters 3 and 4.

3 CORNER UNFOLDING

The certification process for aircraft and their components is reviewed. The 4-point bending test in the context of curved laminate certification is introduced. Experimental test results for curved laminates are presented, using 24- and 44-ply specimens cut from the baseline (S24/S44) and novel (N24/N44) demonstrators, discussed previously in Chapter 2. Also tested are 39-ply curved laminates (G39A/B), which have been manufactured to industrial standard and as such are more pristine (fewer defects). Analytical and numerical models for the prediction of curved beam strength (CBS) are reviewed and developed, including the selection of a suitable failure criterion (referred to as Camanho failure criterion).

3.1 Component Certification

The European Aviation Safety Agency (EASA) is responsible for airworthiness and environmental certification of aeronautical products, which are designed and manufactured for use in European Union (EU) member states [14]. The regulatory requirements and best practices are largely based upon documents originally prepared by the United States of America, Department of Defence, such as the Composite Materials Handbook [15]. The principal aim of these regulations is to ensure aircraft safety, which translates into inspecting the integrity of components manufactured from composite materials, insuring they will adequately perform during aircraft operation. Where possible, non-destructive testing (NDT) is desirable for inspecting composite components. NDT (also non-destructive inspection – NDI) allows every part that is manufactured to be tested without the need to destroy samples with the associated cost penalty. NDT techniques include Ultrasonic testing, X-ray, Radiography, Thermography, Eddy current, Acoustic Emission, Penetrant and Visual Inspection, which are used for various applications [16,17]. In general NDT has limitations for thick composite parts, where it becomes difficult to penetrate through the entire part.

Composite materials such as CFRP and GFRP typically have low thermal conductivity compared with metals, such as aluminium, restricting the penetration depth of flash modulation for Thermography testing [18]. However, by embedding shape memory alloy wires, a technique known as SMArt Thermography seeks to improve defect definition, especially for thicker parts [19]. Ultrasonic testing can be used to inspect relatively deep into a part, however there is a trade-off between penetration depth and the obtained resolution when setting the frequency and hence wavelength of the ultrasonic waves [18,20]. X-ray computed tomography (CT) [21] can enable inspection of a thick composite parts, through multiple delaminations. However, it is generally slower, requiring several hours for a high-resolution scan, rather than the minutes required for Thermography or Ultrasonic testing [18]. However, in certain cases where NDT is not possible, destructive tests are necessary.

> *"Destructive tests are often used to ensure the structural integrity of a component whenever assurance cannot be gained by non-destructive techniques alone. These tests include periodic dissection of the part to examine the interior of complex structures and mechanical testing of specimens cut from excess parts of the component."* Composite Materials Handbook, pages 3-6 [15].

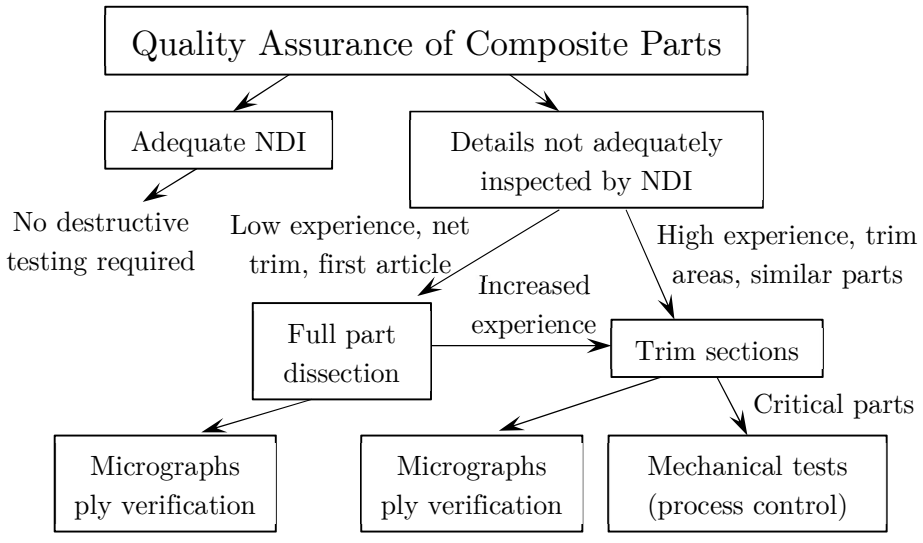

Figure 3.1 Process for ensuring quality of composite parts [15].

Figure 3.1 shows the basic principle of quality assurance and when destructive mechanical tests are carried out. The certification of aircraft is typically validated with a programme of testing. Thousands of tests are carried out on small scale coupons, with fewer and fewer carried out as the test parts get larger and more complex. This is typically carried out most rigorously for the first articles during aircraft development, with the requirement reducing during full production as experience is gained, according to Fig. 3.1. It is important that at every scale the test is representative of the final product. Trim sections are commonly taken by manufacturing a part beyond the trim line of the final product, using the excess material for testing, and offers a compromise between quality assurance and cost [15].

3.2 4-Point Bending

The response of curved laminates to corner unfolding can be assessed by conducting a 4-point bend test [22,23,24]. The 4-point bend test is commonly employed to generate interlaminar tensile stresses, though industry experience of out-of-plane strength testing is low [25]. These tests are typically carried out on small curved laminate specimens, cut away as trim sections from a large part. This means the specimens are several orders of magnitude narrower than the final product. In this chapter a number of 4-point bend tests have been carried out alongside analytical and linear FE analysis to investigate the strength of curved laminates. An illustration of an example curved laminate is shown in Fig. 3.2, although curved laminates of various dimensions were tested.

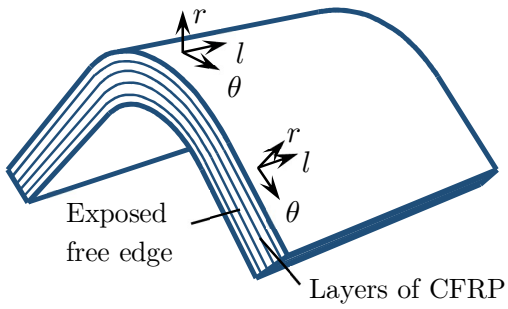

Figure 3.2 Curved laminate example illustration. The axes show the global coordinate system. Fibres in 0° plies are oriented along the l-axis and 90° plies, along the θ-axis. Not to scale.

3.2.1 Test Rig and CBS Calculation

The curved beam strength (CBS) is used as a metric for quantitatively assessing and comparing the strength of the curved laminates. CBS is defined as the applied bending moment per unit width (or running moment) at failure. The CBS of curved laminate specimens was assessed by means of a 4-point bending test. The test setup was adapted from ASTM D6415 [22]. An unfolding moment was generated by 4 rollers attached to a test rig, as shown schematically in Fig. 3.3.

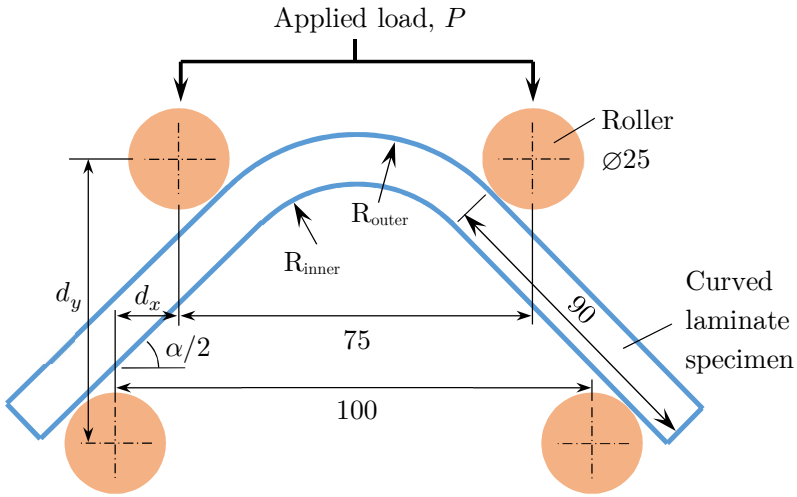

Figure 3.3 Schematic of test setup in cross-section. All dimensions in mm.

Well-lubricated, smooth steel rollers were used to ensure they rotated freely within their housings and could not transfer load into the coupon via shear, which would invalidate many of the modelling assumptions. The lower two rollers were fixed in translation (but free to rotate). The displacement of the upper two rollers was controlled by an Instron machine at a rate of 1 mm/min. By monitoring the load and displacement, the applied moment, and hence CBS, was calculated from [22] according to

$$CBS = \left(\frac{P}{2w\cos\frac{\alpha}{2}}\right)\left(\frac{d_x}{\cos\frac{\alpha}{2}} + (D+t)\tan\frac{\alpha}{2}\right) \tag{3.1}$$

$$\sin\frac{\alpha}{2} = \frac{-d_x(D+t) + d_y\sqrt{{d_x}^2 + {d_y}^2 - D^2 - 2Dt - t^2}}{{d_x}^2 + {d_y}^2} \quad , \tag{3.2}$$

where w and t are, respectively, the width and thickness of the specimen, and D is the roller diameter. All other parameters are defined according to Fig. 3.3. Note that d_y and hence α changes during the test as the upper rollers displace downwards. The values at failure were taken to calculate CBS. The selection of d_x was as small as possible to minimise vertical displacement to failure (and hence geometrical non-linearity), without being so small as to induce failure by shear in the limbs.

3.2.2 Specimen Details

Large C-section structures were manufactured from uni-directional CFRP material. Layup was performed using an AFP machine, with final cure in an autoclave. Specimens were then cut from the C-sections to produce curved laminates as shown in Figs. 3.2 and 3.3. The free edges were then finely polished to avoid artificially creating a defect at the edge, which would induce premature failure. Final specimen width was measured after this polishing process. Table 3.1 summarises nominal material and geometry data for the 6 different curved laminate types.

ID	Resin/fibre material	Cured ply thickness (mm)	No. plies	R_{inner} (mm)	α (°)	Width (mm)
G39A	M21/IMA	0.25	39	21.5	87.5	52
G39B	M21/IMA	0.25	39	21.5	85.0	52
S24	8552/AS4	0.18	24	29	91.6	25
S44	8552/AS4	0.18	44	25	91.4	25
N24	8552/AS4	0.18	24	29	91.4	25
N44	8552/AS4	0.18	44	25	91.4	25

Table 3.1 4-point bending test specimen types and nominal dimensions.

The stacking sequences for G39A/B, S24 and S44 are symmetric, while N24 and N44 are anti-symmetric. 90° fibres wrap around the corner, along the axis labelled θ in Fig. 3.2. The stacking sequences are as follows:

G39: $[(\mp 45/90/0)_2/\mp 45_2/90/\mp 45/90/0/\mp 45/0/\pm 45/0/90/\pm 45/90/\pm 45_2/(0/90/\pm 45)_2]$

S24: $[\pm 45/90/\pm 45/0/\pm 45/90/\mp 45/0]_S$

S44: $[\pm 45/90/0/(\pm 45)_2/0/90/\{(\pm 45)_2/90/0\}_2]_S$

N24: $[\pm 45/90/(\pm 45)_2/90/-45/0_2/+45]_A$

N44: $[\pm 45/90/(\pm 45)_2/90/-45/0_2/\pm 45/0_2/+45/90/\pm 45/+45/90/-45]_A$

3.2.3 Test Results

A summary of all test results for each specimen type is contained in Table 3.2. Results for each individual test are illustrated in Fig. 3.4 through Fig. 3.9, and detailed tables of results for all experimental testing can be found in Appendix B.

In general, the G39- specimens were found to be more consistent with lower standard deviation in proportion to the average CBS. This is expected since these specimens were manufactured to aerospace production standard, whereas the S- and N- specimens were not. The G39- specimens consistently exhibited failure between ply 16-38, as illustrated in Fig. 3.10 for G39B-01, which is typical of similar specimens.

The S24 specimens typically failed in one of two ways: either they failed close to the outer radius, in the vicinity of ply 3, as illustrated by the delamination in Fig. 3.11a and fibre breakage in Fig. 3.11b; or failure was more spread out with multiple delaminations extending throughout the thickness, as shown in Fig. 3.12. The N24 specimens all exhibited failure concentrated in the vicinity of ply 3, often with a single delamination between ply 3-4, as shown in Fig. 3.13. The average CBS of the N24 specimens was 10.8% lower than S24 specimens.

Failure of S44 specimens tended to be towards the inner radius, sometimes concentrated (Fig. 3.14a) but more typically relatively spread out with multiple delaminations through the thickness (Fig. 3.14b); whereas the N44 specimens very consistently exhibited failure concentrated between ply 28-36, as shown in Fig. 3.15. The significance of this is that two pairs of 0° plies are positioned in this range (plies 30-31 and plies 34-35). It is therefore likely that this concentration of 0° plies caused failure at an average CBS 11.4% lower for N44 plies, compared with S44. This is interesting because there are standard guidelines for stacking sequences [11,12], which state that no more than 3 plies with the same fibre orientation may be positioned adjacent to one another, although 4 is acceptable if the total thickness does not exceed 1 mm. In the case of the N44 specimens, only 2 plies of the same orientation (0°) have been positioned adjacent to one another but it appears to have reduced the strength significantly.

Specimen type	(kNmm/mm)		Typical failure location
	CBS	S.D.	
G39A	7.86	0.20	ply 16-38
G39B	7.49	0.22	ply 16-38
S24	2.04	0.12	ply 1-24 (all)
S44	4.28	0.20	ply 18-44
N24	1.82	0.15	ply 1-8
N44	3.79	0.45	ply 28-36

Table 3.2 Average CBS and standard deviation for each specimen type. An indication of the location that delaminations typically occur is also shown, with ply 1 at the outer radius.

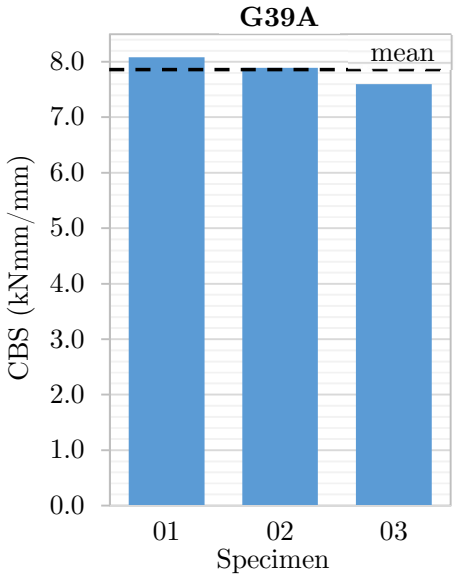

Figure 3.4 G39A test results.

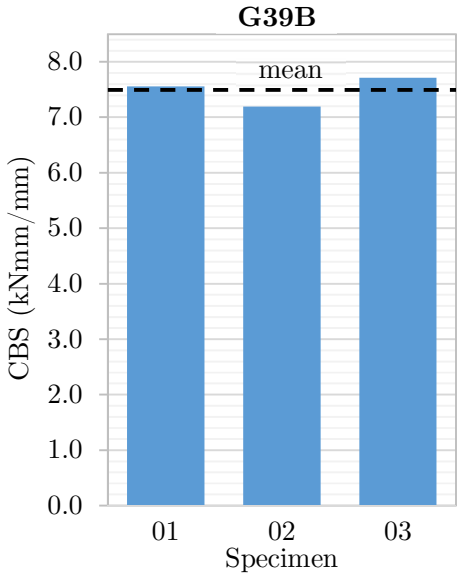

Figure 3.5 G39B test results.

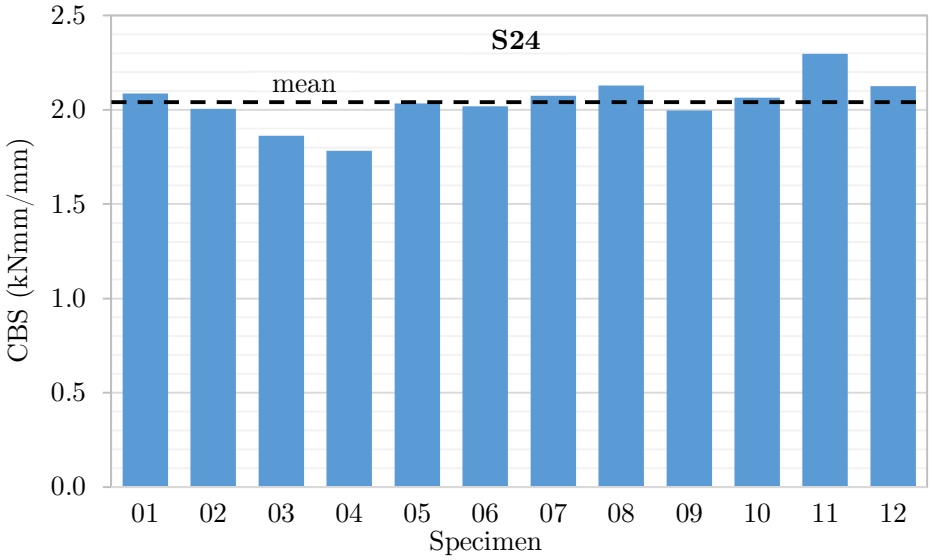

Figure 3.6 S24 specimen test results.

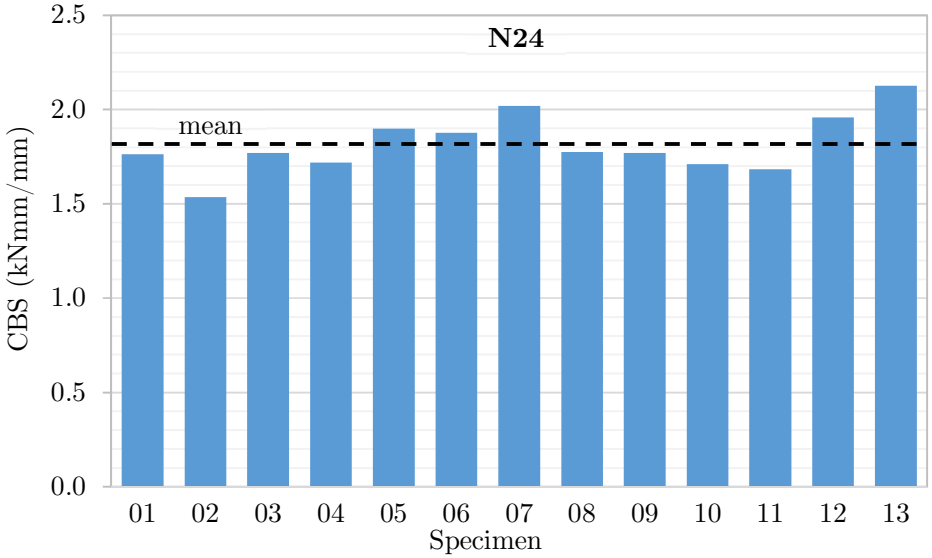

Figure 3.7 N24 specimen test results.

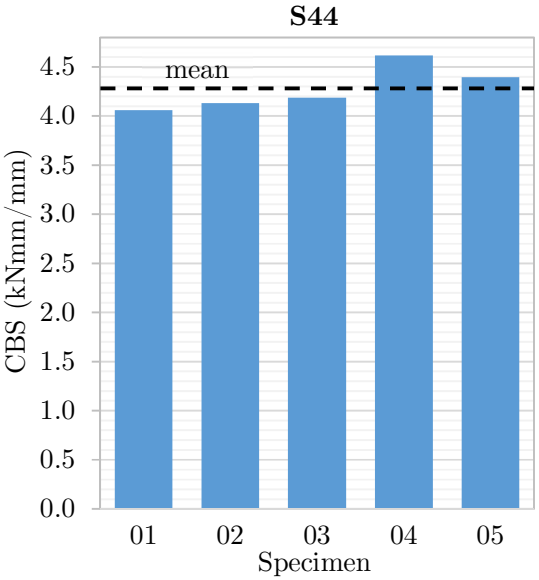

Figure 3.8 S44 test results.

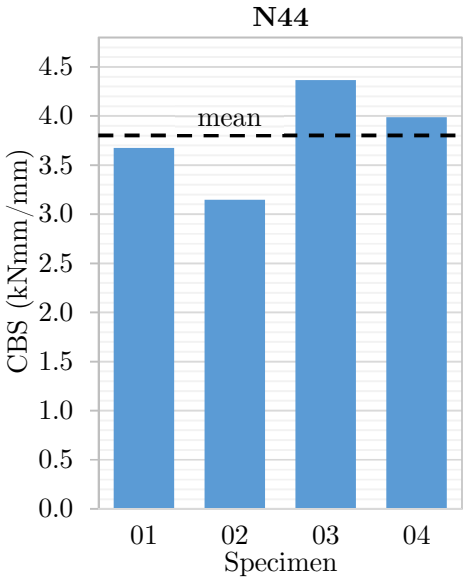

Figure 3.9 N44 test results.

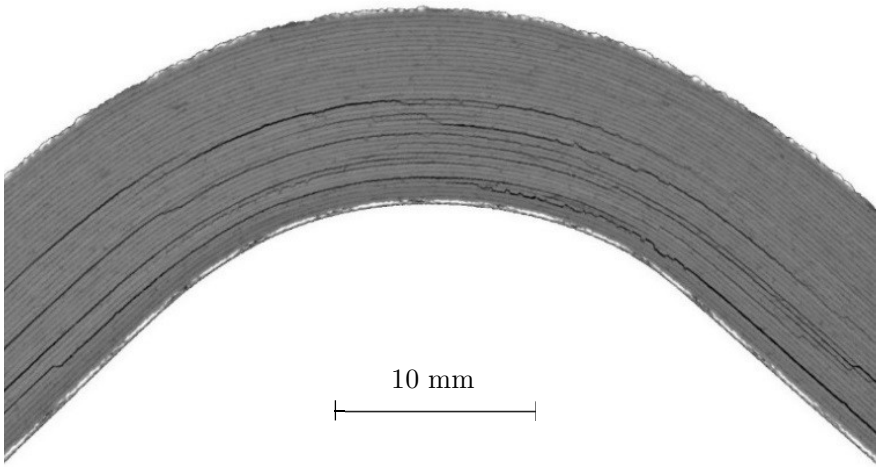

Figure 3.10 Post-test CT scan cross-section of specimen G39B-01. Failure locations are within approximately the inner half of the laminate only (ply 16-38), towards the inner radius.

a) 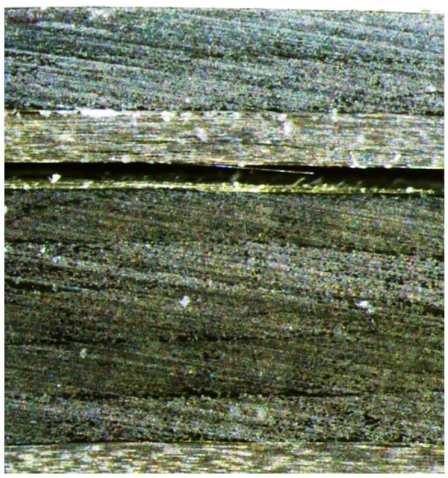 b) 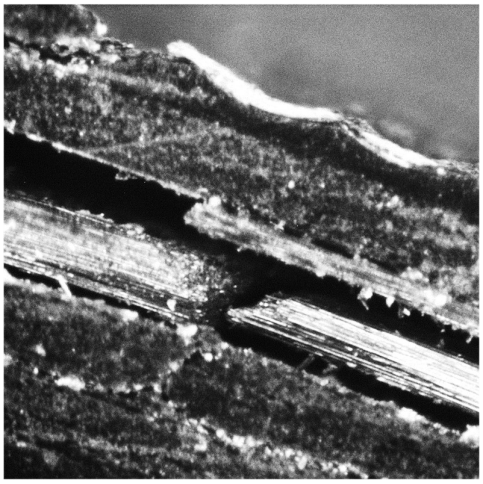

Figure 3.11 Post-test micrographs of S24 specimens. **a)** S24-12, failure location is close to the outer radius, at the inner edge of ply 3 (a 90° ply) and within interface 3 (between plies 3-4). **b)** S24-10, fibre breakage of ply 3.

a) b) 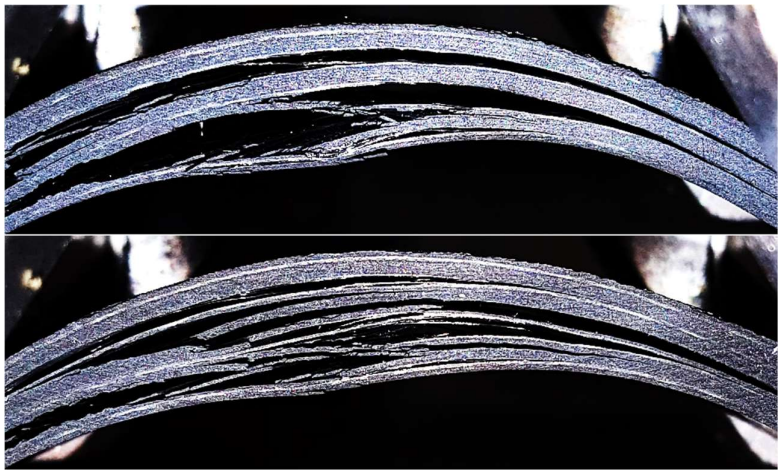

Figure 3.12 Images of S24 specimens at point of failure, showing failures closer to inner radius. **a)** S24-05, ply 8-24. **b)** S24-06, ply 7-24.

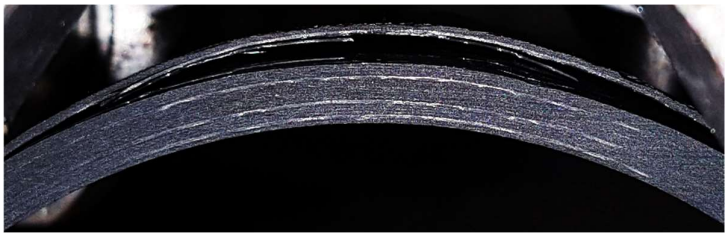

Figure 3.13 Image of N24-05 at point of failure, showing failure concentrated near outer radius (ply 3-4).

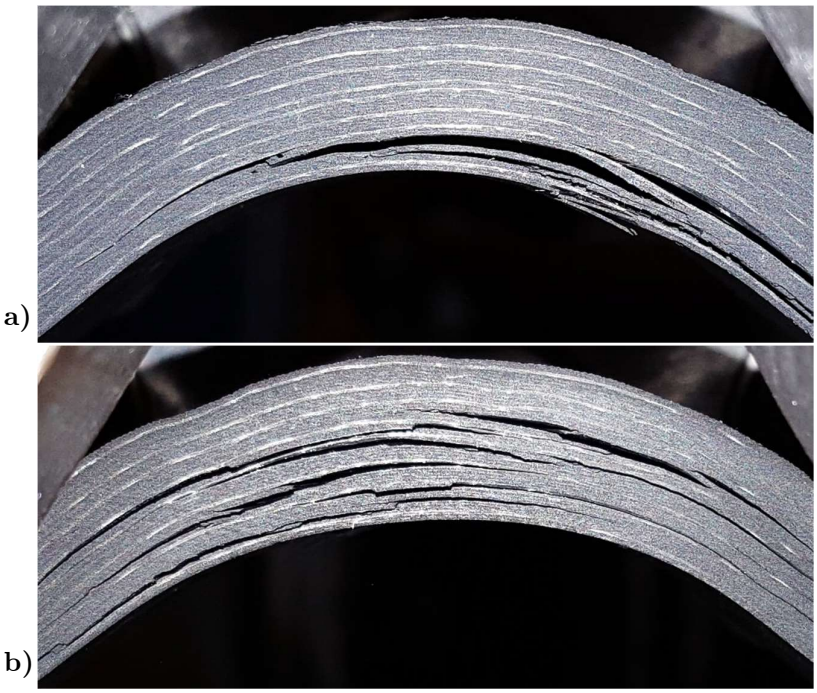

Figure 3.14 Images of S44 specimens at point of failure, showing different failure locations. **a)** S44-04, concentrated close to inner radius (ply 34-44). **b)** S44-05, spread closer to outer radius (ply 18-44).

Figure 3.15 Images of N44 specimens at point of failure, showing consistent, concentrated failure location. **a)** N44-03, ply 29-36. **b)** N44-04, ply 29-36.

3.3 Analytical Model

A simple analytical model that accurately predicts the CBS of curved laminates, taking account of stacking sequence, is sought in this section of the chapter. This could then be used to investigate different laminate designs and determine key features of the stacking sequence that affect CBS. Under the action of a corner unfolding moment, composite laminates commonly fail by delamination, caused by failure of the matrix material bonding the layers together. This is evident in all the specimens tested, as shown in Figs. 3.10 through 3.15. Therefore, a suitable analytical model would be one that predicts the maximum radial stress, $\sigma_{r\,max}$, and at what unfolding moment this reaches the strength limit of the matrix material.

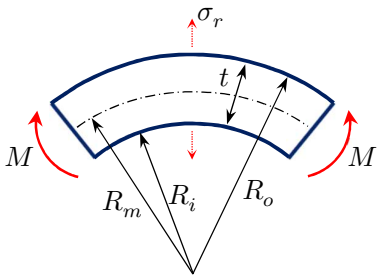

Figure 3.16 Curved laminate, showing the applied unfolding moment, M, and induced radial stress, σ_r. The width of the laminate is b.

Referring to Fig. 3.16, the maximum radial stress induced in a curved member of constant rectangular cross section is readily calculable from [26]

$$\sigma_{r\,max} = \frac{3M}{2btR_m} \quad , \tag{3.3}$$

for thin members, where $R_o \approx R_i$. Eq. (3.3) assumes that the maximum radial stress occurs at the mean radius, R_m. This is not completely accurate and solving for the correct radial location yields improved accuracy, as per an alternative equation, given by [27] as

$$\left|\sigma_{r\,max}\right| = \frac{12M}{bt^3}\left[\sqrt{R_i(R_i+t)} - R_i\frac{t}{2}\right] \quad , \tag{3.4}$$

which reduces to

$$\sigma_{r\,max} = \frac{12M}{bt^3}\left[R_m - \sqrt{R_iR_o}\,\right] \quad . \tag{3.5}$$

The derivation of Eq. (3.3) and (3.5) is from simple bending theory, based upon the assumption of linearly distributed circumferential stress. These expressions give reasonable results for isotropic materials but are slightly unconservative compared to exact methods [28]. The major error in Eq. (3.3) arises from solving for $\sigma_{r\,max}$ at the incorrect radial location and substituting the correct value from Eq. (3.5) gives the expression

$$\sigma_{r\,max} = \frac{3M}{2bt\sqrt{R_i R_o}} \quad , \tag{3.6}$$

which is shown in [28] to have a significantly smaller error than Eq. (3.3) and (3.5), relative to a classical elasticity solution [29]. The assumption $R_o \approx R_i$ is not valid for the curved laminates tested in Section 3.2.3, particularly the thicker specimens. According to [28] the expected error in $\sigma_{r\,max}$ estimation would be up to 4% using Eq. (3.3) or (3.5), however using Eq. (3.6) it would be <1%. Since M/b = CBS, Eq. (3.6) can be rearranged to estimate CBS assuming $\sigma_{r\,ma}$ is equal to the normal tensile strength of the curved laminate, i.e. in the direction of the force σ_r in Fig. 3.16.

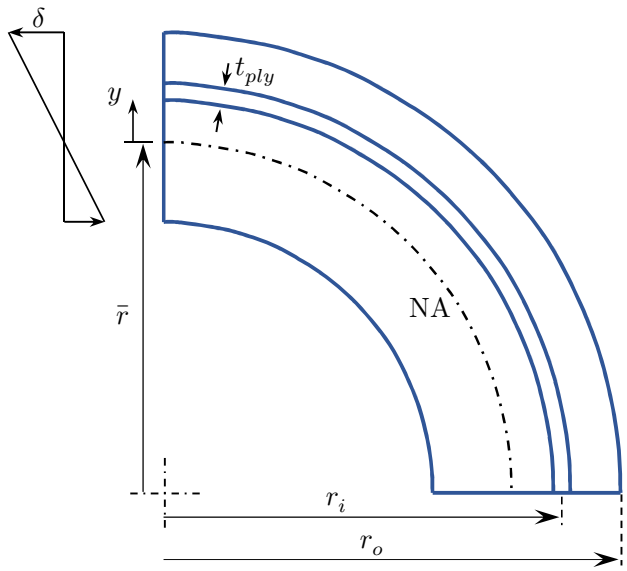

Figure 3.17 Curved laminate with outer radius r_o and neutral axis at $\bar{r}$. A ply of thickness t_{ply} at a mean radius r_i is illustrated. Assuming plane sections remain plane, the deflection through thickness is shown to the left of the laminate.

3.3.1 Layer-wise Analytical Model

Equation (3.6) was found to be inaccurate for predicting laminate CBS and does not take account of different laminate stacking sequences. A more refined model, which does take stacking sequence into account is sought. An Airbus document [30] presents a layer-wise, plane strain 2D model for assessing radial and circumferential stresses in a curved composite laminate. This is primarily derived from Lekhnitskii [31].

Consider the curved laminate in Fig. 3.17. Assuming a linear variation of deflection through thickness, the deflection profile to the left of Fig. 3.17 can be described by

$$\delta = -ay \quad , \tag{3.7}$$

$$y = r - \bar{r} \quad , \tag{3.8}$$

$$\delta = -a(r - \bar{r}) \quad , \tag{3.9}$$

where a describes the slope of the deflection profile. Taking the strain over a unit area and substituting from Eq. (3.9) gives

$$\varepsilon_\theta = \frac{\delta}{r\theta} = -\frac{a(r - \bar{r})}{r.1} \quad , \tag{3.10}$$

$$\varepsilon_\theta = a\left(\frac{\bar{r}}{r} - 1\right) \quad . \tag{3.11}$$

It is assumed that circumferential stress and strain are linked by

$$\sigma_{\theta i} = k_i \, \varepsilon_{\theta i} \quad , \tag{3.12}$$

where k_i describes the stiffness of ply i in the global tangential direction and is found using classical laminate theory as follows.

$$\boldsymbol{S} = \begin{bmatrix} \frac{1}{E_{11}} & -\frac{v_{12}}{E_{11}} & 0 \\ -\frac{v_{12}}{E_{11}} & \frac{1}{E_{22}} & 0 \\ 0 & 0 & \frac{1}{G_{12}} \end{bmatrix} \quad , \tag{3.13}$$

$$\boldsymbol{Q} = \boldsymbol{S}^{-1} \quad , \tag{3.14}$$

$$\boldsymbol{T} = \begin{bmatrix} \cos^2\phi & \sin^2\phi & \sin\phi\cos\phi \\ \sin^2\phi & \cos^2\phi & -\sin\phi\cos\phi \\ -2\sin\phi\cos\phi & 2\sin\phi\cos\phi & (\cos^2\phi - \sin^2\phi) \end{bmatrix} \quad , \tag{3.15}$$

$$\overline{\boldsymbol{Q}} = \boldsymbol{T}^T \boldsymbol{Q} \boldsymbol{T} \quad , \tag{3.16}$$

$$k_i = \overline{Q}_{22} \quad , \tag{3.17}$$

where $\overline{Q}_{22}$ describes the stiffness of the ply in the θ-direction, from Fig. 3.2. For stress equilibrium on a plane section of n plies

$$\sum_{i=1}^{n} \sigma_i \; t_{ply} = 0 \tag{3.18}$$

and substituting from Eq. (3.11) and (3.12)

$$\sum_{i=1}^{n} k_i \; \varepsilon_{\theta i} \; t_{ply} = 0 \quad , \tag{3.19}$$

$$\sum_{i=1}^{n} k_i \; a \left(\frac{\bar{r}}{r_i} - 1 \right) \; t_{ply} = 0 \quad . \tag{3.20}$$

This can be rearranged to find the position of the neutral axis,

$$\bar{r} \sum_{i=1}^{n} \frac{k_i}{r_i} \; a \; t_{ply} = \sum_{i=1}^{n} k_i \; a \; t_{ply} \quad , \tag{3.21}$$

$$\bar{r} = \sum_{i=1}^{n} k_i \Big/ \sum_{i=1}^{n} \frac{k_i}{r_i} \quad . \tag{3.22}$$

The standard result for neutral axis position in a curved beam of isotropic material is given by [32]

$$\bar{r} = \frac{A}{\int \left(\frac{dA}{r} \right)} \quad , \tag{3.23}$$

where A is the cross-sectional area and r is the radius. Equation (3.22) is similar to Eq. (3.23) but accounts for the anisotropy of composite laminates caused by the variation in ply stiffness in the circumferential direction, k_i.

For moment equilibrium under the action of an applied moment M,

$$\sum_{i=1}^{n} \sigma_i \; t_{ply} \; y_i = -M \quad . \tag{3.24}$$

Substituting from Eq. (3.8), (3.11) and (3.12) and rearranging gives

$$\sum_{i=1}^{n} k_i \; \varepsilon_{\theta i} \; (r_i - \bar{r}) = -\frac{M}{t_{ply}} \quad , \tag{3.25}$$

$$\sum_{i=1}^{n} k_i \; a \left(\frac{\bar{r}}{r_i} - 1 \right) \; (r_i - \bar{r}) = -\frac{M}{t_{ply}} \quad , \tag{3.26}$$

$$\sum_{i=1}^{n} k_i \; a \left(2\bar{r} - r_i - \frac{\bar{r}^2}{r_i} \right) = -\frac{M}{t_{ply}} \quad . \tag{3.27}$$

Substituting from Eq. (3.22) gives

$$a \left\{ \frac{2(\sum k_i)^2}{\sum \frac{k_i}{r_i}} - \sum k_i \; r_i - \sum \frac{k_i}{r_i} \cdot \frac{(\sum k_i)^2}{\left(\sum \frac{k_i}{r_i} \right)^2} \right\} = -\frac{M}{t_{ply}} \quad , \tag{3.28}$$

where all summations are for $i = 1 \rightarrow n$ (not indicated in the equation for clarity). This can be rearranged to find the expression

$$a = -\frac{M}{t_{ply} \left\{ \frac{(\sum k_i)^2}{\sum \frac{k_i}{r_i}} - \sum k_i \; r_i \right\}} \quad . \tag{3.29}$$

A MATLAB script has been written which systematically goes through a user defined laminate layer-by-layer, calculating the 3 summation required by Eq. (3.22) and (3.29). It is then possible to calculate the circumferential strain and stress in each layer from Eq. (3.11) and (3.12) respectively, which is also performed by the script.

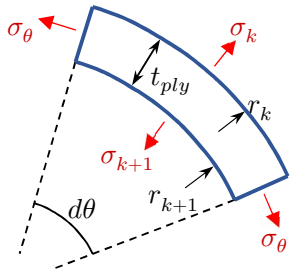

Figure 3.18 Small element, $d\theta$, of k^{th} ply with outer radius r_k and inner radius r_{k+1}. Circumferential stress, σ_θ, and radial stresses, σ_k and σ_{k+1}, are illustrated.

Now consider ply equilibrium, referring to Fig. 3.18. Since the circumferential stresses have now already been calculated for each ply, it is possible to go through the laminate layer-by-layer and calculate the radial stress. Multiplying the stresses in Fig.

3.2 by the area over which they act (assuming unit width) and equating forces in the radial direction to zero gives

$$\sigma_k \; r_k \; d\theta - \sigma_{k+1} \; r_{k+1} \; d\theta - 2 \; \sigma_\theta \; t_{ply} \frac{d\theta}{2} = 0 \tag{3.30}$$

for small $d\theta$, which simplifies to

$$\sigma_k \; r_k \; - \sigma_{k+1}(r_k - t_{ply}) \; - \sigma_\theta \; t_{ply} = 0 \quad . \tag{3.31}$$

If r_o is the outer radius of the laminate then

$$r_k = r_o - (k-1)t_{ply} \tag{3.32}$$

and

$$\sigma_k \; [r_o - (k-1)t_{ply}] \; - \sigma_{k+1}[r_o - k \; t_{ply}] \; - \sigma_\theta \; t_{ply} = 0 \quad , \tag{3.33}$$

$$\sigma_k \; \left[\frac{r_o}{t_{ply}} - (k-1)\right] - \sigma_{k+1} \left[\frac{r_o}{t_{ply}} - k \; \right] - \sigma_\theta = 0 \quad . \tag{3.34}$$

Using Eq. (3.34) for the outermost ply and applying the boundary condition $\sigma_k = 0$ at $k = 1$, it is possible to find the radial stress between ply 1 and 2 according to

$$\sigma_{k+1} = \sigma_2 = -\frac{\sigma_{\theta 1}}{\left[\frac{r_o}{t_{ply}} - 1 \; \right]} \quad . \tag{3.35}$$

Applying Eq. (3.34) for $k = 2$ and substituting from Eq. (3.35) gives

$$\sigma_2 \; \left[\frac{r_o}{t_{ply}} - 1\right] - \sigma_3 \left[\frac{r_o}{t_{ply}} - 2 \; \right] - \sigma_{\theta 2} = 0 \quad , \tag{3.36}$$

$$-\sigma_{\theta 1} \; \frac{\left[\frac{r_o}{t_{ply}} - 1\right]}{\left[\frac{r_o}{t_{ply}} - 1\right]} - \sigma_3 \left[\frac{r_o}{t_{ply}} - 2 \; \right] - \sigma_{\theta 2} = 0 \quad , \tag{3.37}$$

$$\sigma_3 = -\frac{\sigma_{\theta 1} + \sigma_{\theta 2}}{\left[\frac{r_o}{t_{ply}} - 2 \; \right]} \quad . \tag{3.38}$$

In the general case, applying Eq. (3.34) for the k^{th} ply

$$\sigma_{k+1} = -\frac{\sum_{i=1}^{k} \; \sigma_{\theta i}}{\left[\frac{r_o}{t_{ply}} - k \; \right]} \quad . \tag{3.39}$$

This is implemented in MATLAB to rapidly find the direct through thickness stress distribution within a user defined curved laminate.

Having found the stress distribution within the laminate subject to a certain applied moment, it is necessary to determine when this stress will cause failure in order to predict laminate strength. Two failure criteria have been identified which deal with in-plane failure and out-of-plane failure. The Yamada-Sun failure criterion [33] states that in-plane failure occurs when

$$\begin{aligned} \left(\frac{\sigma_{11}}{f_{11}^t}\right)^2 + \left(\frac{\tau_{12}}{f_{12}}\right)^2 = 1 \qquad \text{for } \sigma_{11} > 0 \\ \left(\frac{\sigma_{11}}{f_{11}^c}\right)^2 + \left(\frac{\tau_{12}}{f_{12}}\right)^2 = 1 \qquad \text{for } \sigma_{11} < 0 \ , \end{aligned} \tag{3.40}$$

where σ_{11} is the direct in-plane stress, τ_{12} is the in-plane shear stress and f_{11}^t, f_{11}^c and f_{12} are the in-plane tension, compression and shear allowables respectively. Note that where τ_{12} does not apply for this plane strain model, τ_{13} can be used instead. The Kim-Soni failure criterion [34] states that out-of-plane failure occurs when

$$\frac{{\sigma_{33}}^2}{f_{33}^t \, f_{33}^c} + \left(\frac{\tau_{13}}{f_{13}}\right)^2 + \left(\frac{1}{f_{33}^t} - \frac{1}{f_{33}^c}\right)\sigma_{33} = 1 \quad , \tag{3.41}$$

where σ_{33} is the direct through-thickness stress, τ_{13} is the out-of-plane shear stress and f_{33}^t, f_{33}^c and f_{13} are the out-of-plane tension, compression and shear allowables respectively.

In order to calculate the failure moment, it is necessary to extract the relevant stresses for the failure criteria, Eq. (3.40) and Eq. (3.41), from the model. Since the failure criteria are based on the local ply co-ordinate system, it is necessary to transform the global strains. This is readily achieved according to

$$\begin{aligned} \varepsilon_1 &= \varepsilon_l \cos^2\phi + \varepsilon_\theta \sin^2\phi + \gamma_{l\theta} \sin\phi \cos\phi \\ \epsilon_2 &= \varepsilon_l \sin^2\phi + \varepsilon_\theta \cos^2\phi - \gamma_{l\theta} \sin\phi \cos\phi \\ \gamma_{12} &= 2(\varepsilon_\theta - \varepsilon_l)\sin\phi\cos\phi + \gamma_{l\theta}(\cos^2\phi - \sin^2\phi) \end{aligned} \tag{3.42}$$

as documented by [35], where l and θ denote global axes, 1 and 2 denote local axes and ϕ is the angle between them, i.e. the fibre angle. Considering the plane strain model, ε_θ can be calculated for each ply from Eq. (3.11), while ε_l and $\gamma_{l\theta}$ are not generated since it is a plane strain model. Using the material's modulus, E_{11}, and shear modulus, G_{12}, the strains can be used to calculate stresses σ_{11} and τ_{12} and hence predict in-plane

failure from Eq. (3.40). For out-of-plane failure, σ_{33} is calculated for each ply according to Eq. (3.39) and fed into Eq. (3.41).

3.3.2 Assumed Material Properties

Accurate material properties are important for the overall accuracy of any model. The fibre reinforced plies of the M21/IMA material are assumed to have a thickness of 0.23 mm, with a 0.02 mm interface layer of pure resin between each ply. This is primarily based upon measurements taken from micrograph images. However, there is not a clear boundary between ply and interface, which means there is an element of subjectivity when measuring thickness, of the interface layer in particular. Sample micrographs can be seen in Fig. 3.19 and Fig. 3.20. The 0.02 mm interface thickness is considered a representative average of the significant variations seen in these micrographs. A comparable interface thickness of 0.019 mm has been measured by other researchers for a similar material (M21/T700) [10]. Micrographs indicate a similar interface thickness for 8552/AS4 and so the ply and interface thickness are assumed to be 0.16 mm and 0.02 mm, respectively, for this material. A sensitivity analysis is presented in Section 5.2.1 to address the uncertainty regarding ply and interface thickness.

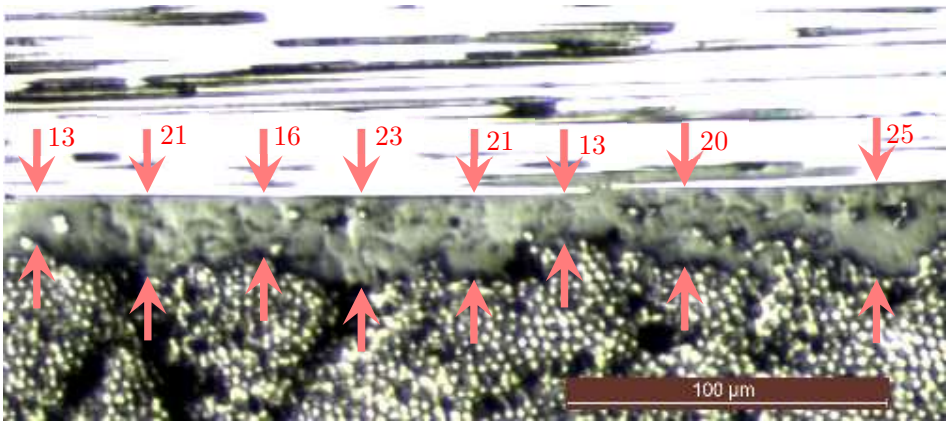

Figure 3.19 Micrograph of interface layer between a 90° and 0° ply. The thickness of the interface is indicated at various locations in µm.

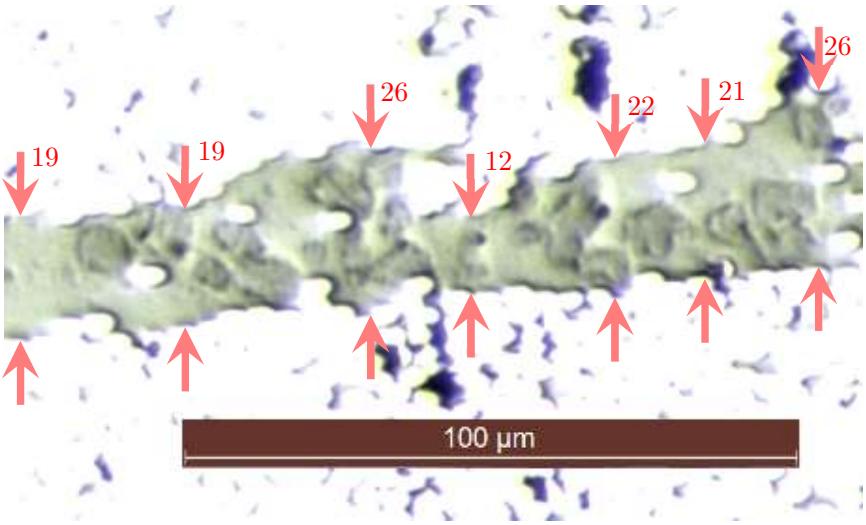

Figure 3.20 Micrograph of interface layer between a +45° and –45° ply. The thickness of the interface is indicated at various locations in µm.

The assumed mechanical properties for both resin-fibre systems are in Table 3.3. E_{11} was found by averaging the 0° tensile and compression moduli, which are quoted in the Hexcel datasheets for M21/IMA [36] and 8552/AS4 [13]. The 90° tensile modulus for 8552/AS4 is given as 10 GPa [13] and this value is therefore taken for E_{22}. The 90° tensile modulus is not quoted for M21/IMA, however M21 is derived from the resin system 8552 and since the resin will dominate E_{22}, the same value is taken for M21/IMA. Also, a dynamic characterisation of M21/T700GC [37] found values for E_{22} ranging between 10.10 - 10.56 GPa. Although this is a different fibre, again the resin will dominate, such that similar values can be expected for M21/IMA. In-plane shear modulus for M21/IMA is quoted as 5.2 GPa [36]. The in-plane shear modulus of 8552/AS4 has been found experimentally to be 4.9 GPa [38]. The Poisson's Ratio is not listed in either material datasheet but has been found experimentally to be 0.3 for 8552/AS4 [38]. The same value is assumed for M21/IMA. All allowables for 8552/AS4 are taken from the datasheet [13], except for f_{22}^c, which is not quoted and taken instead from [39]. Allowables for M21/IMA are taken from the datasheet [36], except for f_{22}^t and f_{22}^c, which are not quoted and taken instead from [40]. Note that all 2 and 3 direction moduli and strength allowables are assumed equal for the plain strain model.

	M21/IMA	8552/AS4
E_{11} (GPa)	162	135
E_{22} (GPa)	10	10
G_{12} (GPa)	5.2	4.9
v_{12}	0.3	0.3
f_{11}^t (MPa)	3050	2207
f_{11}^c (MPa)	1500	1531
f_{12} (MPa)	94	114
f_{22}^t (MPa)	61	81
f_{22}^c (MPa)	189	250

Table 3.3 Assumed mechanical properties for CFRP materials, where 1 is the fibre direction in-plane, 2 is perpendicular to the fibre direction in-plane and 3 is out-of-plane.

3.3.3 Layer-wise Analytical Model Predictions

The accuracy of the model is investigated by implementing the dimensions and mechanical properties of the 6 laminates in Table 3.1 and Table 3.3. This gives the predictions in Table 3.4 for CBS, compared against experimental data. The plane strain model over-predicts curved laminate strength, especially in the case of the S44 and N44 laminates. There is also generally poor correlation between predicted failure location and that observed experimentally. The physical test specimens are 3D and have exposed free edges where they have been cut from larger components. The effect of this is not captured in the model since it is plane stain, effectively assumed to be infinitely wide. It is clear that the plain strain model is inadequate for predicting CBS and the edge effect must be considered to improve accuracy.

Laminate ID	Model Prediction for CBS (kNmm/mm)				Experimental Results	
	YS	Critical location	KS	Critical location	Average CBS	Failure location
G39A	12.3	Ply 3	**10.1**	**Int. 23**	7.86	16-38
G39B	12.3	Ply 3	**10.1**	**Int. 23**	7.49	16-38
S24	**3.22**	**Ply 3**	8.16	Int. 13	2.04	1-24 (all)
S44	**9.49**	**Ply 3**	13.8	Int. 25	4.54	18-44
N24	**3.39**	**Ply 3**	8.20	Int. 15	1.82	1-8
N44	**9.85**	**Ply 3**	14.4	Int. 25	4.10	28-36

Table 3.4 Predicted CBS based on Yamada-Sun and Kim-Soni failure criteria, compared to experimental results. Failure locations are also shown.

3.4 Finite Element Modelling

FE analysis using commercial software Abaqus is used to model the curved laminates in 3D and take account of the free edges. It has been found that accurate modelling requires the inclusion of finite-thickness inter-ply layers [41]. It is believed that these resin rich interfaces between plies have a strong influence on laminate strength. These are modelled as isotropic layers with the mechanical properties of the resin. In the fibrous layers, individual fibres are not modelled due to computational performance constraints, however the layers are modelled as anisotropic to take account of the orientation of the fibres.

3.4.1 Assumed Material Properties

The assumed mechanical properties for both the fibrous ply material and the resin rich interface material are given in Table 3.5 for M21/IMA. The fibrous properties are taken from Table 3.3, with the exception of G_{23} and all Poisson's Ratio terms, which are taken from [40]. The f_{13} allowable is taken from [36].

Orthotropic fibrous layer		**Isotropic interface layer**	
E_{11}	162 GPa	E	10 GPa
E_{22}, E_{33}	10 GPa	v	0.35
G_{12}, G_{13}	5.2 GPa		
G_{23}	3.5 GPa	**Allowables**	
v_{12}, v_{13}	0.35	f_{33}^t	61 MPa
v_{23}	0.5	f_{13}	97 MPa

Table 3.5 Assumed mechanical properties for M21/IMA, where 1 is the fibre direction in-plane, 2 is perpendicular to the fibre direction in-plane and 3 is out-of-plane. f_{33}^t is the direct tensile through-thickness strength and f_{13} is the longitudinal shear strength.

3.4.2 Model Simplification

Modelling the full 3D bending test with rollers (illustrated in Fig. 3.3) and contact analysis would be extremely computationally expensive and restrict mesh fidelity. Therefore a simplified model is used. Curved laminates are modelled with shortened limbs, approximately equal to the thickness of the laminate. A moment is applied to the end of one limb using a beam multi-point constraint (MPC), with all degrees of

freedom fixed at the end of the opposite limb. Figure 3.21 illustrates this in 2D for clarity, however the model used is 3D. Whilst this does not accurately model stresses in the limbs, it gives the same stress field towards the apex of the curved section as a full model with rollers. In this region there is a pure moment (without shear) caused by the roller displacement. Since this is the critical region where failure occurs during the tests, this implies the simplified model is suitable for predicting CBS.

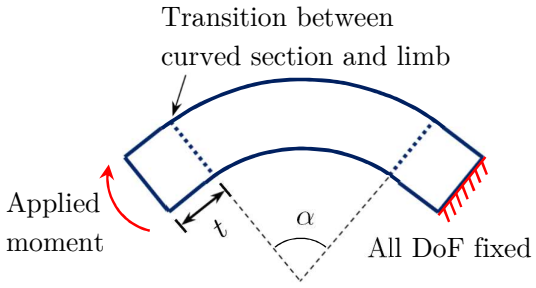

Figure 3.21 Schematic of FE model shown in 2D for clarity, although the model used is 3D. Only a small section of the limbs is modelled with one fixed and a moment applied to the other to simulate the effect of the roller displacement during the test.

3.4.3 Element Type and Mesh Refinement

Eight-node brick elements were used to model the ply and interface layers. It is well-known that fully integrated (2x2x2 integration points) such elements tend to be overly stiff in bending as a result of shear locking, especially for slender beams or thin plates [42-44]. This is because the edges of a fully integrated first order element cannot bend into a curved shape. Reduced integration is used as a method to overcome this phenomenon, whereby there is only a single integration point in the centre of the element. This also reduces the computational requirements, resulting in faster solve times. Figure 3.22 illustrates full and reduced integration for an eight-node brick element.

Although it has significant advantages, reduced integration can lead to an issue known as hourglassing. Hourglass modes are nonphysical, zero-energy modes of deformation that do not produce strain or stress [45,46]. Consider a single element with reduced integration subjected to pure bending (Fig. 3.23). The dashed lines are the same length after the moment is applied and the angle between them is unchanged, meaning all components of stress are zero at the single integration point. Therefore, no strain energy is generated and this is a zero-energy mode of deformation; the element cannot resist this type of deformation as it has no stiffness in this mode. This can

propagate through the mesh, particularly if it is coarse, giving spurious nonphysical results.

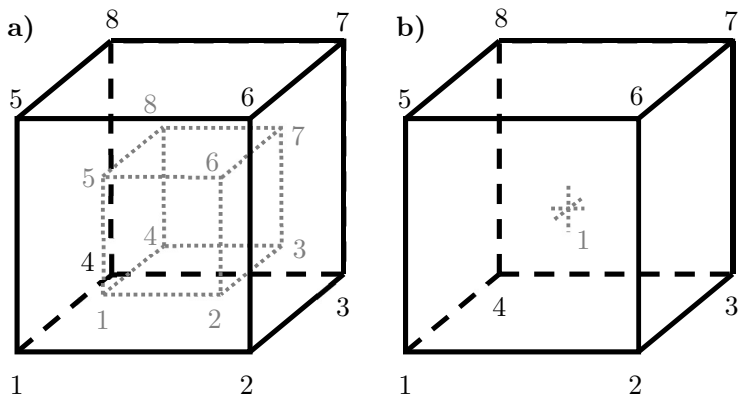

Figure 3.22 Eight-node brick element. Nodes numbered in black, integration points in grey. **a)** With full integration (2x2x2). **b)** With reduced integration (single point).

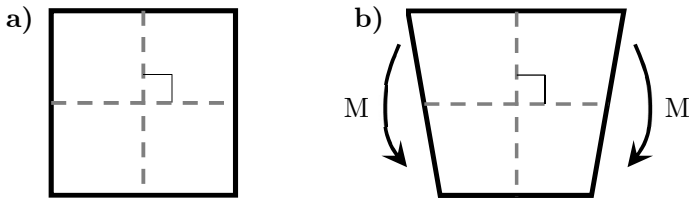

Figure 3.23 Element with single integration point in the centre. **a)** Unloaded. **b)** Under action of pure moment.

Hourglassing can be overcome through the use of hourglass controls, which have been developed and refined since the early 1980s [47,48]. Abaqus, like most modern commercial FE software, implements an automated form of hourglass control. Standard linear hexahedral elements are used throughout the curved laminate, 4-point bending model, with reduced integration and hourglass control (ABAQUS element C3D8R).

Stresses change most rapidly in the vicinity of the free edge and this is also the key area of interest for failure initiation. Therefore, the FE mesh is graded, such that there is higher fidelity near the edge than towards the mid-width, which has been shown to significantly reduce modelling errors [49]. A similar grading scheme is used by [50] to capture stresses near the free edge more accurately. Especially for reduced integration, small elements are also required to capture stress concentrations at the

boundary of a structure [45]. The fibrous layers are modelled with 6 elements through thickness, graded such that the outer elements are smaller than those in the middle of the layers. Modelling undertaken in [49] produced satisfactory results with 5 elements per layer (through thickness), also with element size near the interface reduced. The interface layers are modelled with 2 elements through thickness, which is believed sufficient since bending of the interface layers is not important to the modelling. Around the curved section there are 50 equally sized elements (no grading) and down each limb 5 equally sized elements (no grading). The grading (across the laminate width and through thickness) is achieved using the double bias option in the mesh seeding tool of Abaqus, which produces a finer mesh towards either end of the line being seeded. The number of elements along a line is set, together with the bias ratio, which determines the approximate ratio between the smallest and largest element. An example of this is illustrated in Fig. 3.24. A summary of all the mesh seeding is contained within Table 3.6. Note that mesh sensitivity is tested in sections 4.4.3 and 4.4.4, by varying the number of elements through-thickness, around the curve and across the width.

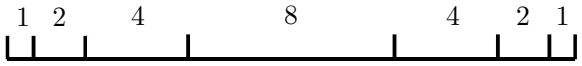

Figure 3.24 Line separated into 7 elements with double bias ratio of 8, meaning the middle element is 8 times larger than the outer most elements, with adjacent elements scaling by a factor of 2.

		No. elements	Bias ratio
Across width		60	1000
Through thickness	Fibrous layer	6	3
	Interface layer	2	-
Around curved section		50	-
Down each limb		5	-

Table 3.6 Summary of mesh seeding for FE model of curved laminate.

3.4.4 Computational Performance

In general, the finer a finite element mesh is, the more accurate the results, accepting that in the extreme case a build-up of numerical errors may mean an extremely fine mesh becomes less accurate. The limitation on mesh fidelity is generally computational performance. Therefore is it desirable to use as finer mesh as possible to produce accurate model results, whilst being able to calculate this in a reasonable timeframe.

Work has been conducted in order to optimise the Abaqus model runs. Key technical specifications of the computer used for this are shown in Table 3.7.

CPU	Processor type	Intel Xeon E5-2640
	Core speed	2.5 GHz
	No. cores/threads	6/12 (per processor)
	No. processors	2
RAM		192 GB
Operating system		Windows 7 Professional

Table 3.7 Computer specifications for Abaqus model runs.

The use of parallel computing is extremely powerful and the computer used had a total of 24 threads, although it was found not all could be used for Abaqus; some needed to be kept in reserve to run the operating system and background operations. A simple curved laminate, 4-point bending model with 15 300 elements (C3D8R) was created to observed the effect of using multiple threads on run times. The results are summarised in Table 3.8, where the processing time refers to the time taken to solve the global stiffness matrix. In general it is found that processing time is inversely proportional to the number of threads used, as expected. Assume

$$processing\ time \propto \frac{1}{p^x} \quad , \tag{3.43}$$

where p is the number of processors used. From Table 3.8, using the SSD single processor runs as baselines, x ranges between 0.66 for the smallest model using 4 processors, to 0.93 for the largest model using 2 processors. The value of x will tend to 1 for very large models, however there are diminishing returns as the number of processors increases or as the model size becomes smaller. This is likely due to the overhead associated with parallel computing and bottlenecks in certain processes which cannot be divided across multiple threads. The number of processors does not show any significant correlation with pre-processing time in Table 3.8, suggesting this stage cannot be performed in parallel.

During the pre-processing stage, Abaqus reads user inputs, such as geometry and material properties, and builds an input file for the analysis. This input file is stored in the working directory, typically a folder on the hard disk drive (HDD) or solid state drive (SSD). The speed at which the input file can be built is therefore partly limited by the speed at which the computer can access the storage. Since RAM can be accessed

orders of magnitude faster than an HDD/SSD, a RAM disk was created on a 10 GB portion of the 192 GB available and used as the working directory. The results can be seen in Table 3.8. The use of a RAM disk yielded a small reduction in processing time but reduced pre-processing time by orders of magnitude.

Table 3.8 also gives an indication of how the computation time is affected by the model size, measured in terms of degrees of freedom (DoF). Assume

$$\begin{aligned} preprocessing\ time &\propto dof^{y} \\ processing\ time &\propto dof^{z} \end{aligned}, \tag{3.44}$$

where dof is the number of DoF in the model. Using the data in Table 3.8, y is 0.95 on average and z is 2.05 on average, suggesting pre-processing time is approximately linearly proportional to model size, while processing time approximately increases with the square of model size. The processing time therefore becomes dominant for large models, such that the overall improvement achieved by a RAM disk is less significant. The fact processing time appears to increase with roughly dof^2 is interesting. Generally the number of rows and columns in the global stiffness matrix each increase proportionately with DoF, such that total number of matrix entries increases with the square of DoF. However, sparse matrices can be used, whereby only the non-zero entries are stored, together with their row and column location in the global stiffness matrix. The size of sparse matrices tend to grow with dof^1 and Abaqus uses sparse matrices (section 10.3.1 in [51] and [52]). More efficient iterative finite element solvers are being developed, which should achieve processing time scaling with approximately dof^1 [53], however such finite element formulations are beyond the scope of this thesis.

Directory location	No. CPU threads	Model size (DoF)	Computation time (sec)		
			Pre-proc.	Processing	Total
RAM disk	1	213 000	2	52	54
		427 000	4	201	205
		628 000	5	514	519
SSD	1	213 000*	64	55	119
		427 000*	123	214	337
		628 000*	177	548	725
	2	213 000	65	32	97
		427 000	123	122	245
		628 000	178	287	465
	4	213 000	64	22	86
		427 000	123	76	199
		628 000	181	169	350

Table 3.8 Effect of directory location, number of CPU threads used and model size (degrees of freedom, DoF) on pre-processing and processing times. *baseline runs for Eq. (3.43).

3.4.5 Initial Finite Element Results

Near the mid-width of the curved laminates stresses generally appear to plateaux, as seen in Fig. 3.25b. In this region there is good agreement between the predictions of the layer-wise analytical model, described in Section 3.3, and the finite element analysis. Close to the edges, however, this assumption does not hold and the stresses become highly complex, under the influence of a numerical singularity at the free edges. For example, there is an initial reduction followed by a sharp rise in direct through thickness stress near the edge, as illustrated in Fig. 3.25. This behaviour is caused physically by the discontinuity at the free edge and the differential strain of 0°, 90° and ±45° layers. Stresses normal to the free edge must reduce to zero at the free edge. Sharp changes near the free edge are also observed in through thickness shear stresses, τ_{lr} and $\tau_{\theta r}$, within the interface layers. This is studied in more detail in Chapter 4. From Fig. 3.25, it is clear that analysing stresses at the mid-width, or by using plane strain assumptions, would grossly over predict the performance of curved laminate specimens. This explains the error associated with using Eq. (3.6) to predict CBS and the results in Table 3.4. Instead, stresses must be assessed close to the free edge, where failure is likely to initiate.

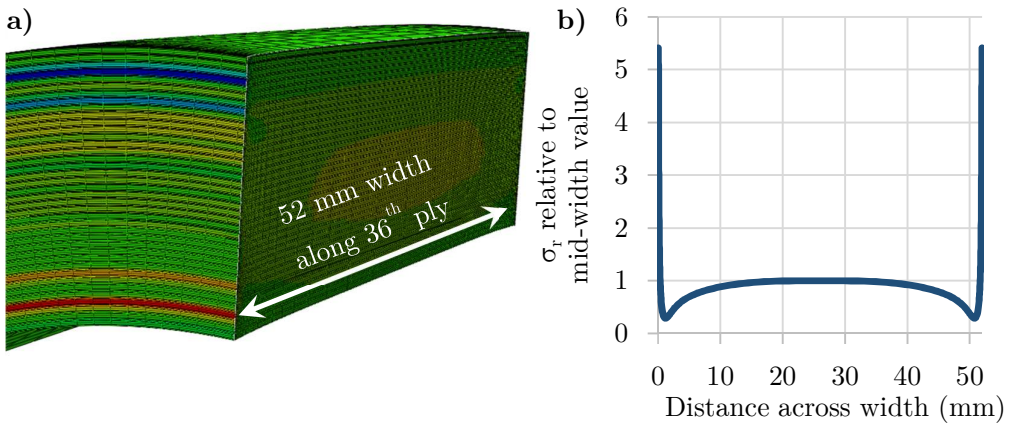

Figure 3.25 **a)** Curved laminate sectioned at the apex of the corner. Maximum tensile σ_r stress occurs at the edge of the 36th ply (4th from inner radius), which is a 0° ply. **b)** Plot of σ_r across the width of the 36th ply, with values normalised relative to the mid-width value.

Reliability of Model

The presence of a free edge creates a singularity in the Finite Element model, which significantly affects stress results obtained for the elements closest to the edge. Generally the first 2 elements adjacent to the free edge give unreliable results. Thereafter the effect of the free edge singularity rapidly dissipates, as evident in Fig. 3.25b. The influence of the singularity was investigated to determine when the predicted stress field can be considered reliable. Stresses were analysed at fixed physical distances of 60 μm and 500 μm away from the free edge. With different mesh refinements these physical distances could be represented by any number of finite elements (see for example Fig. 3.26). It was found that models that included 4 or more elements within the set distance showed negligible difference in their results, with less than 1% change in stress prediction, and were therefore assumed to have converged. Models with 3 elements within the distance gave a marginally different result (between 1-5%) and those with just 1 or 2 elements produced significantly different results (>5%). It was therefore determined that stress results at distances from the free edge similar to those considered (60-500 μm) were only reliable if 4 or more elements exist between the free edge and the point of measurement. Moreover, stresses would never converge at the free edge regardless of mesh refinement, as a result of the singularity. This poses a problem for curved laminate analysis since high stresses near the edge are likely to cause failure, yet it is difficult to reliably predict them. This problem is overcome by modelling curved laminates with a resin edge treatment, which is described in Chapter 4.

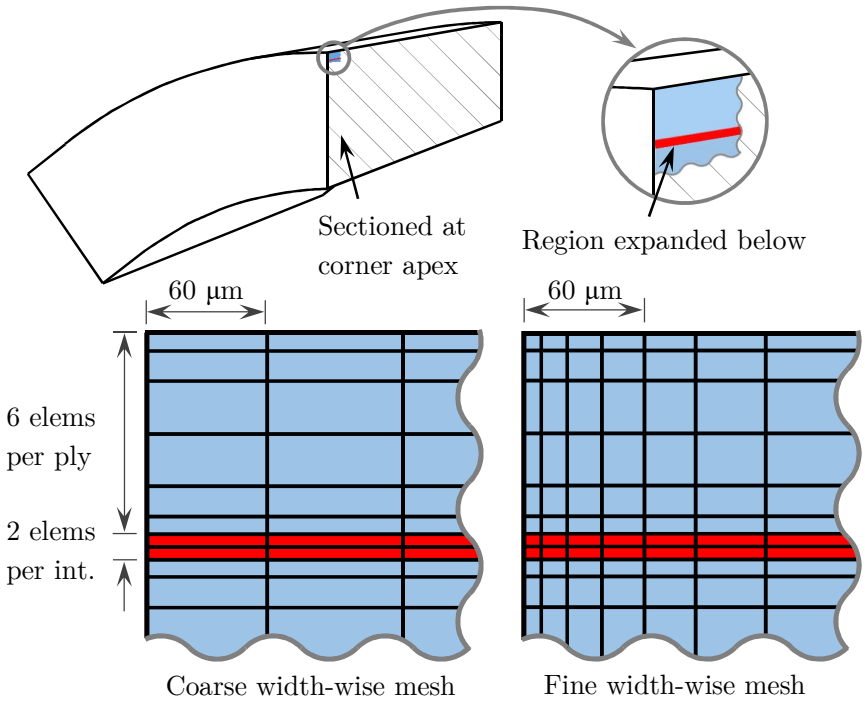

Figure 3.26 Illustration of a section of the FE model showing different mesh refinements.

3.4.6 Failure Criterion

Although the stress predictions are not reliable enough for quantitative prediction of curved laminate CBS, it is possible to qualitatively observe the relative variation in stress through the laminate thickness. A suitable failure criterion is required to provide an indication of where failure is likely to initiate.

Predicting failure in fibre reinforced composites is challenging and has been the subject of numerous research articles and review papers for decades [54-64]. A special issue of *Composites Science and Technology* [65] is entirely dedicated to failure theories. There are many different failure criteria proposed, often applicable only to particular loading conditions, indicating the complexity of failure prediction. In particular there is generally a low level of confidence in prediction of delamination [66], which is the primary failure mode observed in 4-point bending tests (see Section 3.2.3). Surveys conducted by [67] show that a broad range of failure criteria are used within industry and there is no universally accepted approach for all loading conditions.

Stress-based and fracture-mechanics-based failure criteria offer different merits and limitations. Commonly stress-based failure criteria are employed for delamination initiation and fracture-mechanics for propagation, since the singularity at the crack tip

makes stress-based methods inadequate. It has been found that maximum stress criteria are inaccurate when the interaction between stress components is important [57]. Therefore, a mixed mode failure criterion is more suitable than a maximum stress criterion, since the stresses near the free edge of curved laminates subject to 4-point bending are complex, including interlaminar shear and normal stress. Unfolding and delamination failure criteria are mainly based upon these stresses [68].

The strength of the curved laminates is assessed using a quadratic damage onset criterion, defined by Camanho et al [69] as

$$\sqrt{\left(\frac{\sigma_{33}^{+}}{f_{33}^{t}}\right)^{2}+\left(\frac{\tau_{13}}{f_{13}}\right)^{2}+\left(\frac{\tau_{23}}{f_{23}}\right)^{2}}=1 \quad , \tag{3.45}$$

with negative values of σ_{33} treated as zero. Using the FE model, Fig. 3.27 shows the result of the LHS of Eq. (3.45), evaluated 4 elements (60 μm) away from the free edge on the apex of the corner, through the thickness (as per the fine mesh in Fig. 3.26). Failure is predicted to first occur near the inner radius within ply 36, where delamination was also observed during the test, along with other delaminations (see Fig. 3.1). The stress field at the peak in Fig. 3.27 is dominated by direct inter-laminar stress (σ_{33}). Note that failure, and hence CBS, cannot be predicted from Fig. 3.27 since the distance away from the edge (60 μm), at which stresses are assessed, is arbitrary. This distance is merely a consequence of evaluating stresses 4 elements away from the edge in accordance with reliability as discussed previously.

Note that failure criteria, such as the Camanho criterion in Eq. (3.45), are based on local stresses. Therefore, a rotation matrix is used to rotate the global stress vector into the local (fibre) co-ordinate system according to

$$\begin{bmatrix}\sigma_{11}\\ \sigma_{22}\\ \sigma_{33}\\ \tau_{23}\\ \tau_{13}\\ \tau_{12}\end{bmatrix}=\begin{bmatrix}\cos^2\phi & \sin^2\phi & 0 & 0 & 0 & 2\cos\phi\sin\phi\\ \sin^2\phi & \cos^2\phi & 0 & 0 & 0 & -2\cos\phi\sin\phi\\ 0 & 0 & 1 & 0 & 0 & 0\\ 0 & 0 & 0 & \cos\phi & \sin\phi & 0\\ 0 & 0 & 0 & -\sin\phi & \cos\phi & 0\\ -\cos\phi\sin\phi & \cos\phi\sin\phi & 0 & 0 & 0 & \cos^2\phi-\sin^2\phi\end{bmatrix}\begin{bmatrix}\sigma_{l}\\ \sigma_{\theta}\\ \sigma_{r}\\ \tau_{\theta r}\\ \tau_{lr}\\ \tau_{l\theta}\end{bmatrix} \tag{3.46}$$

taken from [70], where 11 is the local fibre direction, r, θ and l are the global cylindrical axes of a curved laminate and ϕ is the fibre orientation of the local co-ordinate system.

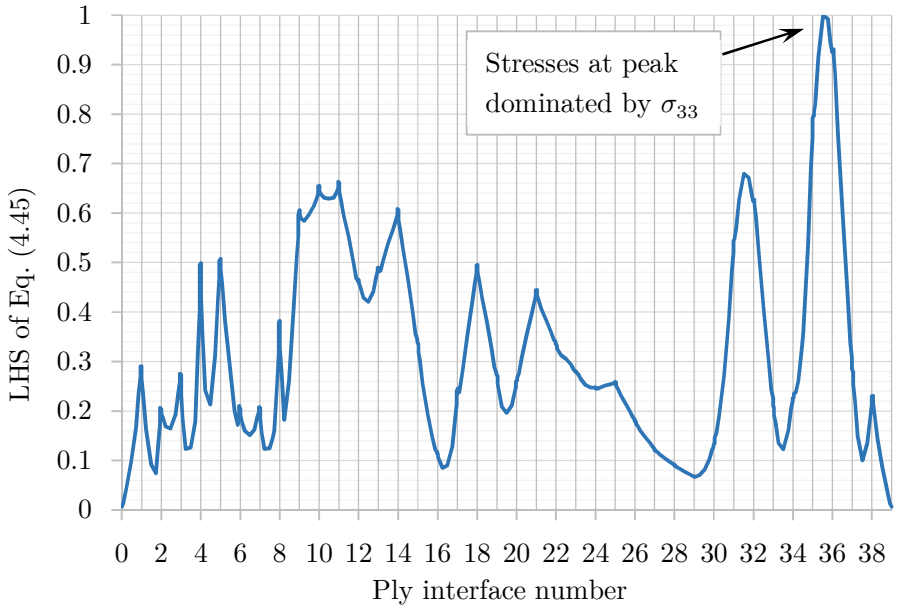

Figure 3.27 LHS of Eq. (3.45) evaluated at the corner apex, 4 elements (60 μm) away (width-wise) from the free edge of the curved laminate model of specimen G39B.

3.5 Closing Remarks

Curved laminate specimens are tested under the action of corner unfolding via a 4-point bend test. CBS and failure location is presented for various specimen types. The novel (N-) specimens fail at a lower average CBS than the symmetric (S-) specimens with an equal number of plies. Most notably, the failure of N44 specimens is very consistently concentrated in the region close to the inner radius where there are two pairs of 0° plies in the stacking sequence. This is highly significant because standard stacking sequence guidelines state that no more than 3 plies of the same fibre orientation should be positioned adjacent to one another to minimise interlaminar stresses; however, the N44 stacking sequences positions only 2 plies of the same orientation together and produces a significantly lower average CBS (11.4%) compared with the S44 stacking sequence. This fundamentally challenges the guideline and suggests that under certain loading conditions no two plies of the same orientation should be positioned adjacent to one another.

The certification process is reviewed. As per witness specimens commonly used for certification, the curved laminate specimens tested in this chapter have exposed free edges. These are found to initiate failure and significantly reduce the strength as

compared with 2D analysis (plane strain), in which free edges are effectively not present. The specimens therefore under-represent the strength of the full-size part, which is much wider and commonly built into surrounding structure at its ends, such that there is no free edge. The edge effect results in analytical modelling being unsuitable and causes a numerical singularity, which makes quantitative evaluation of laminate strength using linear FEA challenging. To overcome this and improve specimen strength, the edge effect must be mitigated, which can be achieved using an edge treatment, developed in Chapter 4.

4 EDGE EFFECT AND TREATMENT

The initiation of failure of curved laminate specimens from the free edge is investigated using CT imagery of a partially delaminated test specimen, and an explanation for this edge effect is presented. Techniques proposed in the literature for the mitigation of the edge effect are reviewed, which have been applied primarily to flat laminates. An original free edge protection treatment is developed, which is better suited to retrospective application to witness specimens once they have been cut from a production part. This novel resin edge treatment is applied to a range of specimen types and experimentally tested, comparing results with untreated specimens from Chapter 3. The FE model and failure prediction is improved, using two failure criteria: Camanho criterion identified in Chapter 3, and Christensen failure criterion. Finally, the level of defects within the experimental specimens is presented.

4.1 Analysis of Partial-Width Delamination

The majority of curved laminate test specimens exhibited full-width delaminations when analysed after failure by 4-point bending. During the tests, the delamination(s) appeared instantaneously and it was not possible to determine where they originated. However, two specimens only exhibited partial-width delaminations: N24-11 and N24-12. N24-11 failed at a below-average CBS. Therefore, the lower energy at failure likely resulted in the delamination not propagating across the full width of the specimen. N24-12 failed at above-average CBS, however.

The partial-width delaminations were examined using X-ray computed tomography (CT). In both cases, the delamination(s) extended from the free edge towards the mid-width and were never contained within the laminate without extending to the free edge. This suggests the failure likely originated at the free edge in both cases. Figure 4.1 shows the main and small delamination in 3D for specimen N24-12. The curved laminate is shown as semi-transparent to provide a reference for the location and size of the delamination. Figure 4.2 shows the main delamination as viewed from

above. The CT visualisation software Avizo [71] was used to produce all CT images and measure the size of the delamination, as labelled in Fig. 4.2. At its widest point the delamination extends approximately 10.7 mm into the 25 mm wide specimen. Figure 4.3 shows the delamination against a partially cut-away view of the laminate, with relevant interfaces highlighted and labelled for clarity. The crack appears to initiate within interface 3 at the edge, subsequently jumping into interface 2 and 1 further towards the mid-width. The partial-width delaminations provide further evidence that failure of the curved laminate test specimens initiates from the free edge.

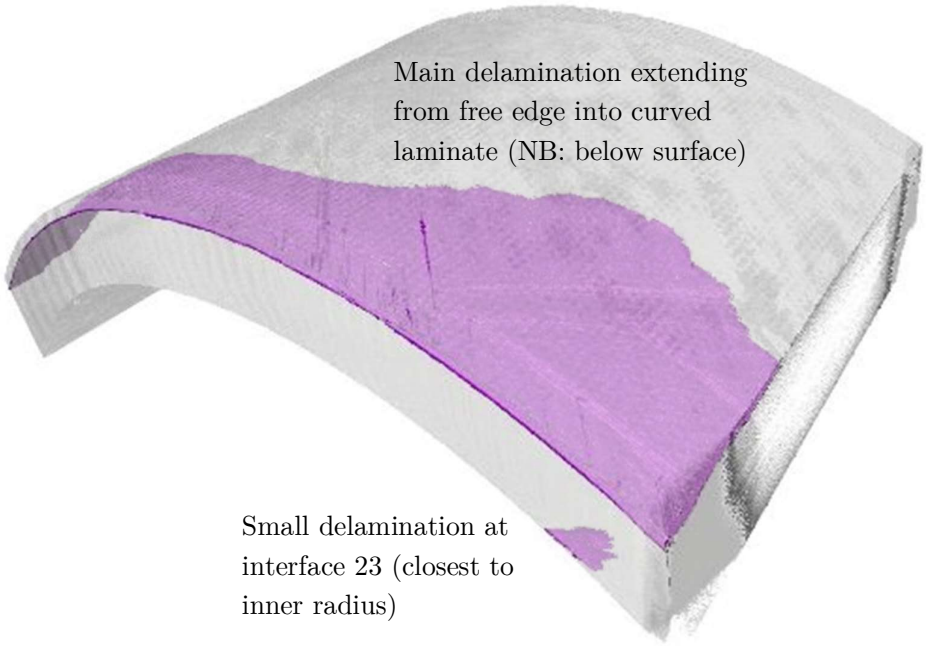

Figure 4.1 CT image of N24-12 post-test, showing main delamination (purple) in context of curved laminate (shown as translucent ghost). A small delamination near the inner radius is also visible.

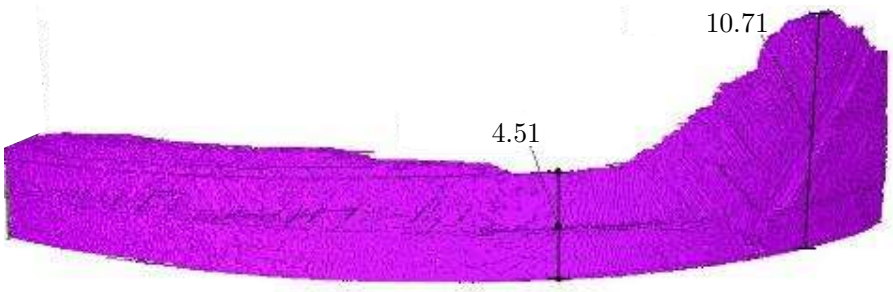

Figure 4.2 CT image showing main delamination shape as viewed from above the apex of the curved laminate (laminate hidden for clarity). The size of the delamination (mm) is shown in two locations.

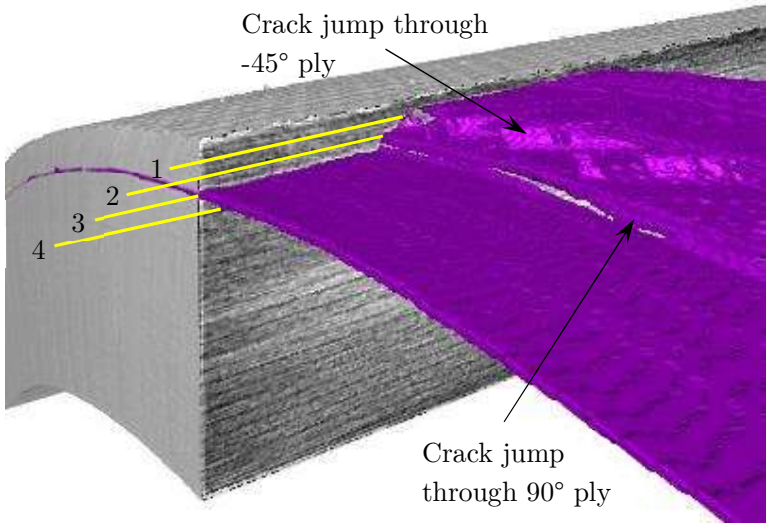

Figure 4.3 CT image of delamination (purple) showing through thickness location against cut away of curved laminate (grey scale). The first four interfaces (near outer radius) are highlighted in yellow for clarity.

4.2 The Edge Effect

The mismatch in elastic properties between plies with different fibre orientations induces high interlaminar stresses at the free edge of the UD curved laminates under bending. This phenomena is therefore generally not observed in isotropic materials, such as Aluminium, or if a CFRP laminate consists of a single ply orientation. This so called edge effect generally causes narrow test specimens to fail at a significantly lower load than would be predicted by 2D, plane strain analysis. It therefore results in the narrow specimen not being representative of the final, full-length product, where the final product is very long and/or is built into surrounding structure at its ends, such that it has no free edges.

The high stress intensity caused by free edges has long been a known issue. Evaluating the edge effect is challenging and many analytical and numerical approximation methods have been proposed. Literature surveys of these can be found in review articles [72,73] but there are no analytical methods that calculate the exact stresses at the free edge. An approximate analytical method for calculating the interlaminar stresses for laminated plates is presented in [74]. This work shows the singular behaviour of interlaminar normal and shear stresses near laminate free edges, which gives rise to the challenges and complexity in modelling such problems. Linear

FE analysis often results in highly localised, mesh dependent stresses near the edge that are higher than the strength of the material. A method for assessing when these high stresses will lead to failure has been developed using linear elastic fracture mechanics [75]. Non-linear FE analysis of cohesive zones is often performed in order to capture failure initiation and predict composite laminate strength, such as 3D non-linear modelling of delamination damage onset and growth in composite spar wingskin joints [76]. 3D non-linear FE modelling is generally very computationally expensive. An alternative method for assessing the free edge effect for composite flat plates is described in [77]. This consists of assessing 2D and 1D problems through a series of iterations, which produces quasi-3D results less costly than full 3D FEM computations.

4.2.1 Analysis of Edge Effect using FE

The FE model of the G39B specimens is analysed. Near the inner radius the curved laminates are under tension in the θ direction (refer to Fig. 3.2, page 68) as a result of the unfolding moment. Figure 4.4 shows the variation in different stress components from the mid-width to the free edge of the curved laminate. As expected, components of stress in the l-direction (normal to the free edge) must become zero at the free edge, in this case τ_{lr} and σ_l. In contrast, away from the mid-width σ_r initially reduces before rapidly increasing close to the free edge. Figure 4.5 shows the variation in stress components $\tau_{l\theta}$, which must reduce to zero at the free edge, and $\tau_{\theta r}$, which rapidly increases near the free edge. Previous studies have also found that interlaminar shear stresses (τ_{lr} and $\tau_{\theta r}$) peak at or near the free edge [78,50] and it has been found that edge delamination is dominated by $\tau_{\theta r}$, though may be triggered by normal stress σ_r [41].

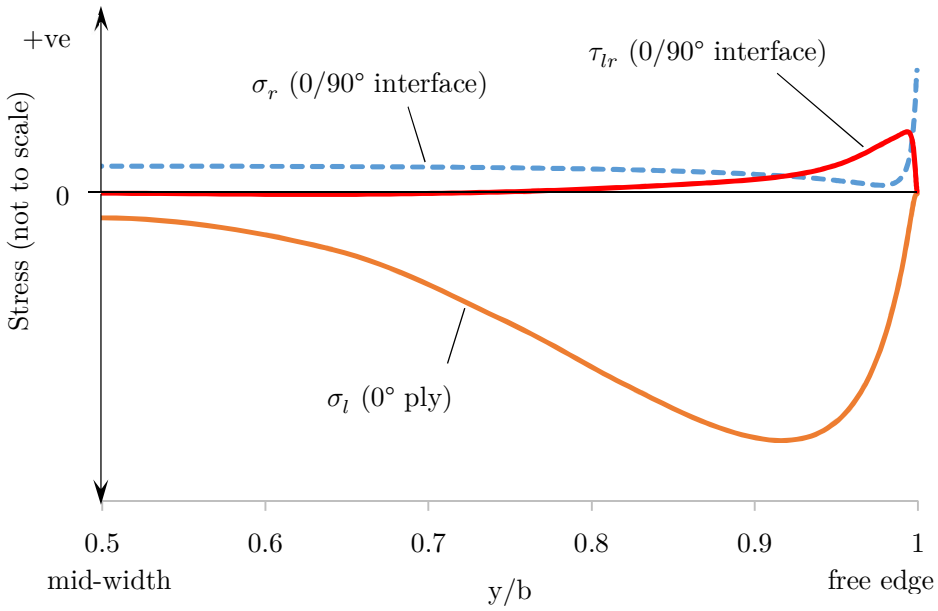

Figure 4.4 Variation in stress components from mid-width to free edge in vicinity of 0/90° pair of plies closest to inner radius of G39B FE model.

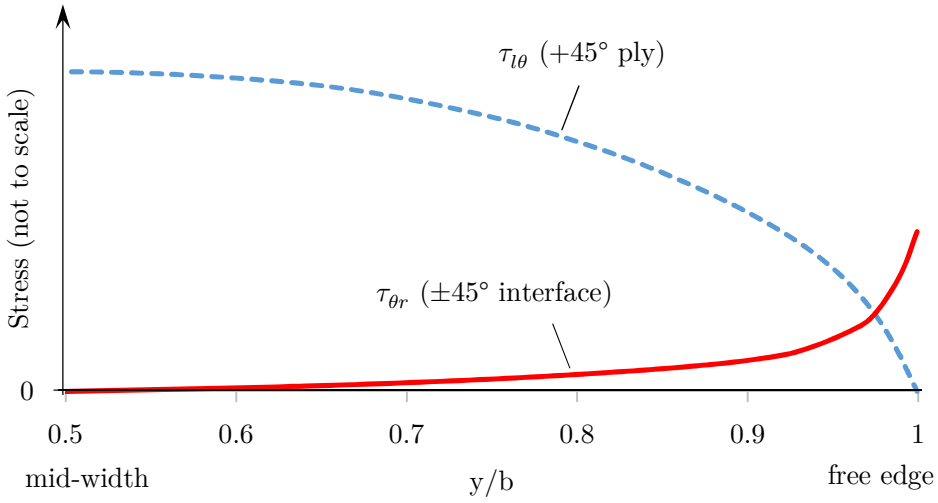

Figure 4.5 Variation in stress components from mid-width to free edge in vicinity of ±45° pair of plies at inner radius of G39B FE model.

4.2.2 An Explanation of the Edge Effect

A similar stress variation to that shown in Figs. 4.4 and 4.5 is presented in [79] for flat plates under uniaxial tension. A full explanation for this is also given in [79] and can be adapted to the curved laminate results. Consider the response of the ±45° plies under tension in the y-direction, a small section of which is shown in Fig. 4.6 as an exploded view. The angle of the fibres generates in-plane shear (shown in black) in the opposite sense for each ply. However, this must be zero at the free edges. To achieve equilibrium, interlaminar shear (shown in red) is formed on the bottom surface of the -45° ply and the top surface of the +45° ply in the vicinity of the free edge. This is driven by the mismatch in extension-shear elastic coupling ($\bar{Q}_{16}$ and $\bar{Q}_{26}$) of the ±45° plies and explains the result shown in Fig. 4.5, where the y-direction is analogous to the θ-direction, x to l and z to r.

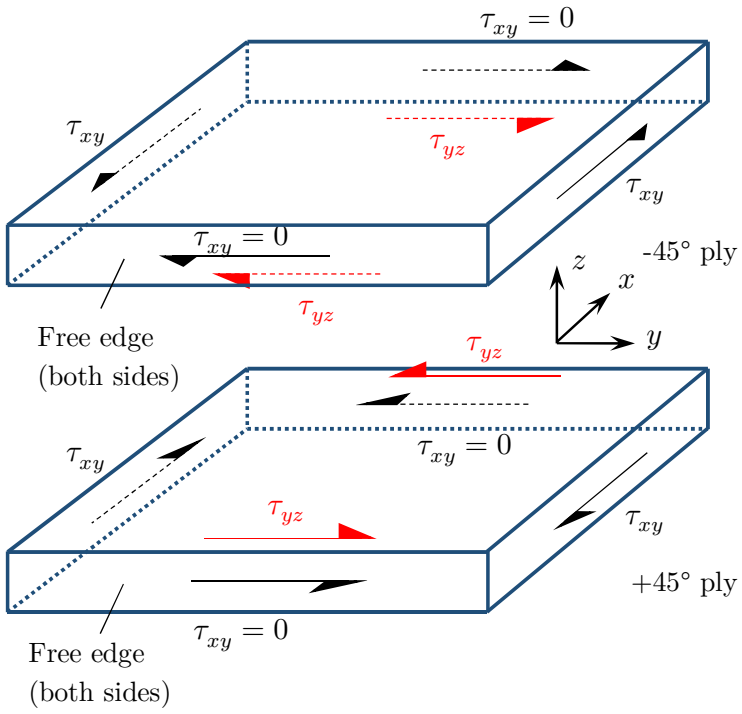

Figure 4.6 Response of ±45° plies to tension in y-direction (exploded view of small section). The angle of the fibres generates in-plane shearing, τ_{xy}. However, since τ_{xy} must be zero at the free edge, equilibrium is achieved by generating interlaminar shear stress, τ_{yz}, near the free edge on the top surface of the +45° ply and bottom surface of the -45° ply. Adapted from [79].

Consider the response of the 0/90° ply pair under tension in the y-direction, a small section of which is shown in Fig. 4.7 as an exploded view. The 90° contraction in the x-direction will be restricted by the 0° ply, putting the plies into tension and

compression respectively. The stress, σ_x, must tend towards zero at the free edges since there is no stress applied at these boundaries. Instead, to counteract the contraction or stretching of the ply, interlaminar shear (τ_{xz} shown in red) is developed near the free edge, though this must also become zero immediately at the free edge. Now consider the stresses in the vicinity of the 90° ply free edge, shown in 2D as viewed in the y-direction in Fig. 4.8. The non-zero σ_x stress towards the mid-width (LHS) generates a clockwise moment about the upper surface, which is not counteracted by the free edge stress (RHS) since this is zero. Instead a system of interlaminar direct stress, σ_z, generates a restoring anti-clockwise moment near the free edge as shown in Fig. 4.8. The unfolding moment during the 4-point bending test generates a positive tearing stress, as seen by the positive value of σ_r at the mid-width in Fig. 4.4. The free edge interlaminar direct stress system initially reduces this away from the mid-width, before increasing rapidly very close to the free edge as the positive σ_z stress in Fig. 4.8 (analogous to σ_r in Fig. 4.4) is superimposed with the tearing stress caused by corner unfolding. The presence of interlaminar shear stress τ_{xz} (τ_{lr}) and sharp increase in interlaminar direct stress σ_z (σ_r) is due to the mismatch in Poisson's ratio between adjacent plies.

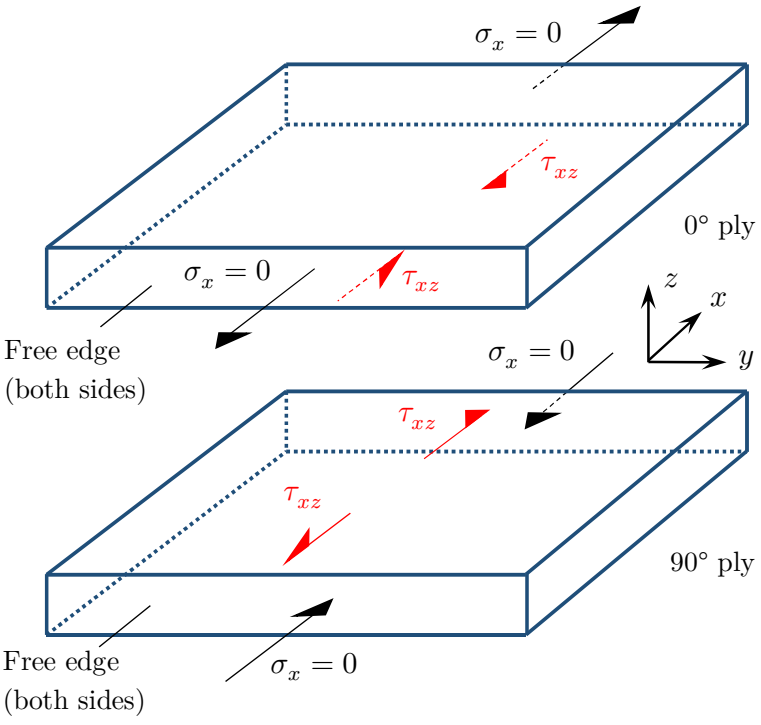

Figure 4.7 Response of 0/90° plies to tension in y-direction (exploded view of small section). The mismatch in Poisson's ratio results in x-direction contraction of the 90° ply being restricted by the 0° ply via interlaminar shear, τ_{xz}. Adapted from [79].

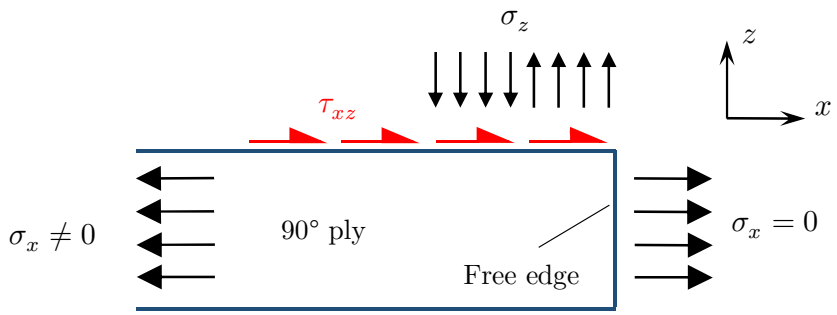

Figure 4.8 2D view of 90° ply free edge. Direct, σ_z, stress near the free edge is generated in order to provide a resorting (anti-clockwise) moment to counteract the clockwise moment of σ_x and τ_{xz} stress. Adapted from [79].

4.3 Treatment of Free Edges

To mitigate the edge effect, a treatment is sought that protects the free edges and delays failure initiation, such that specimens behave similarly to (and are therefore more representative of) the production part, where free edges do not exist. There have been many techniques proposed to reduce the high stress intensity associated with free edges.

Caps can be bonded onto the free edges and this has been shown to reduce interlaminar normal stress but does not significantly reduce interlaminar shear stress [80-83]. The edges can be altered to tailor structural properties, using an isotropic filler material and by changing the orientation of a ply near the free edge to reduce interlaminar stresses in this region [84]. A number of other techniques have been used to mitigate the free edge effect, such as stitching along the edges [85] and the use of adhesive layers [86]. It has also been shown that the stacking sequence of the laminate is important and can be tailored to influence the interlaminar stresses near a free edge [87].

The vast majority of edge protection techniques have been applied only to flat laminates under axial loading. The curvature of the specimens in this thesis would make the use of edge caps difficult since these would have to be somehow curved. The modification of the specimens in terms of stitching, stacking sequence, or other forms of tailoring the stiffness properties at the edge, is not possible post-cure, and is therefore not suitable for retrospective application to witness specimens once they have been cut from a production component. A treatment that addresses these issues is therefore required a novel method is introduced in Section 4.4.

4.4 Resin Edge Treatment

This treatment consists of a coating of resin applied to the exposed free edges of specimens, as illustrated in Fig. 4.9. Referring to the mechanism driving the edge effect (discussed in Section 4.2.1 with Figs. 4.6 and 4.7), the addition of resin removes the condition that stresses in the l-direction must become zero at the specimen edge, which is no longer a free edge and hereafter referred to as the CFRP edge. The mechanism for the edge effect is therefore partially mitigated, although there is still a discontinuity across the CFRP edge-resin treatment boundary.

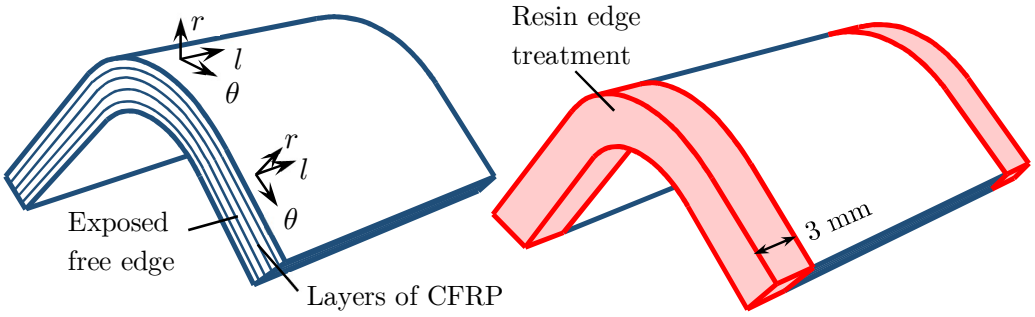

Figure 4.9 Curved laminate without (LHS) and with (RHS) resin edge treatment, applied to the exposed free edges.

It has been shown that reducing the fibre volume fraction towards the free edge reduces interlaminar stresses for a flat laminate under axial extension [88]. The resin edge treatment technique has some similarities to this, with effectively a fibre volume fraction of zero within the resin edge treatment. However, whereas the specimens in [88] must be specifically designed for the test, a key benefit of the new resin edge treatment is that it can be applied retrospectively to witness specimens (or "trim" sections) cut from the edge of large production components. This makes it more suitable for meeting certification requirements discussed in Section 3.1.

As with untreated curved laminate specimens, the free edges are first polished. They are then plasma treated, in order to ensure the highest quality bond possible, and then the resin (EP1330LV, supplied by Resinlab [89]) is applied. A mould is used to control the shape of the resin edge, such that it is prismatic with the curved laminate (see Fig. 4.9). Resin is poured into the mould by hand and cured in an oven before

being ground back so that approximately 3 mm of resin is left on each free edge. This increases the overall specimen width to approximately 58 mm (G39A/B specimens) or 31 mm (S24/44 and N24/44 specimens). However, for the purposes of calculating CBS according to Eq. (3.1), the width is taken as that of the CFRP only.

The 3 mm resin edge is chosen from analysis of the stress transfer between a fibrous ply and resin by interlaminar shear. This is similar to deriving a critical fibre length, except instead of a single fibre, an entire ply thickness is considered. The required resin width is given by w_r, calculated according to

$$w_r = \frac{t_{fib}\ f_{11}^t}{2\ f_{13}} \quad , \tag{4.1}$$

where t_{fib} is the thickness of the fibrous layer. Assuming the fibrous layer carries a stress equal to the tensile limit, f_{11}^t, is the worst case. Typically, the stress will be an order of magnitude lower than this and so a resin edge significantly smaller could be equally effective but 3 mm is conservative.

At a laminate free edge there is an infinite contrast in mechanical properties across the free edge. The resin edge treatment works by reducing this contrast. Since CFRP is generally much stiffer than pure resin, is it important that a high modulus resin is used to minimise the contrast across the CFRP-resin edge boundary. The effect of resin modulus is discussed in Section 5.1, and in Section 5.4 resin materials with different moduli are analysed and tested.

4.4.1 Experimental Results of Resin Edge Treatment

Specimen Type	Treated (kNmm/mm)		Untreated (kNmm/mm)		Treated CBS increase (%)
	CBS	S.D.	CBS	S.D.	
G39B(R)	8.65	0.04	7.49	0.22	15.6
S24(R)	2.30	0.11	2.04	0.12	12.9
S44(R)	5.23	0.45	4.28	0.20	22.3
N24(R)	2.00	0.05	1.82	0.15	9.9
N44(R)	3.92	0.04	3.79	0.45	3.3

Table 4.1 Average CBS and standard deviation for resin treated specimens. Compared against average CBS for equivalent untreated specimens, showing increase in CBS as a result of resin edge treatment (without rounding errors).

Each test was stopped immediately after first failure event occurred, identified by either an audible crack or load drop. The specimen was then inspected visually, using a microscope and X-ray CT scanner to identify the location of first failure. The results for each specimen type are summarised in Table 4.1, comparing average CBS and standard deviation against that of the equivalent untreated specimens. Results for each individual test are illustrated in Fig. 4.10 through Fig. 4.14. Full tables of results for all test specimens can be found in Appendix B. Specimens that had resin edge treatment consistently achieved a higher CBS than those without treatment, in particular for the production laminate G39B and those with stacking sequences following typical industrial standards: S24 and S44. The test variability was also generally reduced by the resin edge treatment (lower standard deviation), except in the case of the S44(R) specimens. The higher standard deviation for this specimen type was largely caused by specimen S44(R)-01, however, for which the resin edge appeared to fail prematurely. Figure 4.15 shows the resin edge immediately after first failure. Whereas the resin edge generally shattered and de-bonded from the CFRP edge at the point of failure (see Fig. 4.16), for S44(R)-01 there were cracks visible, most likely associated with the tensile tangential stresses (θ-direction in Fig. 4.9) at the inner radius.

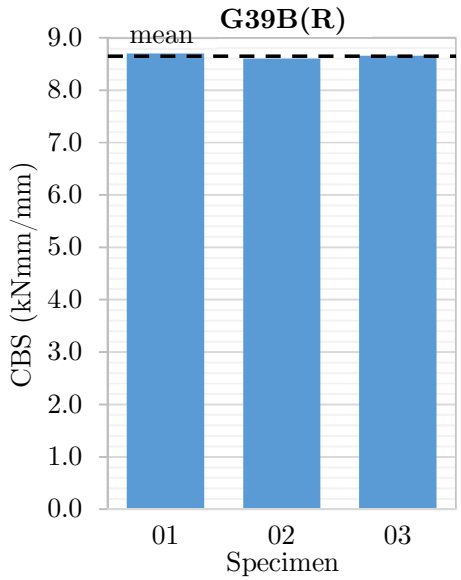

Figure 4.10 G39B(R) specimen test results.

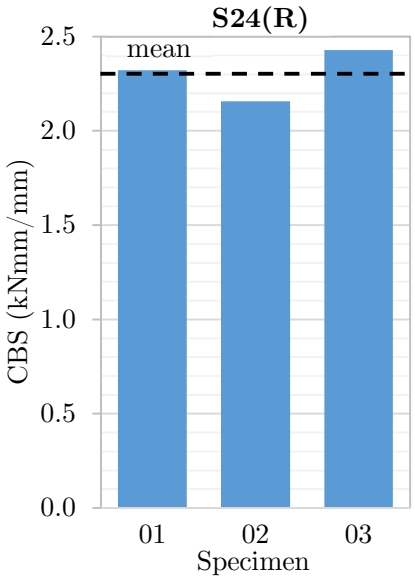

Figure 4.11 S24(R) test results.

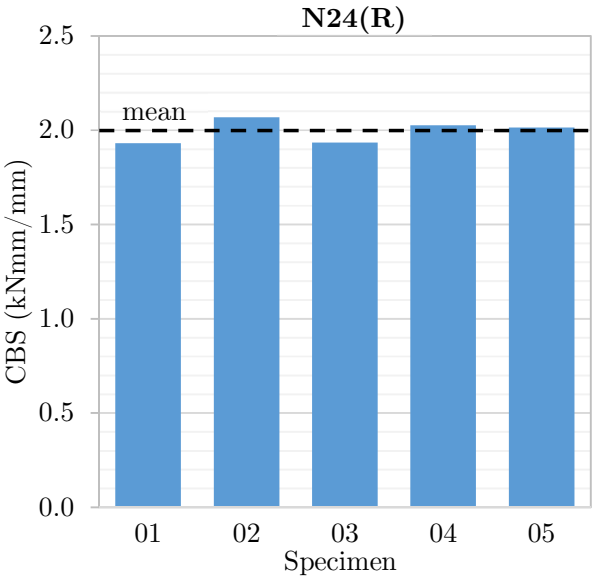

Figure 4.12 N24(R) test results.

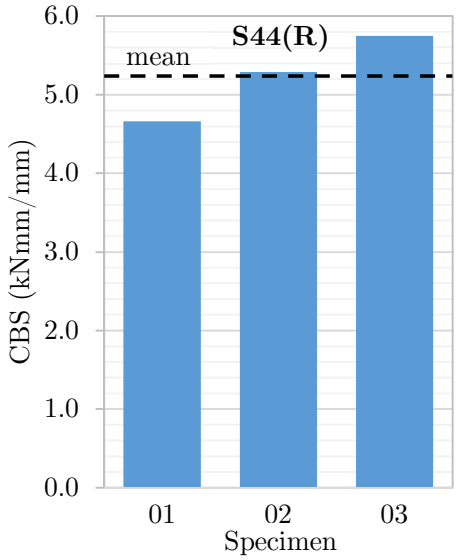

Figure 4.13 S44(R) test results.

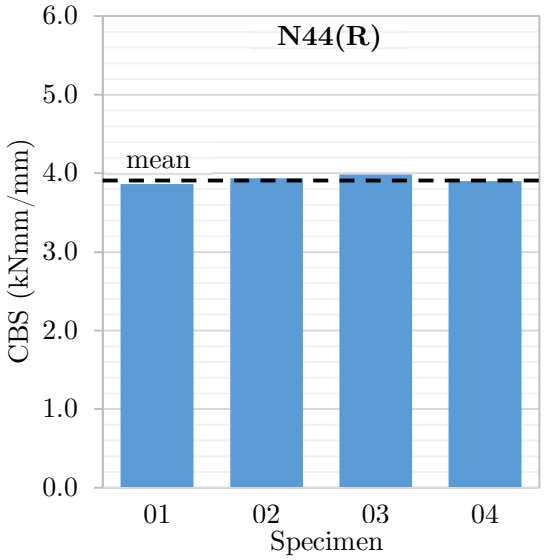

Figure 4.14 N44(R) test results.

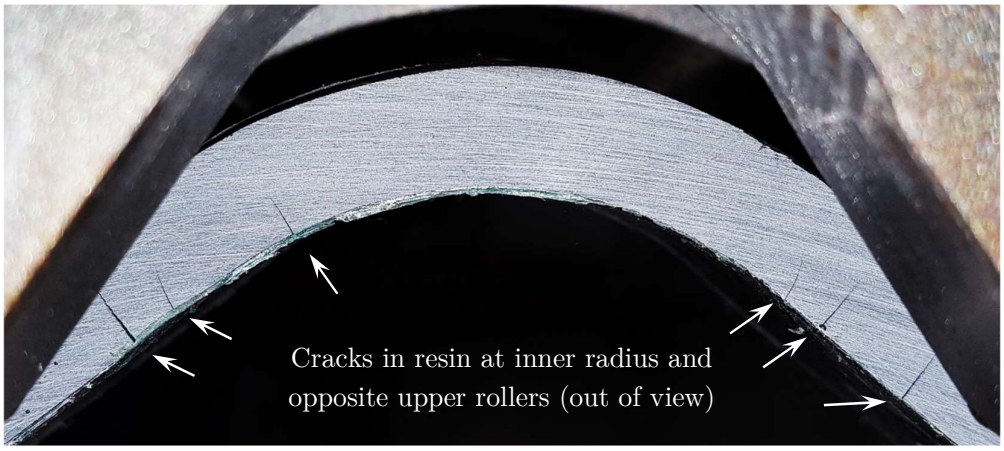

Figure 4.15 Specimen S44(R)-01 immediately after first failure. Cracks are visible in the resin edge inner radius, where the unfolding moment causes tension in the tangential direction.

The failure location of the test specimens was found to be relatively predictable, with a clear difference between specimens that were resin edge treated and those that were not. The specimens generally failed with multiple delaminations simultaneously (see Fig. 4.16a), meaning it was not possible to determine where failure first occurred from test data alone. However, whereas the untreated thicker specimens (39- and 44-ply) all failed within the inner half of the laminate only, the edge treated thicker specimens all exhibited large delaminations throughout the thickness of the laminate, as shown in Fig. 4.16a. At the point of failure during the test, the resin edge shattered, leaving the CFRP edge exposed, as shown in Fig. 4.16b. Figure 4.16 shows specimen G39B(R)-01 as an example but all 39- and 44-ply specimens exhibited similar failure behaviour, with the exception of S44(R)-01, discussed previously. The thinner 24-ply specimens exhibited greater variability in failure location. Delamination was observed within ply 3 and interfaces 2-3 only for half the specimens, as was typical for the untreated 24-ply specimens. The other half of the treated 24-ply specimens exhibited delaminations throughout the thickness, including the surface plies at the inner and outer radius.

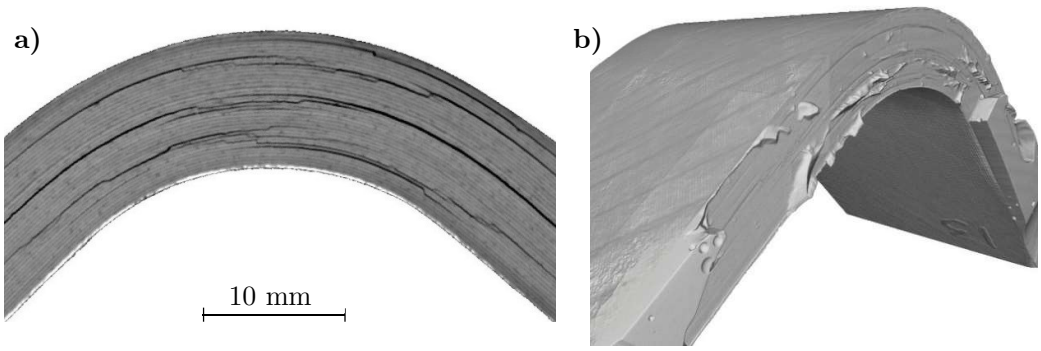

Figure 4.16 Post-failure CT scan of specimen G39B(R)-01. **a)** Cross-section within the CFRP. **b)** 3D view showing damage to resin edge, with only small fragments remaining bonded to the CFRP edge.

4.4.2 Finite Element Modelling of Resin Edge Treatment

In order to analyse the effect of the resin edge treatment the central CFRP section of the treated curved laminate is modelled with an identical mesh as for the untreated curved laminate (Section 3.4). The resin edges (applied to the CFRP free edges) are each meshed with 10 elements across the width (l-direction in Fig. 4.9). Fidelity at the CFRP edge-resin edge treatment boundary is increased using the single bias option in ABAQUS, with a bias ratio of 150. Through thickness and around the corner, the mesh seeding is identical to the central CFRP section.

Figure 4.17 shows the effect the resin edge treatment has on stresses, by calculating the failure criterion at the same location within the laminate for both untreated and treated laminates, with the same opening moment applied. The treatment generally suppresses stresses throughout the thickness, however the peaks tend to be dominated by interlaminar shear rather than interlaminar direct stress and in a few locations, particularly the inner- and outer-most interfaces, the failure criterion is increased by the resin edge treatment. The suppression of the highest untreated laminate peak likely the reason for the reason for the increased CBS observed experimentally for treated laminates. The highest peak in the treated laminate result is at interface 5, although there are several peaks of similar magnitude. This likely explains the shift in delamination locations from within the inner half of the laminate only for untreated 39-ply specimens, to throughout the thickness for treated 39-ply specimens, including close to the outer radius.

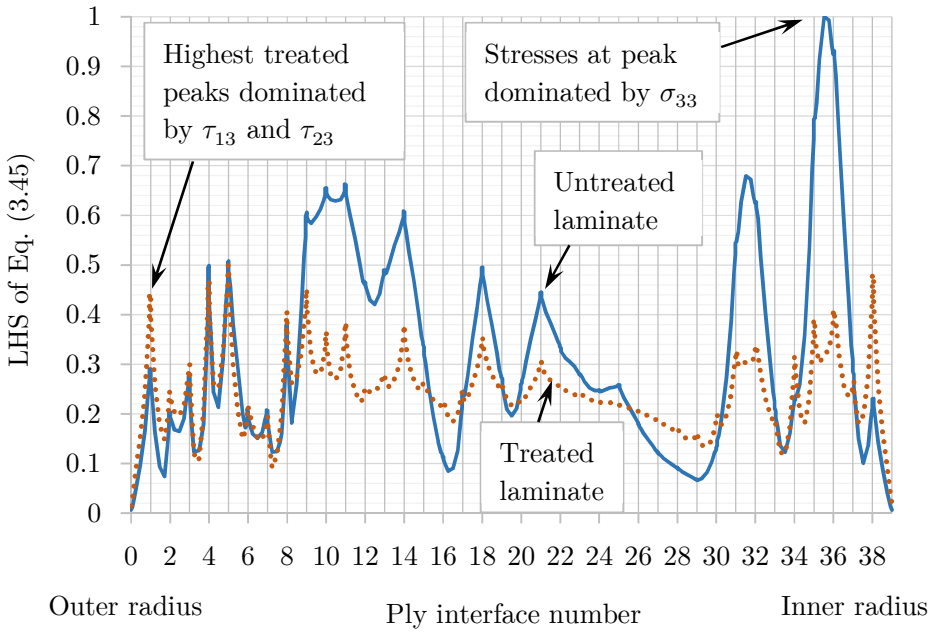

Figure 4.17 LHS of Eq. (3.45) evaluated at the corner apex, 4 elements (60 μm) away (width-wise) from the CFRP edge of the curved laminate models of G39B (untreated) and G39B(R) (resin edge treated).

4.4.3 Mesh Refinement

It is initially assumed in Section 3.4.3 that modelling the resin rich interface layers with 2 elements through thickness is sufficient since bending of these layers is not important to the modelling. However, sharp changes in stresses are observed in the through thickness direction, evident by the peaks in Fig. 4.17. It also appears that peaks in the Camanho failure criteria (where failure is predicted to occur) are often coincident with interface layers. Therefore, refinement of the mesh through thickness of interface layers is considered. FE models with 2, 4, 6 and 8 elements through the thickness of each interface layer are created, with identical meshes in all other respects. Equation (3.45) is evaluated at the mid-thickness of interfaces 4 and 38, near the CFRP edge at the corner apex for each model. Note that an arbitrary unfolding moment is applied and hence the absolute value of Eq. (3.45) is unimportant. The convergence as the mesh is refined is shown graphically in Fig. 4.18. On the basis of this study it is deemed that using 6 elements through the thickness of interface layers is sufficient for accurately assessing the Camanho failure criterion, whilst minimising model size and computation time.

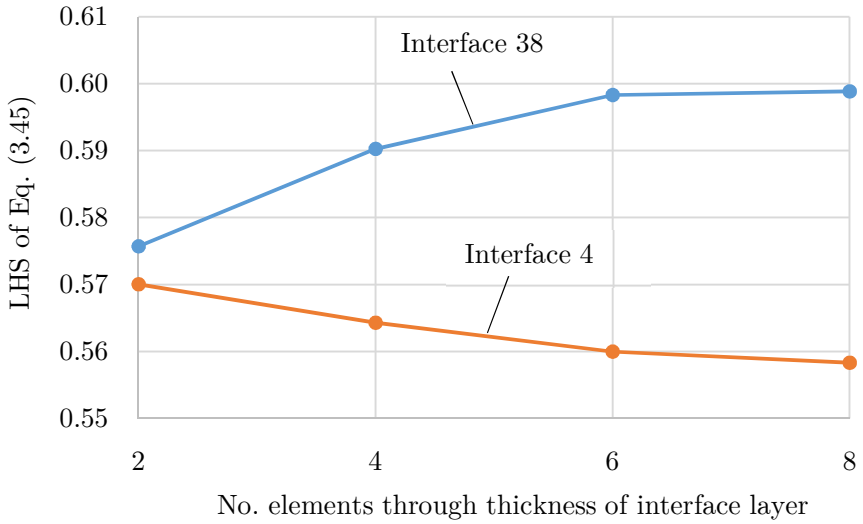

Figure 4.18 LHS of Eq. (3.45) evaluated at the corner apex, 1 element away from the CFRP edge at the mid-thickness of interfaces 4 and 38. Results appear reasonably converged with 6 or more elements through thickness.

Mesh refinement around the curve of the FE model is now considered. Previously 50 elements were used around the curved section and 5 down each limb, i.e. in the θ-direction of Fig. 4.9. Note that only shortened limbs are modelled, equal in length to the laminate thickness (see Fig. 3.21). This dimension of the mesh is varied with 20, 40, 60 and 90 elements around the curve of four separate FE models, with 2, 4, 6 and 9 elements down each limb respectively. Equation (3.45) is evaluated at the mid-thickness of interfaces 5 and 38, near the CFRP edge at the corner apex of each model. Again an arbitrary unfolding moment is applied. The mesh convergence is shown in Fig. 4.19. There is a difference of 4% between the result at interface 38 with 20 and 90 elements around the curve. With 60 elements, the result is within 0.5% of the 90 element model. It is deemed that using 60 elements around the curve and 6 down each limb is sufficient for mesh convergence and minimising computation time.

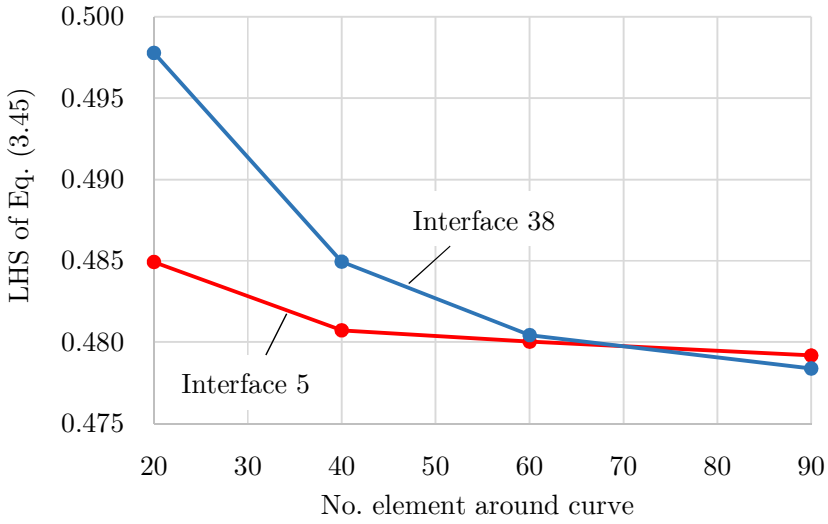

Figure 4.19 LHS of Eq. (3.45) evaluated at the corner apex, 1 element away from the CFRP edge at the mid-thickness of interfaces 5 and 38. Results appear reasonably converged with 60 or more elements around the curve.

4.4.4 Analysis of Edge Singularity

The singularity caused by the free edge makes FE modelling of untreated curved laminates extremely challenging. To illustrate the effect, the plot in Fig. 4.20 shows direct interlaminar stress. The stress is measured in the middle of the 36th ply, which is the 0° ply closest to the inner radius of the G39B specimen model and is where maximum tensile σ_{33} is seen close to the CFRP edge. Note that the CFRP edge is the free edge for untreated laminates and the boundary with the resin edge for treated laminates. By varying the width-wise mesh refinement, the size of the element at this edge is varied, and so the physical distance from the edge that stresses are taken.

From Fig. 4.20 it appears that the untreated curved laminate stress value is tending towards infinity as it is measured closer to the free edge. This is because there can be no stress normal to the free edge. Other stresses, such as direct inter-laminar stress, increase near the edge to compensate for this, as discussed in Section 4.2.2. Note that the stress close to the edge is significantly beyond the allowable for the untreated laminate with the average experimental CBS of 7.49 kNmm/mm applied. In contrast, the treated curved laminate stress value appears to converge to a finite value. This is because the presence of the resin edge allows for some stress normal to the CFRP edge, in turn preventing other stresses from becoming infinite. The result is that it is much

more feasible to model the treated laminates to predict failure than the untreated ones, without a reliable method for determining how far from the free edge to evaluate untreated laminate stresses.

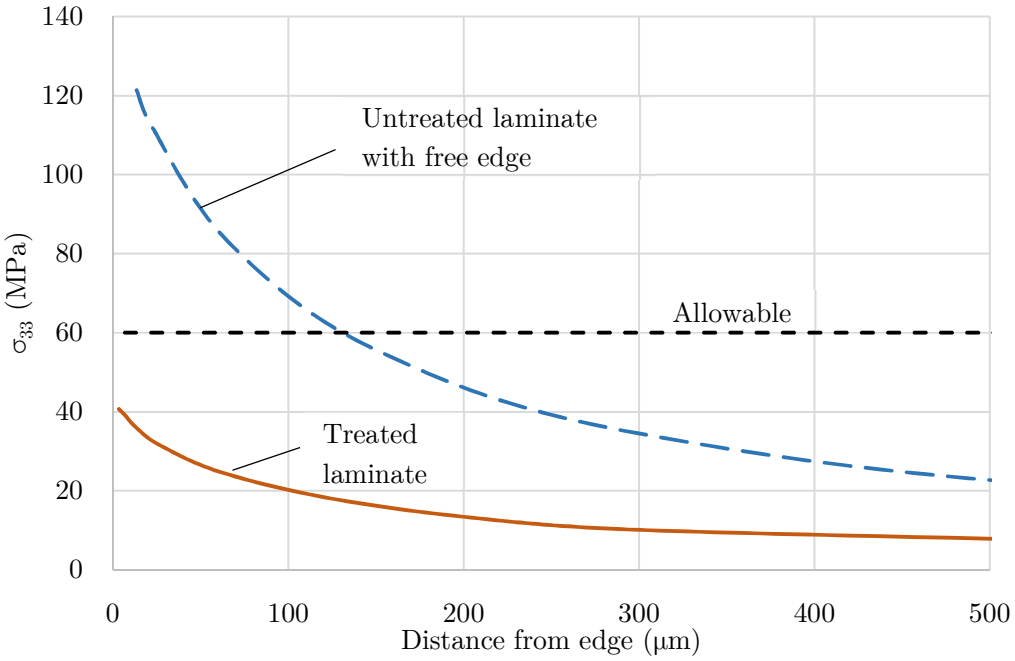

Figure 4.20 Direct interlaminar stress in ply 36 of G39B FE model near CFRP edge. Average experimental CBS of 7.49 kNmm/mm is applied.

4.4.5 FE Prediction of CBS for Resin Treated Laminates

The mechanical properties of the CFRP materials in the FE models are as previously recorded in Table 3.3 and Table 3.5. The resin edge material EP1330LV is assumed to have a modulus of 8.9 GPa [89]. Unlike the untreated model, the presence of the resin edges in the treated model permits convergence at the CFRP edge. Therefore, stresses can be taken at the CFRP edge-resin treatment boundary and are not arbitrary, unlike the untreated laminate stresses used to produce Fig. 3.27. Figure 4.21 shows the result of Eq. (3.45) evaluated from the G39B(R) model, at a distance of one element (8 μm) from the CFRP edge-resin treatment boundary, at the apex of the corner, through thickness. Stresses are ideally measured as close to the CFRP edge as possible, since this is where they are highest. However, taking them along the node line of the boundary would result in the averaging of stresses in the resin edge and CFRP section. From this analysis, a CBS of 8.35 kN/mm is predicted, giving a conservative result within 3.5% of the average experimental failure (8.65 kNmm/mm). Failure is predicted

at interface 5, towards the outer radius, where experimental specimens exhibited delamination, as well as in other locations (see Fig. 4.16a). It is noted however, that there are several peaks in Fig. 4.21 that are close to failure. In contrast to the untreated laminate failure criterion, the greatest four peaks (A-D) are dominated by interlaminar shear, τ_{23}. The peaks labelled E and F are dominated by σ_{33} and τ_{13} respectively. Peak E is coincident with the greatest peak in Fig. 3.27 for the untreated laminate.

Similarly, the failure criterion plots from FE models of S24(R), S44(R), N24(R) and N44(R) are shown, respectively, in Fig. 4.22 through to Fig. 4.25. The subsequent predictions for CBS and failure location are summarised in Table 4.2, compared against the average experimental results. The Camanho failure criterion is found to give accurate prediction for the G and S specimens, which have a more conventional balanced, symmetric layup, typical of industrial use. However, for the N specimens, which have a novel anti-symmetric layup and 0° plies more clustered together, the Camanho failure criterion does not accurately predict the CBS. The prediction is highly un-conservative for the thicker N44(R) specimens in particular; the criterion does not appear to capture the correct failure mode for these specimens, since the failure location is at odds with the experimental results. This discrepancy is addressed subsequently in Section 4.5.

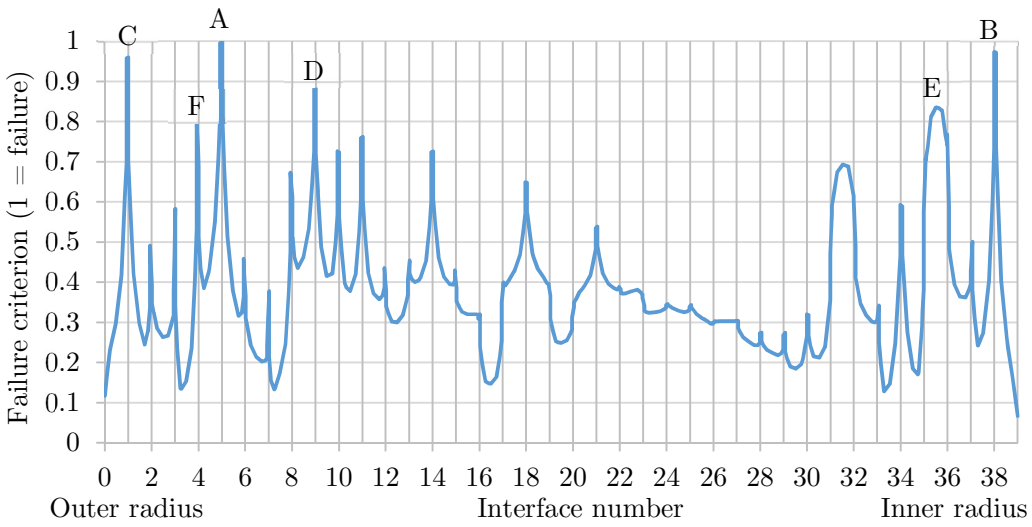

Figure 4.21 Failure criterion evaluated at the corner apex, one element from CFRP edge-resin treatment boundary, through the thickness of the G39B(R) FE model. The value of applied running moment is 8.35 kNmm/mm.

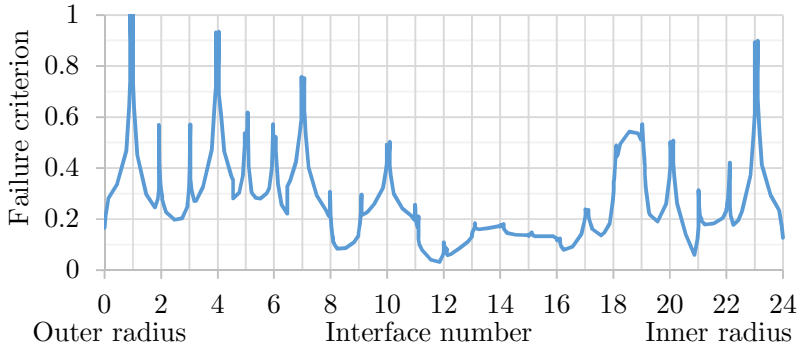

Figure 4.22 Failure criterion for S24(R) model. 2.31 kNmm/mm applied.

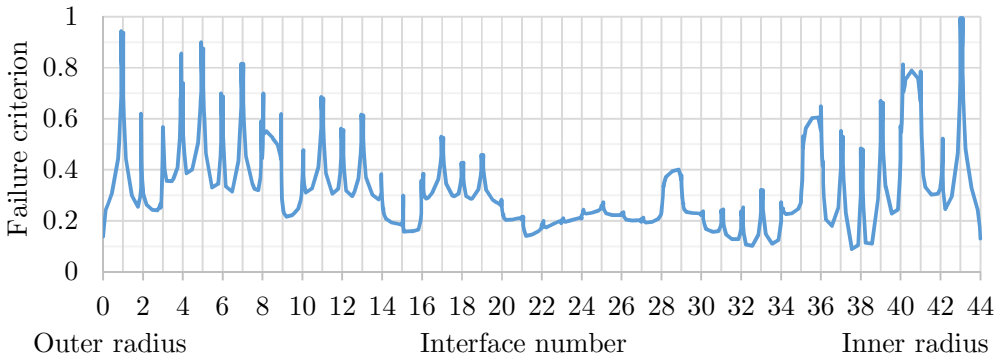

Figure 4.23 Failure criterion for S44(R) model. 5.58 kNmm/mm applied.

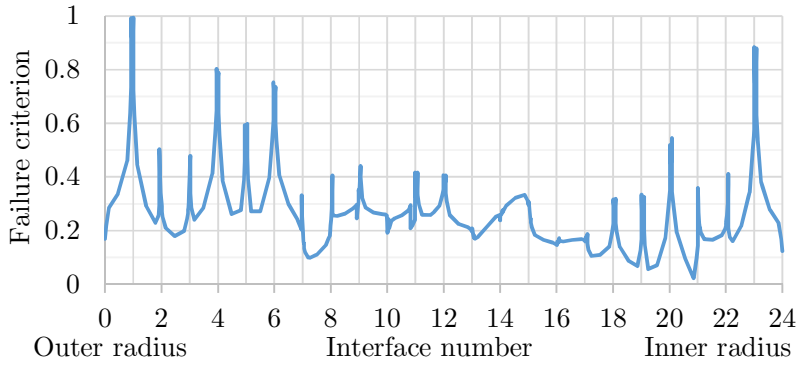

Figure 4.24 Failure criterion for N24(R) model. 2.35 kNmm/mm applied.

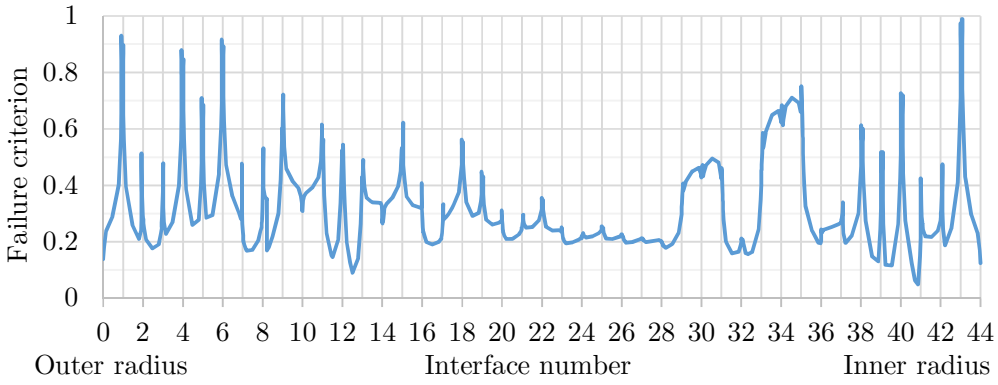

Figure 4.25 Failure criterion for N44(R) model. 5.59 kNmm/mm applied.

Specimen Type	CBS (kNmm/mm)			Failure location	
	Exp.	FE	Error (%)	Experimental	FE
G39B(R)	8.65	8.35	-3.5	Int. 1-37	Int. 5
S24(R)	2.30	2.31	+0.4	Int. 1-23 (all)	Int. 1
S44(R)	5.23	5.58	+6.7	Int. 30-43	Int. 43
N24(R)	2.00	2.35	+17.5	Int. 1-23 (all)	Int. 1
N44(R)	3.92	5.59	+42.6	Int. 26-36	Int. 43

Table 4.2 CBS and failure location predictions from FE models of resin treated curved laminates, based solely on Camanho failure criterion, compared with average experimental result.

4.5 Improved Failure Prediction

The discrepancy between the N24(R) and N44(R) model predictions for CBS, and that of the experimental test specimens (see Table 4.2) is addressed. In doing so, the modelling of all specimen types is refined.

4.5.1 Comparison of Predictions Against Experimental Results

The experimental failure location for the N44(R) specimens is shown in Fig. 4.26, and for N24(R) in Fig. 4.27. The failure of N44(R) specimens is consistently concentrated between plies 26-37. However, the Camanho failure criterion peak is at interface 43 (between plies 43-44) in Fig. 4.25. Experimentally, the N44(R) specimens consistently failed at a significantly lower CBS than the S44(R) specimens. This is not predicted by the Camanho failure criterion, which predicts approximately the same CBS for both specimen types.

The FE models of S44(R) and N44(R) are interrogated to find the cause of the lower CBS results for N44(R) specimens, and improve the model prediction. At an applied running moment of 4 kNmm/mm, the out-of-plane stresses are shown in Fig. 4.28 and the in-plane stresses in Fig. 4.29 for the two 44-ply specimen types. These are evaluated at the corner apex, one element away from the CFRP edge-resin treatment boundary, where failure is likely to first initiate. One of the most significant differences between S44(R) and N44(R) models is the direct through thickness stress, shown in Fig. 4.28a. Specifically, there are large peaks for the N44(R) model between interfaces 29-31 and 33-35. Although the highest peak for S44(R) is higher, this resides within a fibrous ply (ply 41); whereas there are high peaks within pure resin interfaces of N44(R), in particular interface 34. For clarity, Fig. 4.30 shows the value of σ_{33} at the centre of each interface only. There is a cluster of peaks for the N44(R) model in the vicinity of the cluster of 0° plies nearest the inner radius. Most significantly, it appears the existence of two 0° plies adjacent to one another results in a high level of stress within the joining interface. The S44(R) laminate does not have adjacent 0° plies, except for at the centre of the stack (interface 22), where stresses are generally low and no significant peak is observed.

a) N44(R)-03 front side **b)** N44(R)-03 back side

c) N44(R)-04 front side **d)** N44(R)-04 back side

Figure 4.26 N44(R) specimens immediately after failure during experimental testing.

The CBS for N24(R) specimens is also over-predicted in Table 4.2 and is now analysed. Whereas failure location of the 44-ply specimens is relatively consistent, there appear to be two distinct failure modes experimentally for 24-ply specimens. Specimens either fail in the close vicinity of ply 3 (see for example Fig. 4.27a), which is the outer-most 90° ply, where maximum compressive stress due to bending is seen, often with a single, distinct delamination; or they fail closer to the inner radius, between plies 8-24, when typically several delaminations appear simultaneously (see for example Fig. 4.27b). A few specimens exhibit both, with delamination visible around ply 3 and at ply levels all the way to the inner radius at ply 24.

The FE models of S24(R) and N24(R) are interrogated. At an applied running moment of 2 kNmm/mm, the out-of-plane stresses are shown in Fig. 4.31 and the in-plane stresses in Fig. 4.32 for the two 24-ply specimen types. Unlike N44(R), N24(R) does not exhibit high peaks in σ_{33} within the interfaces (Fig. 4.31a). Most notably, Fig. 4.32b indicates a compressive σ_{22} beyond the manufacturer quoted allowable within the outer most 90° ply (ply 3). Such bending induced compressive fibre failure has been found to be critical under impact loading, especially for thin ply laminates [90]. The different stacking sequence for S24 and N24 specimens causes a shift in the neutral axis, indicated by Fig. 4.32b, which shows increased compressive σ_{22} at ply 3, and reduced tensile σ_{22} at ply 22 for the N24(R) model, as compared with the S24(R) model. Note that the tensile stress at ply 22 is less than half the manufacturer quoted

allowable; plies are generally significantly stronger in tension than in compression along the fibre direction. The reduction in tensile σ_{22} at ply 22 and increase in compressive σ_{22} at ply 3 for the N24(R) specimens is therefore likely to result in earlier failure and lower CBS; as compared with the S24(R) specimens, which are less likely to fail at ply 3. This is consistent with the evidence from untreated (S24 and N24) 24-ply specimen tests: all 13 N24 specimens fail in the vicinity of ply 3; whereas the S24 specimens fail in this location in 7 out of 12 tests, the other 5 failing closer to the mid-thickness and inner radius.

a) N24(R)-03, failure at plies 1-5

b) N24(R)-02, failure at plies 9-24

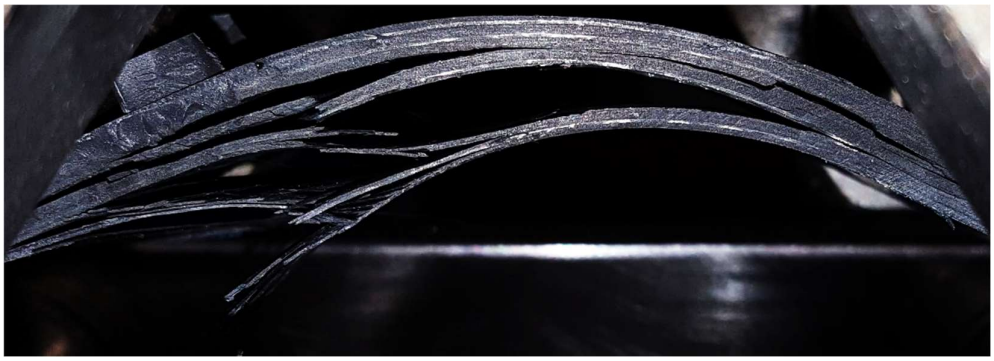

Figure 4.27 N24(R) specimens immediately after failure during experimental testing.

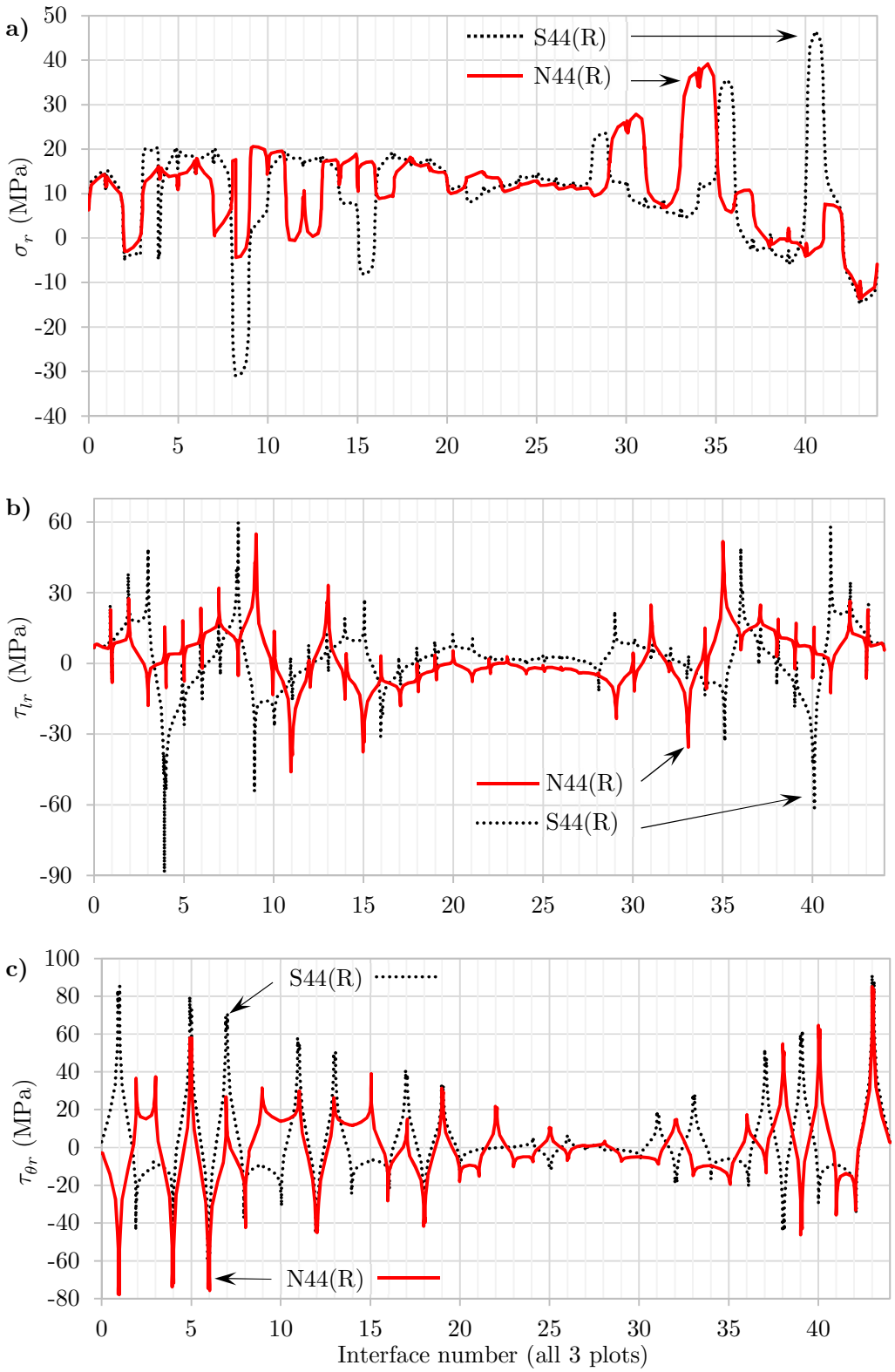

Figure 4.28 Out-of-plane stress components for 44-ply FE models at the corner apex, one element from the CFRP edge-resin treatment boundary. Running moment of 4 kNmm/mm applied.

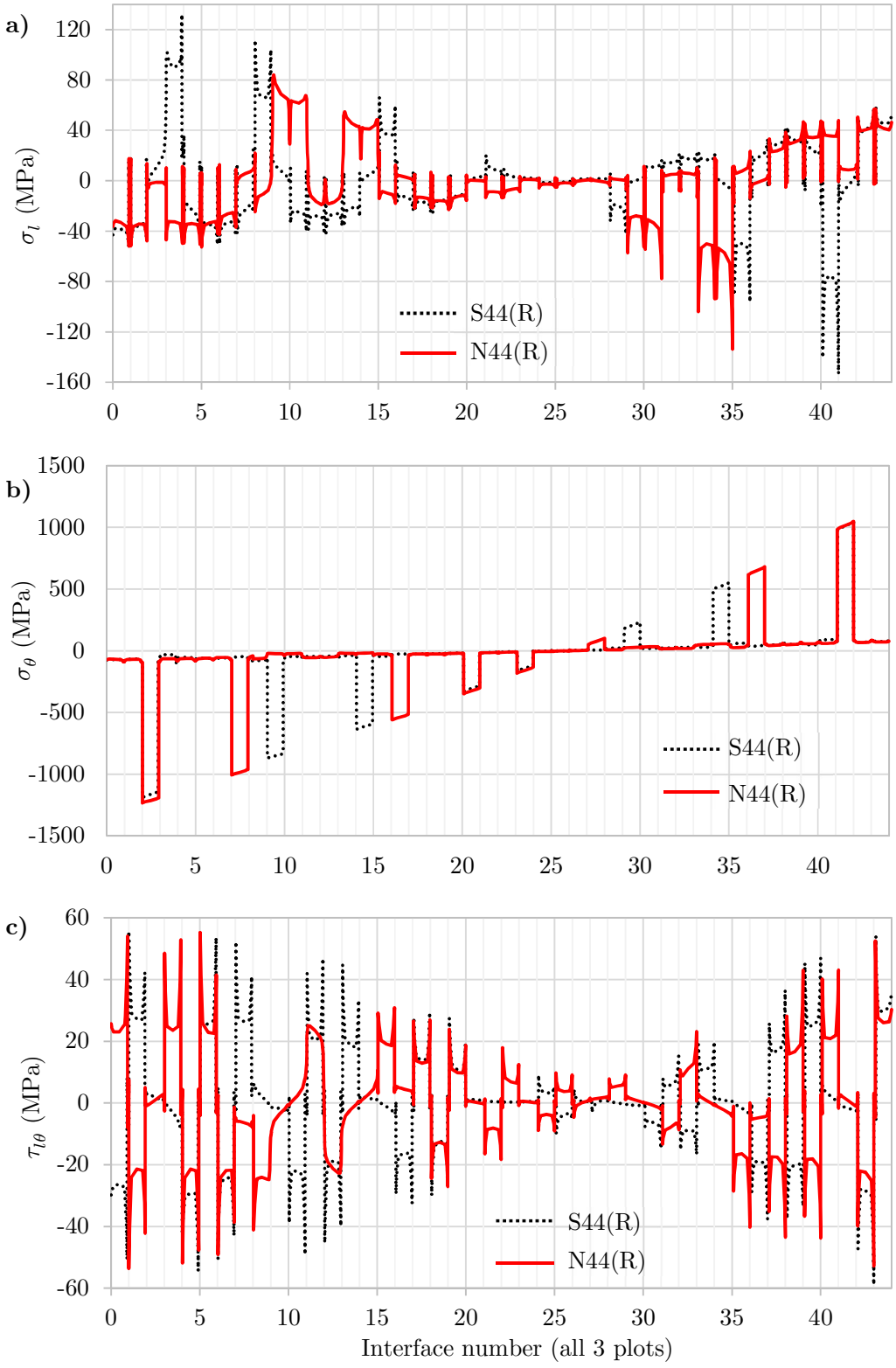

Figure 4.29 In-plane stress components for 44-ply FE models at the corner apex, one element from the CFRP edge-resin treatment boundary. Running moment of 4 kNmm/mm applied.

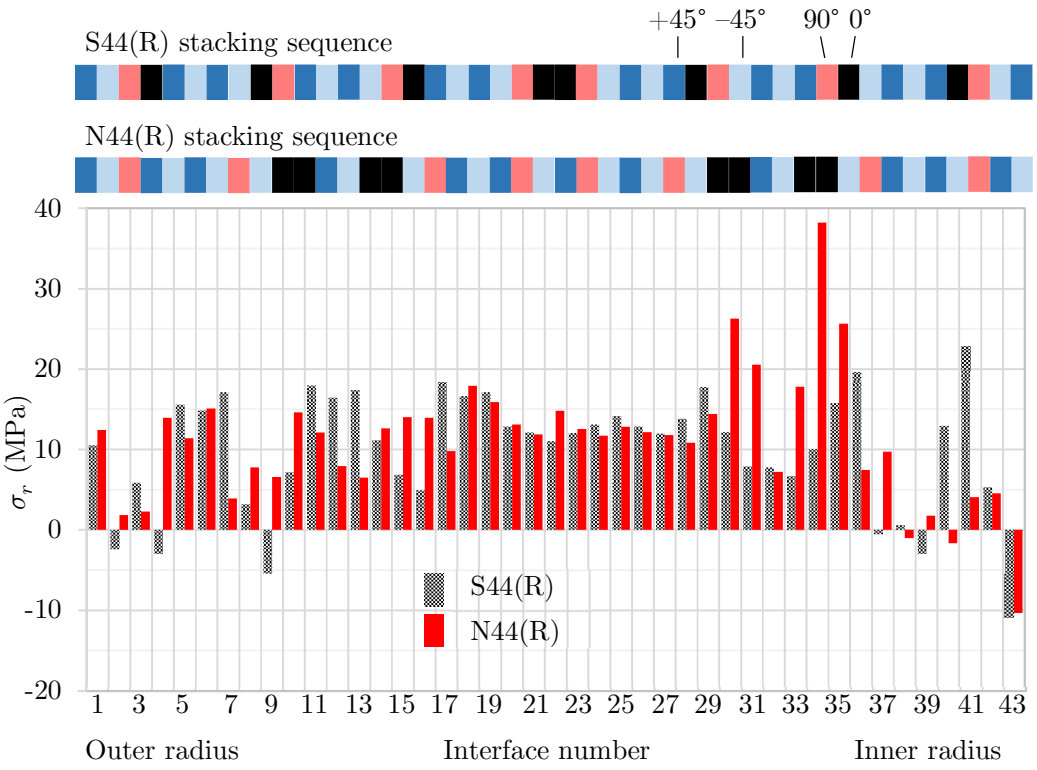

Figure 4.30 Direct through thickness stress for interfaces of 44-ply models. The stacking sequence of the N44(R) laminate is shown above plot. Highest N44(R) peaks occur in the vicinity of the 0° ply cluster closest to inner radius.

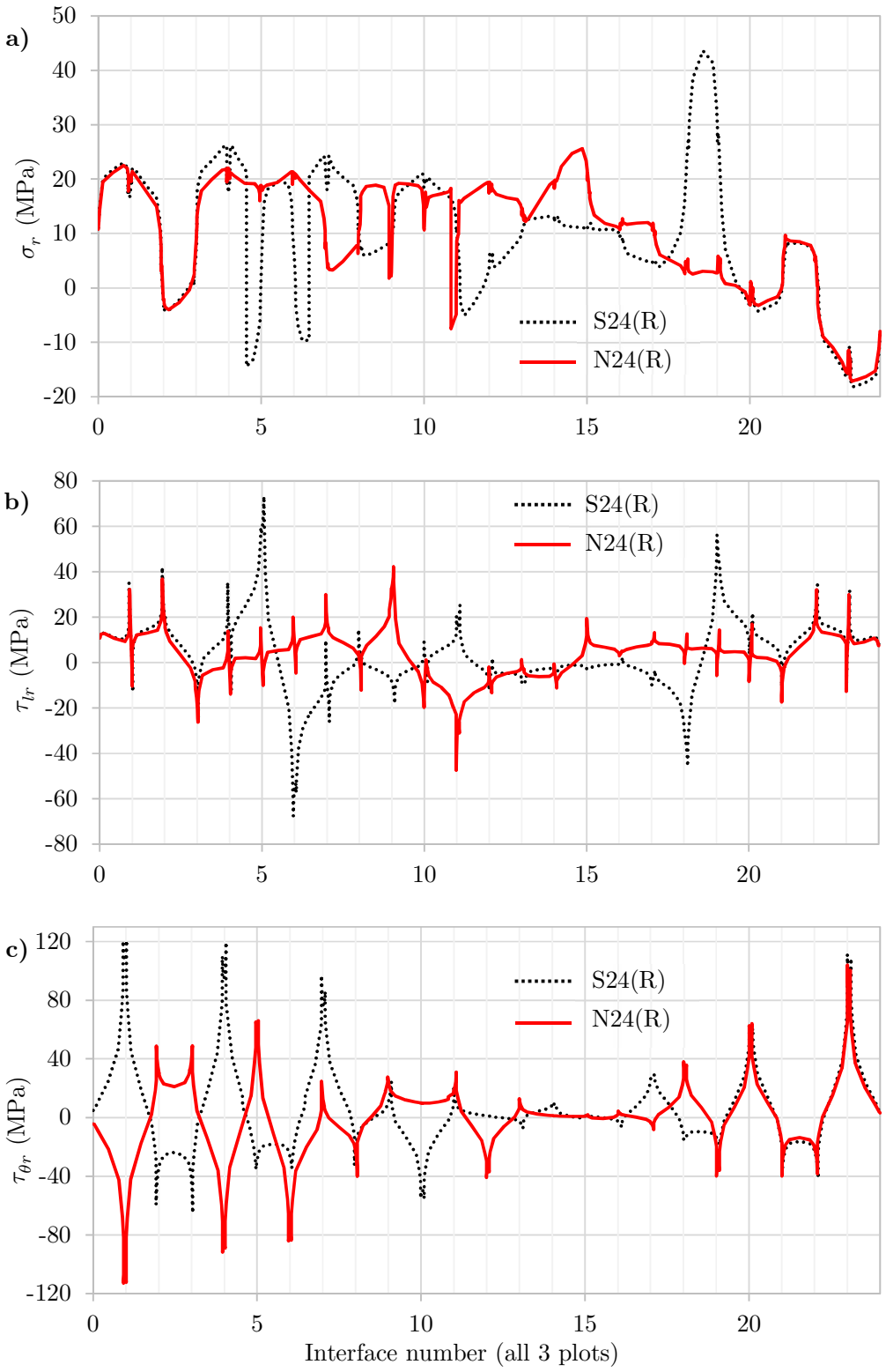

Figure 4.31 Out-of-plane stress components for 24-ply FE models at the corner apex, one element from the CFRP edge-resin treatment boundary. Running moment of 2 kNmm/mm applied.

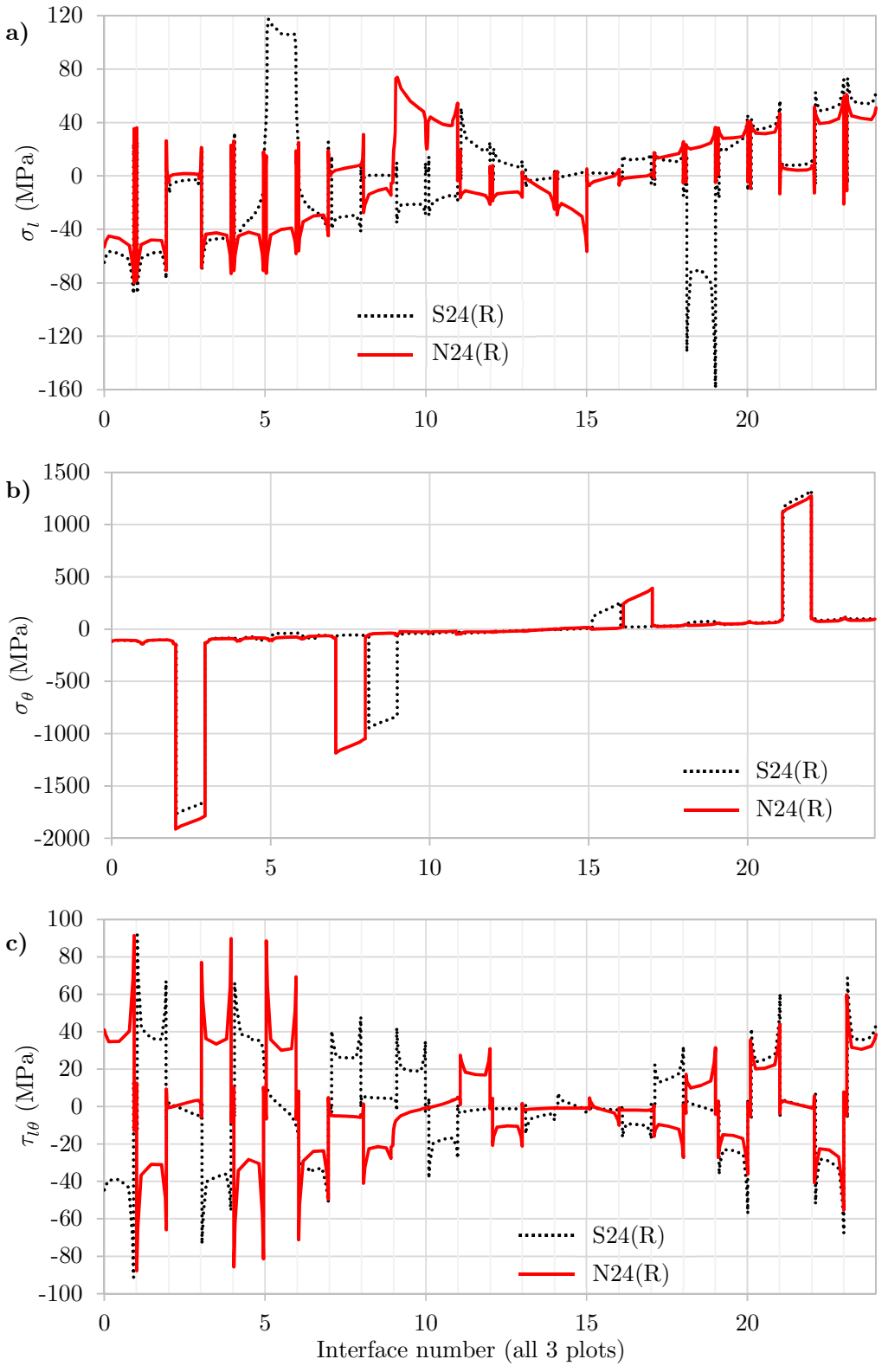

Figure 4.32 In-plane stress components for 24-ply FE models at the corner apex, one element from the CFRP edge-resin treatment boundary. Running moment of 2 kNmm/mm applied.

4.5.2 Updated Material Properties

For the predictions in Table 4.2, it is assumed the σ_{33} allowable within the interface is equal to the 90° tensile strength quoted by the manufacturer. This appears to be inadequate. It has been found that the σ_{33} allowable is typically lower than the transverse tensile strength [91]. The interlaminar tensile strength (σ_{33} allowable) of composite laminates is difficult to reliably ascertain experimentally. The ASTM D 6415 standard is proposed as a method for determining interlaminar tensile strength, but it is noted that data from this test exhibits large scatter and may be coupon specific [92]. A range of values are found in the literature but a comprehensive experimental programme was conducted by the National Institute for Aviation Research (NIAR), supported by the National Center for Advanced Materials Performance (NCAMP) and National Aeronautics and Space Administration (NASA) [93]. This report for 8552/AS4 unidirectional prepreg gives a mean interlaminar tensile strength of 54.5 MPa, which is significantly lower than the Hexcel quoted transverse (90°) tensile strength of 81 MPa.

The transverse shear strength f_{23} is difficult to obtain experimentally but can be derived from the expression given by [94]:

$$f_{23} = f_{22}^{c} \ \cos\alpha_0 \left(\sin\alpha_0 + \frac{\cos\alpha_0}{\tan 2\alpha_0} \right) \quad , \tag{4.2}$$

where α_0 is the fracture angle and typically ranges between 51-55° for glass and carbon composites, but can be taken as 53° [91-97]. A transverse compression strength f_{22}^{c} of 268 MPa is given by [93], giving a transverse shear strength of 101 MPa from Eq. (4.2).

The longitudinal tensile and compression strengths are typically obtained by loading a stack of 0° plies in the fibre direction to failure. Quoted stress values, for example in [13] and [93], are typically then calculated by dividing the failure load by the cross-sectional area, based on total thickness. This therefore gives the smeared strength across fibrous ply and resin interface. Since the fibrous plies and resin interfaces are modelled separately in this thesis, the quoted values are scaled to find the fibrous ply strength by neglecting the strength contribution of the interface, i.e.

$$f_{11,fib} = f_{11,fib+int} \ \frac{t_{fib+int}}{t_{fib}} \quad , \tag{4.3}$$

where $f_{11,fib+int}$ is the strength value quoted in the literature for the combination of fibrous and interface layer, $t_{fib+int}$ is the total thickness of fibrous layer and interface

(0.18 mm for 8552/AS4) and t_{fib} is the thickness of the fibrous layer only (0.16 mm for 8552/AS4).

The resin interface is modelled with the elastic modulus of pure resin, quoted by the manufacturer. Table 4.3 details all the 8552/AS4 material properties used for the FE model and failure criteria. The updated properties for M21/IMA are listed in Table 4.4, with the properties of pure resin now used for the resin interface.

Fibrous layer		Source	Allowables		Source
E_{11} (GPa)	135	[13]	f_{11}^t (MPa)	2480	[13]*
E_{22}, E_{33} (GPa)	10	[13]	f_{11}^c (MPa)	1720	[13]*
G_{12}, G_{13} (GPa)	4.83	[93]	f_{22}^c (MPa)	268	[93]
G_{23} (GPa)	3.35	[91]	f_{33}^t (MPa)	54.5	[93]
v_{12}, v_{13}	0.32	[93]	f_{23} (MPa)	101	Eq. (4.2)
v_{23}	0.49	[91]	f_{13} (MPa)	115	[93]
			f_{12} (MPa)	114	[13]
Resin interface		Source	*using Eq. (4.3) as described in text.		
E (GPa)	4.67	[13]			
v	0.35	typical			

Table 4.3 Assumed 8552/AS4 material properties for FE models and failure criteria.

Fibrous layer		Source	Allowables		Source
E_{11} (GPa)	162	[36]	f_{11}^t (MPa)	3320	[36]*
E_{22}, E_{33} (GPa)	10	[36]	f_{11}^c (MPa)	1630	[36]*
G_{12}, G_{13} (GPa)	5.2	[36]	f_{22}^c (MPa)	250	[40]
G_{23} (GPa)	3.5	[40]	f_{33}^t (MPa)	61	[40]
v_{12}, v_{13}	0.35	[40]	f_{23} (MPa)	94	Eq. (4.2)
v_{23}	0.5	[40]	f_{13} (MPa)	97	[36]
			f_{12} (MPa)	94	[36]
Resin interface		Source	*using Eq. (4.3) as described in text.		
E (GPa)	3.5	[98]			
v	0.35	typical			

Table 4.4 Assumed M21/IMA material properties for FE models and failure criteria.

4.5.3 Updated CBS Predictions

The updated material properties are used to refine the FE models of the curved laminates. However, it was determined in Section 4.5.1 that the Camanho failure criterion doesn't accurately predict the failure in all cases. This criterion predicts delamination, which is often the dominate failure mode in laminated materials, but there are other ways in which laminates can fail.

Ye & Zhang [99] and Christensen [100,101], amongst others, propose that the failure of composites can naturally be broken down into matrix dominated failure and fibre dominated failure. From [99,101], matrix dominated failure is predicted to occur when

$$\begin{aligned}&\left(\frac{1}{f_{22}^t}-\frac{1}{f_{22}^c}\right)(\sigma_{22}+\sigma_{33})+\frac{1}{f_{22}^t f_{22}^c}(\sigma_{22}+\sigma_{33})^2\\&+\frac{1}{{f_{23}}^2}({\tau_{23}}^2-\sigma_{22}\sigma_{33})+\frac{1}{{f_{12}}^2}({\tau_{12}}^2+{\tau_{13}}^2)\geq 1\end{aligned}\quad , \tag{4.4}$$

where $f_{23}\geq\frac{1}{2}\sqrt{f_{22}^t f_{22}^c}$ for real roots to exist, which is comfortably satisfied for both 8552/AS4 and M21/IMA mechanical properties. Note that for the resin interfaces of the model, f_{22}^t is taken as f_{33}^t from Table 4.3 and Table 4.4. Delamination is generally less likely to occur between two plies with the same fibre orientation since there is no mismatch in mechanical properties between them. Indeed, often such plies would be modelled as one thicker ply of the common fibre orientation. The Camanho failure criterion does not predict delamination between the 0° ply pairs of the N44(R) specimens (interfaces 30 and 34) in Fig. 4.25, yet experimentally failure is observed in this region (Fig. 4.26). Instead, where two adjacent plies of common fibre orientation exist, Christensen failure criterion is used to predict when the triaxial stresses exceed the strength limit of the resin interface between them, as per Eq. (4.4).

Complimentary to the matrix dominated failure, [99,101] propose that fibre dominated failure will occur when the axial stress in the fibre direction is outside the range

$$-f_{11}^c\leq\sigma_{11}\leq f_{11}^t \quad . \tag{4.5}$$

This criterion is used to assess when the longitudinal stress (in the fibre direction) exceeds the strength limit of the fibrous layer.

Figure 4.33 shows the Camanho (Eq. (3.45)) and Christensen (Eq. (4.5)) failure criteria at the mid-thickness of each fibrous ply and pure resin interface for the G39B(R) model. Equation (4.5) is assessed within the fibrous plies only. Equation

(3.45) is assessed within both the fibrous plies and resin interfaces, with the highest failure index shown in Fig. 4.33. The failure index reaches 1 for Camanho failure criterion within interface 5, at an applied running moment of 8.42 kNmm/mm, which is therefore the predicted CBS. This location is within the range of ply levels that exhibit failure experimentally.

Figure 4.34 and Fig. 4.35 show the same for the S44(R) and N44(R) models respectively. Christensen failure criterion for matrix failure (Eq. (4.4)) is also assessed for the interfaces between plies with a common fibre orientation. Failure is predicted at 5.11 kNmm/mm within ply 41 for S44(R) and at 3.86 kNmm/mm within interface 34 for N44(R). Failure at these locations is observed experimentally.

Finally, the failure criteria are shown for S24(R) and N24(R) models in Fig. 4.36 and Fig. 4.37, respectively. Failure is predicted within ply 3 by fibre failure for both, with a lower CBS for N24(R) than S24(R), consistent with experimental observations. A higher failure index is indicated at other locations, including nearer the inner radius, for the S24(R) model than the N24(R) model. This likely explains why failure at locations nearer the inner radius are more commonly observed experimentally for the S24/S24(R) specimens than the N24/N24(R) specimens.

The CBS of all specimen types is now conservatively predicted to within a reasonable degree of accuracy, as summarised in Table 4.5, by considering both Camanho and Christensen failure criteria.

Specimen Type	CBS (kNmm/mm)			Failure location	
	Exp.	FE	Error (%)	Experimental	FE
G39B(R)	8.65	8.42	-2.7	Int. 1-37	Int. 5
S24(R)	2.30	2.16	-6.1	Ply 1-24 (all)	Ply 3
S44(R)	5.23	5.11	-2.3	Ply 30-44	Ply 41
N24(R)	2.00	1.87	-6.5	Ply 1-24 (all)	Ply 3
N44(R)	3.92	3.86	-1.5	Int. 26-36	Int. 34

Table 4.5 CBS and failure location predictions from FE models of resin treated curved laminates, based on Camanho and Christensen failure criteria. Compared against average experimental data.

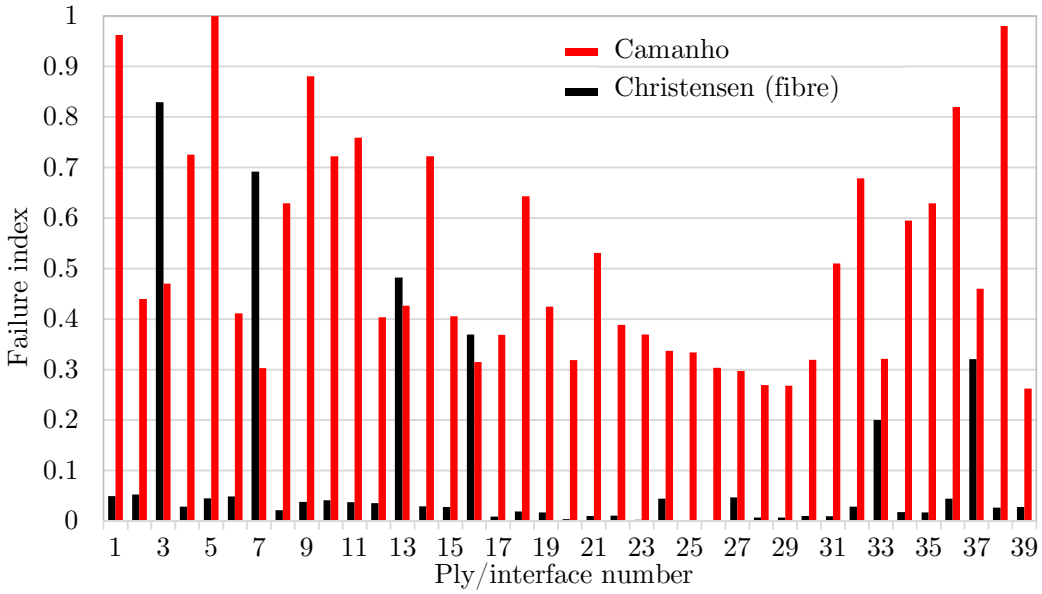

Figure 4.33 Failure criteria at mid-thickness of each fibrous ply and resin interface for G39B(R) FE model. 8.42 kNmm/mm applied running moment, stresses taken at corner apex, one element from CFRP edge-resin treatment boundary.

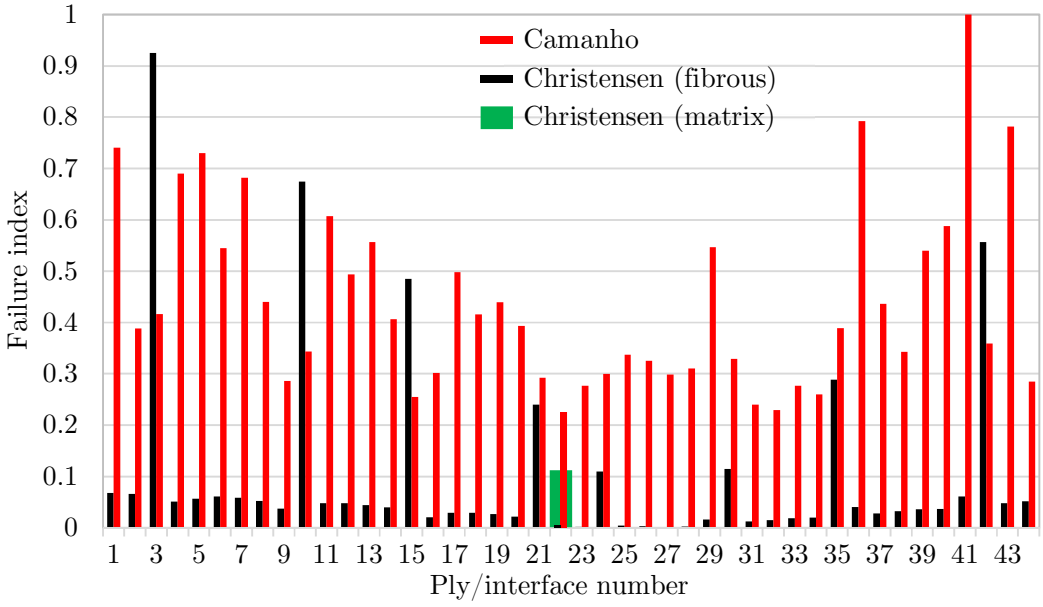

Figure 4.34 Failure criteria at mid-thickness of each fibrous ply and resin interface for S44(R) FE model. 5.11 kNmm/mm applied running moment, stresses taken at corner apex, one element from CFRP edge-resin treatment boundary.

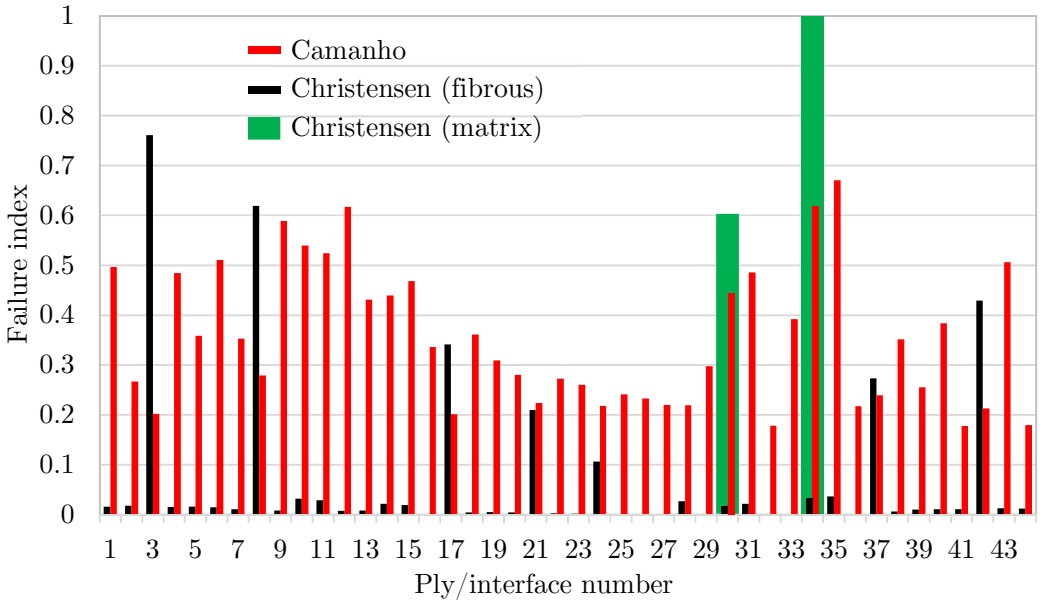

Figure 4.35 Failure criteria at mid-thickness of each fibrous ply and resin interface for N44(R) FE model. 3.86 kNmm/mm applied running moment, stresses taken at corner apex, one element from CFRP edge-resin treatment boundary.

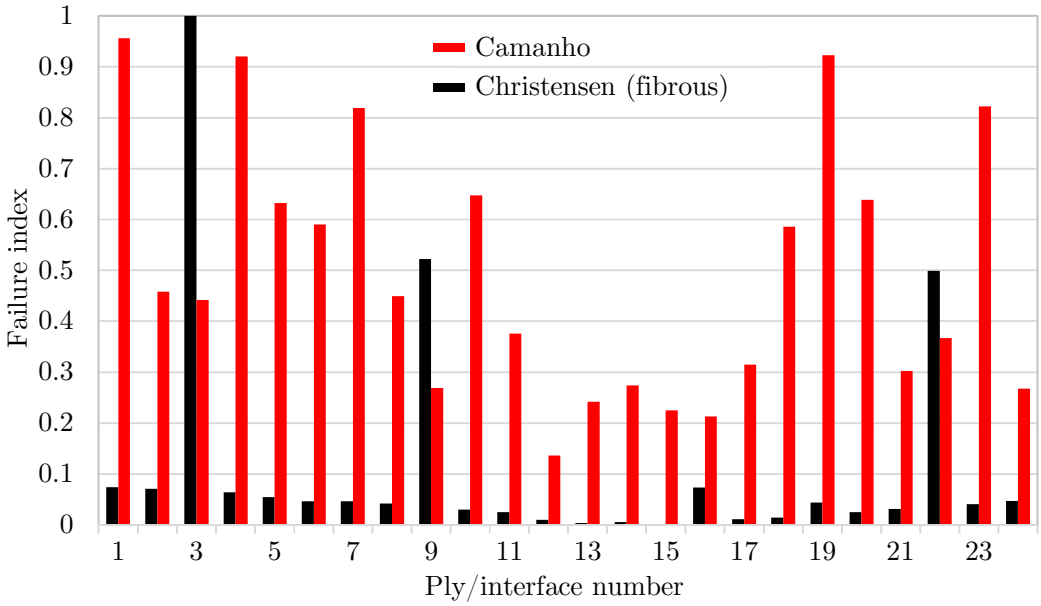

Figure 4.36 Failure criteria at mid-thickness of each fibrous ply and resin interface for S24(R) FE model. 2.16 kNmm/mm applied running moment, stresses taken at corner apex, one element from CFRP edge-resin treatment boundary.

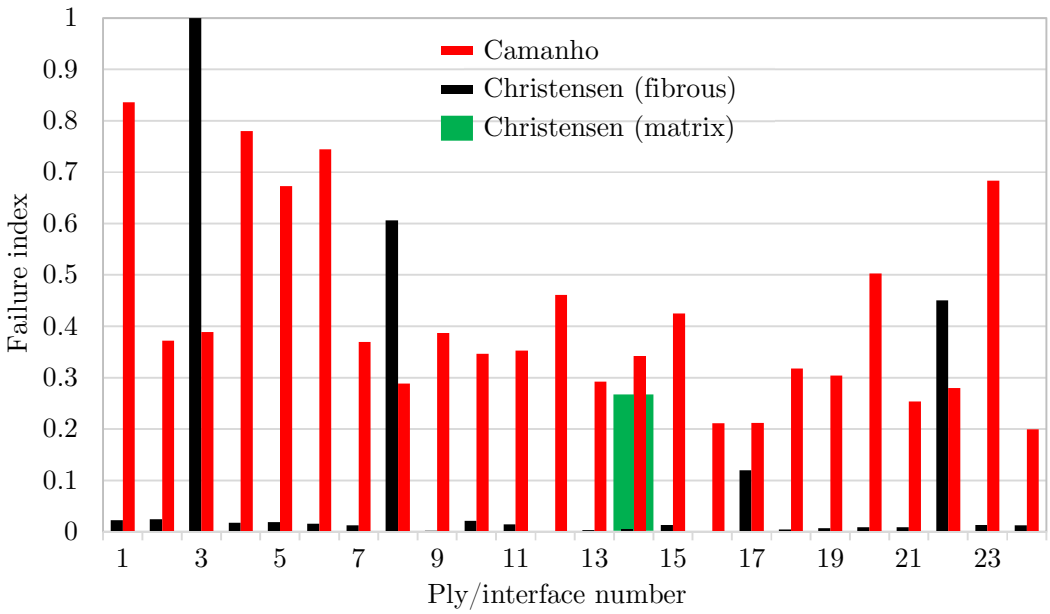

Figure 4.37 Failure criteria at mid-thickness of each fibrous ply and resin interface for N24(R) FE model. 1.87 kNmm/mm applied running moment, stresses taken at corner apex, one element from CFRP edge-resin treatment boundary.

4.6 Load vs Displacement

The load vs displacement during the experimental testing of specimens with and without resin edge treatment is shown in Fig. 4.38. The resin treated specimens exhibit a small increase in stiffness, carrying 3.8% more load at 5 mm displacement. This is partly due to the increase in the stress carried by the laminate near the edge and partly due to the stiffness contribution of the resin edge. Much more significant is the increase in load and displacement to failure of the resin treated specimens. On average the treated specimens deflect 12% more and carry 21% more load at the point of failure. The resin edge treatment significantly increases specimen strength with minimal effect on stiffness.

The load vs displacement prediction from the FE model simulation is also shown in Fig. 4.38. The simulation predicts the strength and stiffness of the treated specimens accurately, generally slightly under-predicting both. The materials are modelled as linear elastic, which appears to under predict the initial stiffness compared with the experimental data in Fig. 4.38. However, the real material exhibits a non-linear response, which reduces the stiffness at high load, where the FE model shows a slightly stiffer response compared with the experimental data. In-spite of this material behaviour, the gradient of both experimental and simulation data appears to increase

with increasing displacement in Fig. 4.38. This is because of the non-linear geometrical affect, which reduces the mechanical advantage of the test rig as displacement increases. The simulation captures this aspect of non-linearity.

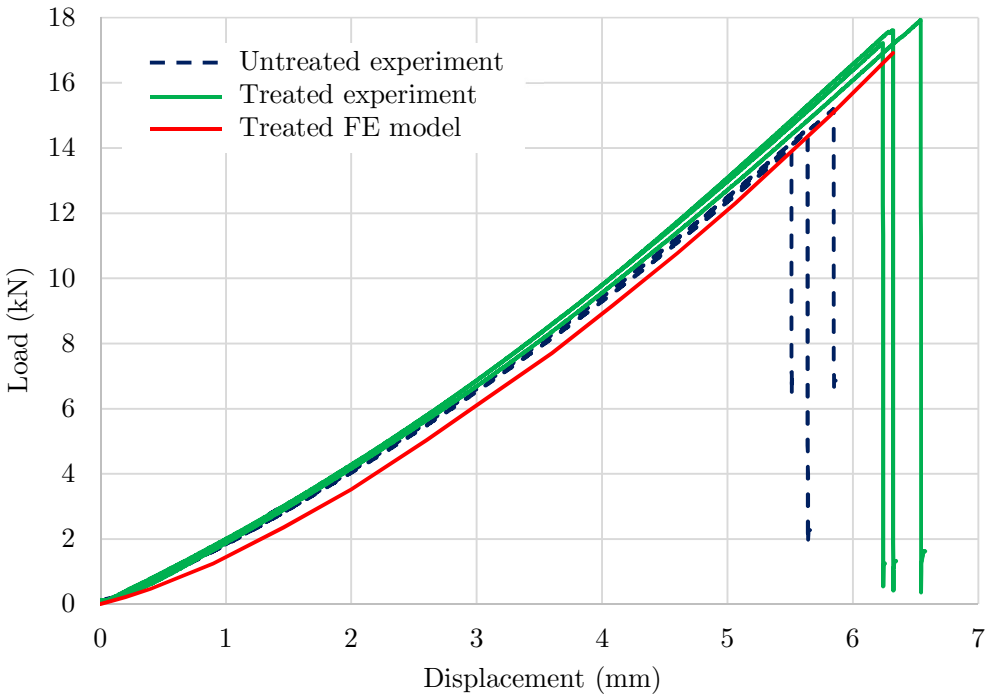

Figure 4.38 Load vs displacement for G39B specimens with and without resin edge treatment, tested experimentally. Also shown is the prediction of the FE model for the specimens with treatment.

4.7 Specimen Defects

Pristine specimens are assumed for the FE models of the curved laminates; defects such as wrinkles are not modelled. However, experimental specimens contain some level of imperfections. It is found that the S44(R) (Fig. 4.39) and N44(R) (Fig. 4.40) are most notably defective in terms of ply wrinkling, much more so than other specimens. Wrinkles are especially visible in Fig. 4.39c and Fig. 4.40c. 90° plies appear brightest in the micrographs. In Fig. 4.39a and Fig. 4.40b, the 2nd outer-most 90° ply appears thinner than the rest of the plies. This is found to be localised and the same ply is closer to the nominal thickness on the opposite free edge in both cases. The thinner appearance in Fig. 4.39a and Fig. 4.40b is likely due to the specimen being sectioned on the edge of a tow gap between two adjacent 90° tows, which form part of the same ply. Tow gaps between 0° plies appear as dark patches and between ±45° plies appear

as elongated dark patches. The increased level of defects in 44-ply specimens possibly explains why the FE predictions for the S44(R) / N44(R) specimen types are less conservative than for S24(R) / N24(R) specimen types in Table 4.5. However, a clear correlation between defects and CBS is not found. For example, N44(R)-03 appears visibly more defective (Fig. 4.40c) than other N44(R) specimens (Fig. 4.40a,b,d), yet does not exhibit a lower CBS.

In contrast the G39B(R) specimens appear to have relatively uniform ply thickness and do not exhibit any visible wrinkling. Figure 4.41 shows G39B(R)-01 as an example but is also representative of -02 and -03. The G39B specimens were manufactured to production standard using a more highly refined process than the experimental manufacture of S44 and N44 specimens. Although S24 and N24 specimens were manufactured using the same process as S44 and N44, they do not exhibit visible wrinkling, as shown in Fig. 4.42, which is representative of all S24 and N24 specimens. The thinner profile reduces the chances of a defect forming, with significantly less movement during de-bulk and cure.

a) S44(R)-01

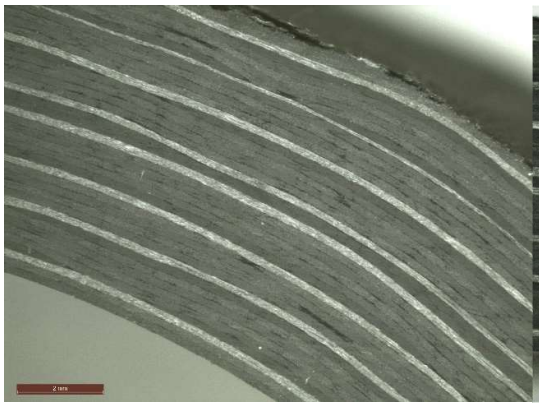

b) S44(R)-02

c) S44(R)-03

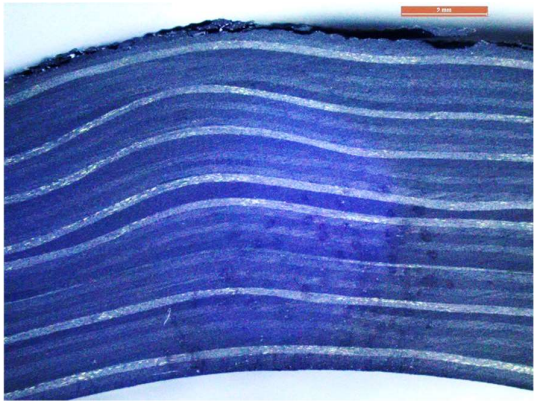

Figure 4.39 Micrographs of S44(R) specimens before application of resin edge.

a) N44(R)-01 **b)** N44(R)-02

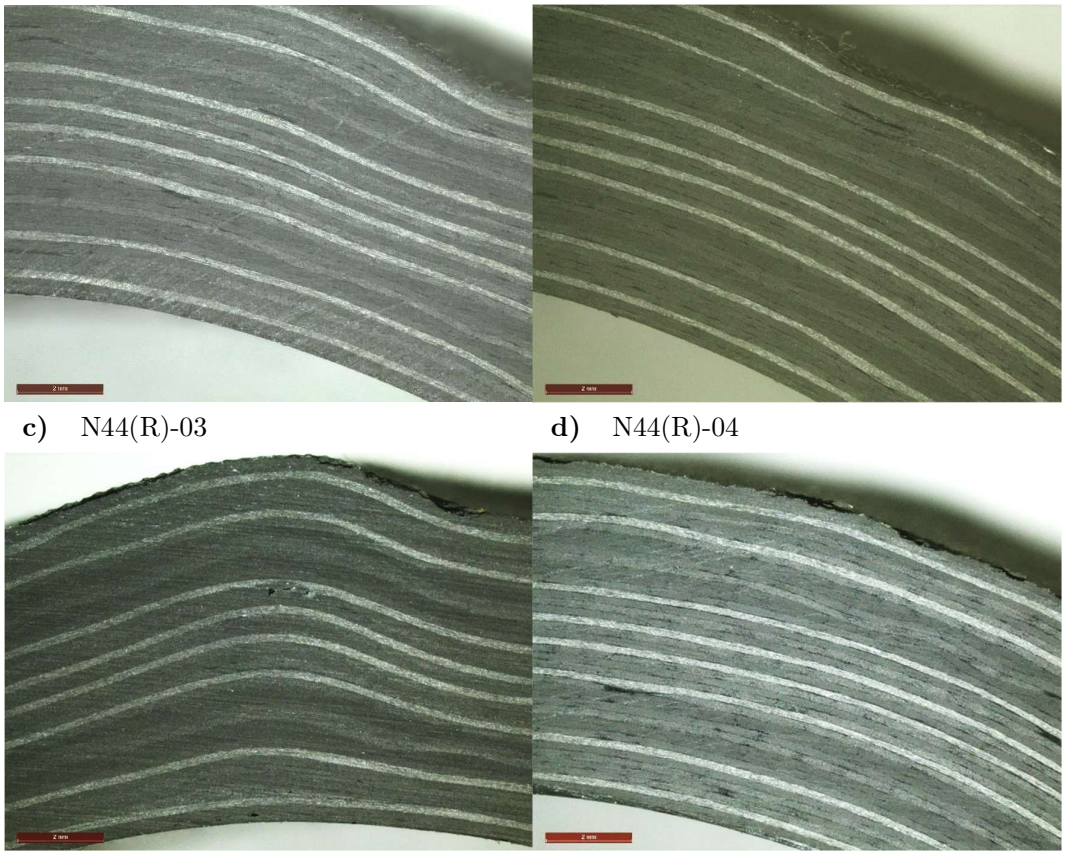

c) N44(R)-03 **d)** N44(R)-04

Figure 4.40 Micrographs of N44(R) specimens before application of resin edge.

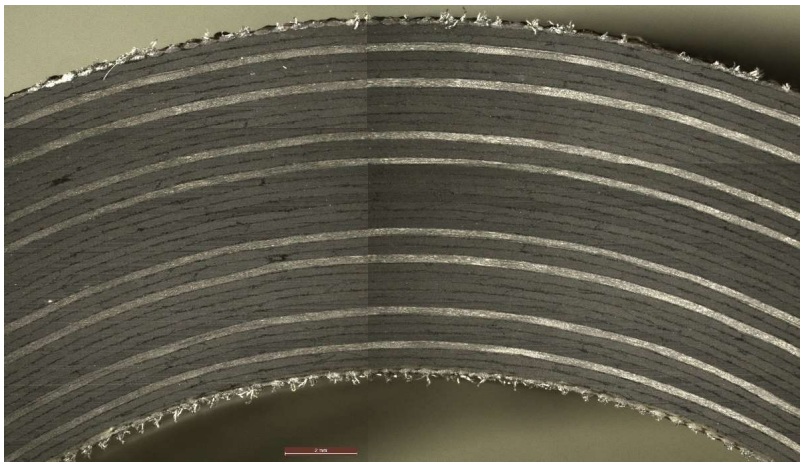

Figure 4.41 Micrograph of G39B(R)-01 before application of resin edge.

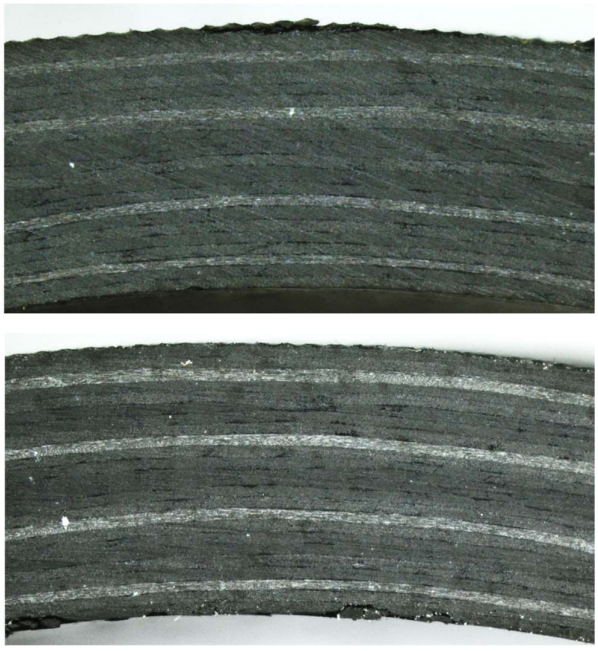

Figure 4.42 Micrographs of **a)** N24(R)-05 and **b)** S24(R)-02 before application of resin edge.

4.8 Closing Remarks

The edge effect is examined in this chapter. An explanation is given for the initiation of failure from the free edge of curved laminates under 4-point bending. Methods in the literature for mitigating the edge effect are studied and an original method is developed, more suitable for application to witness specimens cut from production parts. The novel approach consists of a resin edge treatment and shows a useful improvement in CBS for a range of specimen types. However, the level of improvement depends on the specimen type; the resin edge treatment appears to suppress certain stresses and modes of failure more significantly than others. The novel stacking sequence design N44 fails under a different mode (Christensen matrix failure criterion) from the symmetric counter-part: S44. The resin edge treatment does not appear to increase CBS for this mode as much as for the more conventional G39B and S44 designs, which are predicted to fail according to Camanho failure criterion. Accurate prediction of failure location and CBS is achieved for all specimen types by considering both the Camanho and Christensen failure criteria. The effect of the resin treatment on stresses in the vicinity of the CFRP edge is analysed in more detail in Chapter 5, with varying resin mechanical properties.

5 ANALYSIS OF RESIN TREATED LAMINATES

The effect of the resin treatment on near-edge stresses is analysed in more detail, with varying resin modulus. The confidence in the FE modelling is assessed with a series of sensitivity studies, to understand the importance of variations in material properties and specimen geometry. It is noted that for particular specimen types and resin edge material, failure of the resin edge may occur first, rather than failure initiating within the CFRP laminate. Failure of the resin edge is therefore an important consideration. The potential for resin edge failure is reduced with an alternative resin edge material and tested experimentally. Results are compared against a baseline (untreated) laminate and a laminate treated with the resin used in Chapter 4. The broader applicability of the resin edge treatment, beyond curved laminates subjected to 4-point bending, is shown by FE analysis of flat laminates subjected to axial loading, which is in line with the case presented in the literature for other edge protection techniques, discussed in Section 4.3.

5.1 Effect of Resin Treatment on Near-edge Stress

The stress field in the vicinity of the free edge is highly complex, as is the way in which the resin edge treatment interacts with it. Interlaminar stresses σ_r and τ_{lr} have been identified as critical components contributing towards failure near the free edge [49]. Comparisons between untreated and treated laminates of global interlaminar direct stress (σ_r) and interlaminar shear stress (τ_{lr}) are shown in Fig. 5.1 and Fig. 5.2 respectively. The presence of a singularity in the untreated laminate dictates that stresses in the l-direction must be zero at the free edge and other stresses become very large near the edge to compensate. The presence of the resin edge treatment allows for a non-zero stress in the l-direction at the CFRP edge, resulting in finite values for other

stresses. The effect on σ_r near the CFRP edge is shown in Fig. 5.1 for 3 different resin treatment moduli, which indicates higher modulus resin treatment suppresses σ_r further than lower modulus. The modulus of the resin used for the edge treatment is therefore important. Figure 5.1 indicates that the peak σ_r stress for the 'high modulus' resin (E = 8.5 GPa) is approximately equal to the mid-width σ_r.

Although the resin treatment suppresses σ_r stress, this is not the case for all stresses. Since the stresses in the l-direction no longer have to be zero at the CFRP edge, interlaminar shear stress, τ_{lr}, can be significant. This is shown in Fig. 5.2 for 3 different resin treatment moduli. The untreated laminate stress goes to zero at y/b = 1, with the stress in the immediate vicinity increasing with increasing resin modulus. Note however that τ_{lr} is reduced further from the CFRP edge (y/b $\lesssim$ 0.99) with increasing resin modulus. The significant reduction in σ_r and increase in τ_{lr} near the CFRP edge can cause a failure mode change for the resin treated laminates, which is why different delamination patterns are seen in Fig. 3.10, page 74 and Fig. 4.16a, page 112.

The use of edge caps [80-83] has also been shown to reduce interlaminar direct stress but not interlaminar shear stress. The caps consist of a C-shape that is clamped around the laminate at the free edge. This provides a means for development of none zero stresses normal to the free edge, where the laminate edge is in contact with the vertical section of the C-shape, similar to the effect of resin treatment in this work. Compared with the resin treatment however, edge caps are likely to provide greater support in the r-direction because of the clamping effect through thickness.

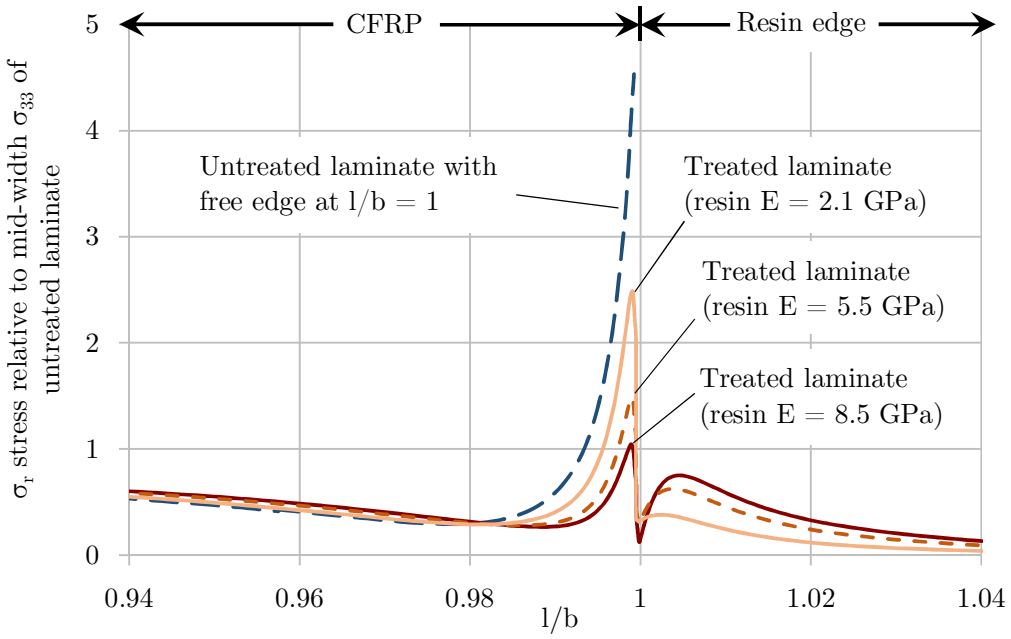

Figure 5.1 Global σ_r stress in the vicinity of the CFRP edge within interface 36 (between 0/90° plies closest to inner radius) of G39B FE model. Normalised relative to the mid-width σ_r of the untreated laminate. Curved laminate width is b.

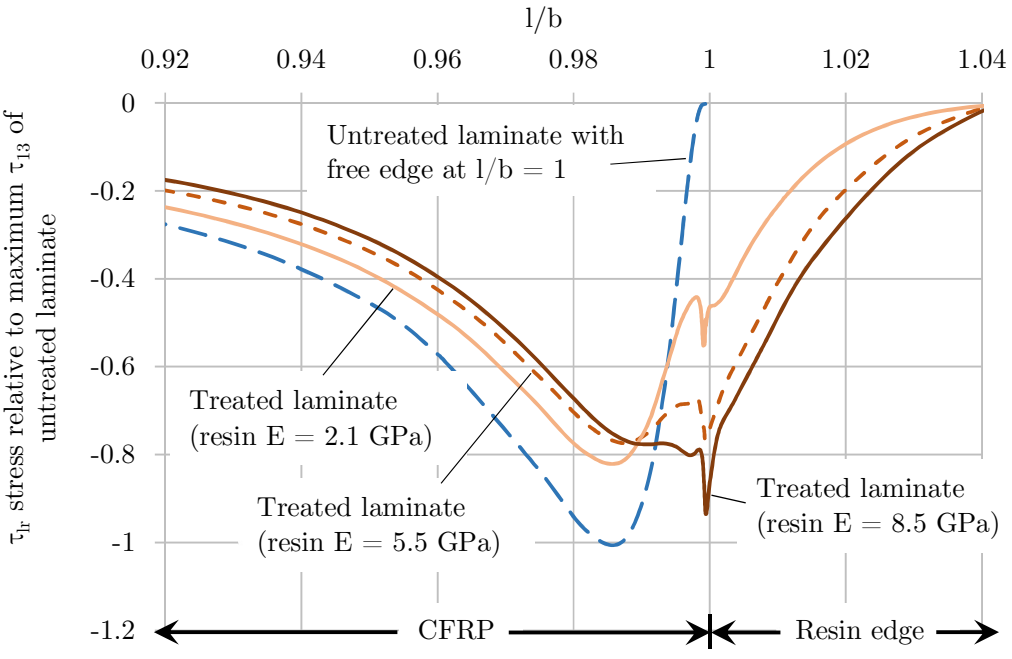

Figure 5.2 Global τ_{lr} stress in the vicinity of the CFRP edge within interface 38 (between ±45° plies closest to inner radius) of G39B FE model. Normalised relative to maximum τ_{lr} of untreated laminate. Curved laminate width is b.

5.2 Sensitivity Studies

In order to formulate the analytical and FE models, a number of assumption about the material properties and specimen geometry were made. In this section, the importance of these properties is investigated by varying their value and assessing the impact on CBS prediction. A Python script is written to rapidly adjust curved laminate properties, such as opening angle and layer thickness.

5.2.1 Thickness of Ply and Interface Layers

There is a reasonably high level of confidence in the overall thickness of fibrous ply and resin interface together since this can be calculated from the total laminate thickness and number of plies. However, the exact radio of how this thickness is distributed between ply and interface is more difficult to determine. As mentioned previously, a nominal ply/interface thickness of 0.23/0.02 mm (M21/IMA) and 0.16/0.02 mm (8552/AS4) is used for the analysis in Chapters 3 and 4. These ratios are now varied according to Table 5.1, which shows the effect on the predicted CBS according to the Camanho or Christensen failure criteria (whichever is limiting). For each laminate type, the highest CBS prediction is highlighted for clarity. The effect of the ply-interface ratio depends on the location that failure is predicted: when failure is predicted within a fibrous ply, a higher CBS is predicted when the ply is thicker; and when failure is predicted within a resin interface, a higher CBS is predicted when the interface is thicker than the baseline. In general the CBS prediction is relatively insensitive to the variations in ply-interface ratios considered, with the exception of the G39B(R) model, which shows a relatively significant reduction (6.7%) in CBS if a thicker ply/thinner interface is modelled. However, even this difference is relatively small in comparison to the reduction in interface thickness (25%) required to produce it, as compared to the baseline.

Laminate	Ply / interface thickness (mm)	Failure by	Within	Predicted CBS (kNmm/mm)	Difference (%)
G39B(R)	0.235 / 0.015	Camanho	Int.	7.86	-6.7
	0.230 / 0.020			8.42	baseline
	0.225 / 0.025			8.88	+5.5
S44(R)	0.165 / 0.015	Camanho	Ply	5.17	+1.2
	0.160 / 0.020			5.11	baseline
	0.155 / 0.025			5.05	-1.2
N44(R)	0.165 / 0.015	Christensen	Int.	3.80	-1.6
	0.160 / 0.020			3.86	baseline
	0.155 / 0.025			3.91	+1.3
S24(R)	0.165 / 0.015	Christensen	Ply	2.21	+2.3
	0.160 / 0.020			2.16	baseline
	0.155 / 0.025			2.10	-2.8
N24(R)	0.165 / 0.015	Christensen	Ply	1.92	+2.7
	0.160 / 0.020			1.87	Baseline
	0.155 / 0.025			1.82	-2.7

Table 5.1 Effect of ply/interface thickness ratio on CBS.

5.2.2 Corner Radius

The curved laminates were laid up onto a male tool during manufacture, such that the tool surface controlled the inner radius. The radius of the tool was therefore assumed for each curved laminate model. Any level of spring-in / spring-back after cure is likely to affect the inner radius. However, deviation from the nominal inner radius was smaller than was measurable for the specimens in Chapters 3 and 4. Therefore, the effect of a small variation in inner radius of ± 1 mm is considered, since anything larger than this would be readily detectable. The results from FE analysis is shown in Table 5.2. The CBS prediction is insensitive to variations in inner radius, within the range reasonably expected for the curved laminate specimens. Therefore, the CBS predictions based on nominal inner radius are valid, irrespective of small variations in radius.

Laminate	Inner Radius (mm)	Predicted CBS (kNmm/mm)	Difference (%)
G39B(R)	21	8.36	-0.7
	22	8.42	baseline
	23	8.47	+0.6

Table 5.2 Effect of curved laminate inner radius on CBS.

5.2.3 Opening Angle

The limb angle (refer to Fig. 3.3, page 69) of the specimens was measured after cure to take into account any spring-in / spring-out, and the average value is used for the nominal FE models. Nevertheless, there are small variations in opening angle between different specimens of the same type, as indicated by (Fig. 2.16, page 62). From this figure, the variation in opening angle between the greatest and smallest data point is 0.4°, equivalent to 0.2° per limb, i.e. $\alpha/2$ in Fig. 3.3. Table 5.3 shows the effect on CBS prediction with a ~10-fold greater variation in limb angle of ±2.5°. The CBS is relatively insensitive to this and the FE model with nominal limb angle is therefore valid for all specimens, irrespective of typical variations in limb angle.

Laminate	Corner angle, α (°)	Predicted CBS (kNmm/mm)	Difference (%)
G39B(R)	80	8.55	+1.5
	85	8.42	baseline
	90	8.29	-1.6

Table 5.3 Effect of corner angle on CBS.

5.3 Failure of Resin Edge

The selection of resin used for the resin edge treatment is important because the mechanical properties of the resin have a strong influence on the stress distribution in the curved laminate, as shown in Figs. 5.1 and 5.2. The level of stress generated within the resin edge is also important. At the point of failure during the experimental tests, it was observed that the resin edge shattered into many pieces and broke away from the CFRP (see Fig. 4.16b), as well as multiple delaminations appearing in the CFRP, all within a fraction of a second. If the resin edge fails, CFRP edge protection is lost and therefore the laminate is likely to fail simultaneously, if the untreated test CBS has been exceeded. It was not possible to determine exactly which failure occurred first during experimental tests.

With the average experimental CBS of 8.65 kNmm/mm applied, the G39B(R) model is interrogated to find possible failure modes of the resin edge. At the inner radius a small portion of the resin edge is stressed beyond the 55 MPa UTS [89] by σ_θ, as shown in Fig. 5.3. The maximum tensile σ_θ in the resin edge is found to be 60 MPa.

Note much of the CFRP section has a stress well beyond this, however the allowable is significantly higher in this region due to the presence of the fibre reinforcement. This would indicate failure during the test could first be initiated by failure of the resin edge treatment. Although it was difficult to determine the trigger for failure of experimental specimens, as previously mentioned the resin edge of specimen S44(R)-01 did not shatter, instead exhibiting cracks at the inner radius (see 4.15), which are consistent with failure of the resin edge by tensile σ_θ stress. Applying the average experimental CBS to the S44(R) FE model reveals that a greater portion of the resin edge is stressed beyond UTS compared with G39B(R), as shown in Fig. 5.4. In general it is found that the more compliant the curved laminate, the greater the maximum σ_θ in the resin edge, driven by the larger deflection-to-failure.

In Table 4.5 the CBS predictions considered failure of the central CFRP section only. It was observed during the experimental testing that there were very low level audible emissions that began part way through the loading of all resin treated specimens, becoming more frequent up to the point of failure. However, there was no traceable load drop co-incident with these emissions. The earliest emissions occurred approximately at the point at which the σ_θ stress in the resin edge reaches yield according to the FE analysis. It is likely that as load is increased during the test, the resin begins to yield and carry less stress than that predicted by linear FE analysis. The resin also visibly de-bonded from the limbs of the curved laminates during testing of the thinner, 24-ply specimens. This would also alleviate stress in the resin edge, which would have the effect of delaying failure.

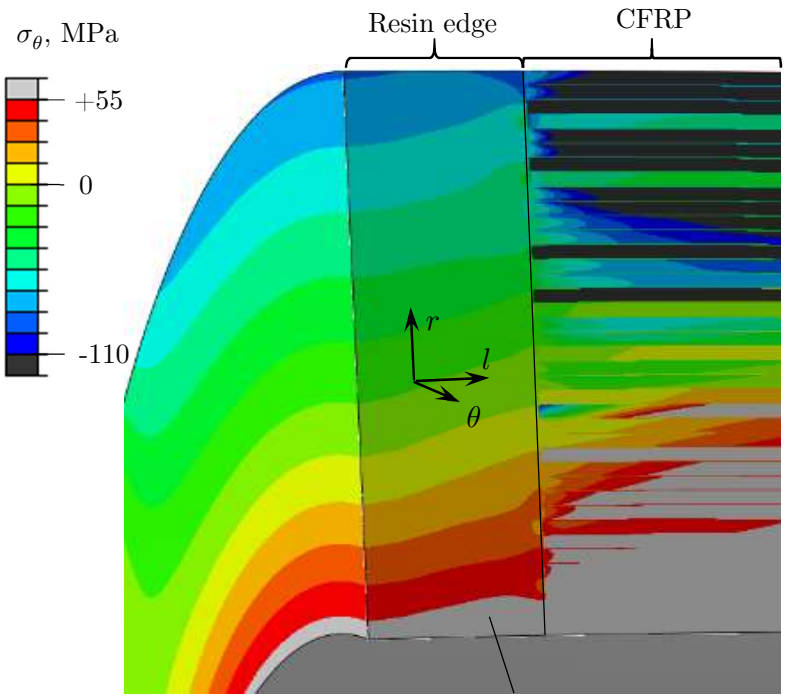

Figure 5.3 G39B(R) FE model sectioned at apex, showing σ_θ contours with 8.65 kNmm/mm applied. The contour scale limits are the ultimate tensile and compressive strength of the EP1330LV resin edge material.

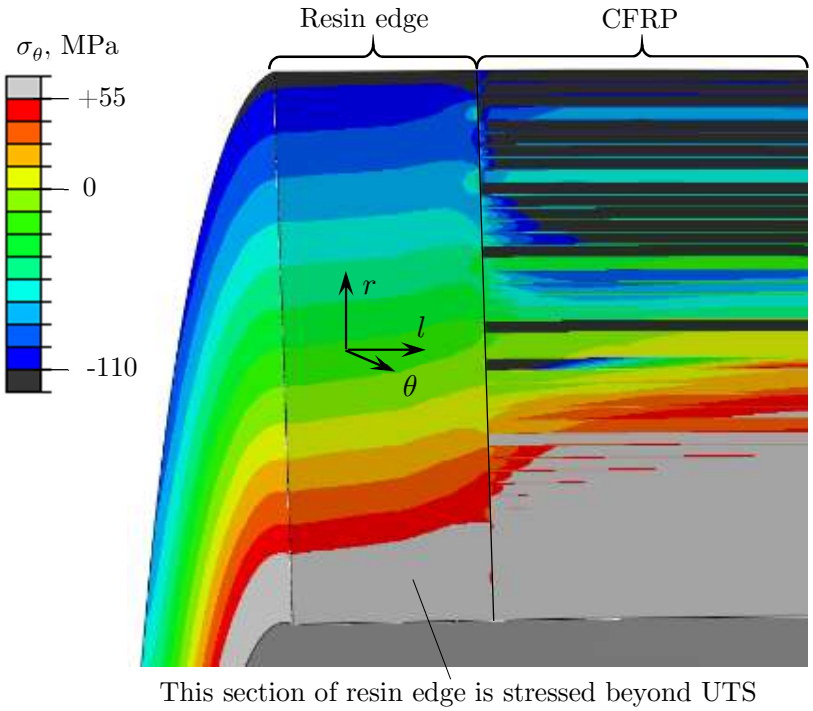

Figure 5.4 S44(R) FE model sectioned at apex, showing σ_θ contours with 5.23 kNmm/mm applied. The contour scale limits are the ultimate tensile and compressive strength of the EP1330LV resin edge material.

5.4 Alternative Resin Edge Material

The effect of using a different material for the resin edge treatment is explored. The aim is to alleviate stress in the resin edge and minimise the chance of failure first occurring in this region. For this investigation, industrially manufactured curved laminate specimens are used, with key dimensions shown in Table 5.4. Code named G64; they consist of 64 plies (0°, 90° and ±45°) in a typical balanced, symmetric stacking sequence:

$[\pm 45/90/0/\pm 45/(\pm 45/90/0)_4/\pm 45/(\pm 45/90/0)_2]$s.

The laminate material, M21/IMA, is assumed to have the properties as per Table 4.4. Two alternative materials are used for the resin edge treatment: the resin system EP1330LV, which is used in Chapter 4 and has a relatively high modulus of 8.9 GPa and UTS of 55 MPa; and EP950G, which has a lower modulus of 3.8 GPa but a higher UTS of 66 MPa [102]. Compared with EP1330LV, as well as attracting less stress due to the lower modulus, the higher strength is thought to significantly reduce the likelihood of resin edge failure during corner unfolding (prior to laminate failure).

ID	Resin/fibre material	Cured ply thickness (mm)	No. plies	R_{inner} (mm)	α (°)	Width (mm)
G64	M21/IMA	0.25	64	29	88.6	52

Table 5.4 G64 specimen nominal dimensions.

5.4.1 FE Modelling Predictions

The effect of varying resin edge modulus is analysed using the FE models and failure criteria as per Section 4.5.3. Figure 5.5 shows the Camanho failure criterion with 15.2 kNmm/mm running moment applied to the FE models: one with EP950G resin edge modulus and one with EP1330LV. As expected, the lower resin modulus provides less support to the CFRP edge and this generally results in higher failure criterion values, and hence lower predicted CBS. However, it is noted that the effect is different for different stress components: the direct stress σ_{33} is the dominant stress at peak failure index (at ply 61) for the 3.8 GPa resin, and this stress component is strongly suppressed by higher resin modulus; whereas the interlaminar shear stresses τ_{13} and τ_{23} are less strongly influenced by resin modulus, being the dominant stresses at peak failure index

for the 8.9 GPa resin. Figure 5.6 shows the Christensen fibre failure criterion with the same applied running moment for the two resin edge moduli. The Christensen failure index appears significantly less affected by resin modulus than the Camanho index, because the stress in the global θ-direction (parallel to the CFRP edge) is less significantly affected by resin edge modulus than through-thickness stress components and those normal to the CFRP edge. Note that stress is decreased in the global l-direction with lower resin edge modulus since less stress can be supported normal to the CFRP edge. This is evident by the reduced Christensen failure index for the 3.8 GPa resin modulus in 0° plies, for example ply 4 in Fig. 5.6. This is not the case for all 90° plies (for example ply 3), since the fibres in these plies are aligned in the global θ-direction. Interestingly the 3.8 GPa resin appears to increase Christensen failure index for the 90° plies in compression and reduce that for those in tension. Applying Christensen matrix failure criterion between the mid-thickness 0° ply pair (interface 32) gives a failure index of 0.168 for the 3.8 GPa resin and 0.166 for the 8.9 GPa resin. This is therefore not significantly affected by resin edge modulus, and since the index is well below 1, failure is not predicted by this mode.

Failure of the G64 laminate with 3.8 GPa modulus resin edge treatment is predicted to be 15.2 kNmm/mm from Fig. 5.5. With a resin modulus of 8.9 GPa, failure is predicted to occur by Christensen failure criterion, shown in Fig. 5.6, at 22.7 kNmm/mm. However, analysing the mid-width stresses, failure is predicted to occur at 20.6 kNmm/mm by Camanho failure criterion, shown in Fig. 5.7a. Note that this is completely dominated by σ_{33} (Fig. 5.7b), since τ_{13} and τ_{23} are negligible at the mid-width. In other words, the 8.9 GPa resin completely mitigates the edge effect for the G64 laminates, since failure is predicted at the mid-width before the edge. The predicted CBS based on failure of the laminate is summarised in Table 5.5.

Although CBS based on laminate failure is reduced with the lower resin edge modulus; the key benefit of the lower modulus is that it reduces the stress in the resin edge treatment. With an applied running moment of 13 kNmm/mm, the σ_θ stress in the resin edge is shown in Fig. 5.8 for the 8.9 GPa modulus resin. A localised region is predicted to be stressed beyond the 55 MPa UTS. This is primarily caused by the corner unfolding, with some interaction with the CFRP laminate causing a localised increase in stress near the CFRP edge-resin edge boundary. Figure 5.9 shows the equivalent for the 3.8 GPa modulus resin edge; however, a significantly higher running moment of 30 kNmm/mm is applied in order to generate the same localised region of stress beyond UTS. This is primarily because the lower modulus attracts less stress

but is also partly because the UTS is slightly higher at 66 MPa. Assuming these localised regions of stress would cause failure, the resulting predicted CBS based on failure of the resin edge is summarised in Table 5.5. However, it is important to consider that this is based on a highly localised area of stress. Since this is from linear FE analysis, it does not account for reduction in resin modulus with increasing stress or allow for localised yielding of material and redistribution of stress. Nor does it take account of whether failure of the resin edge in a given location is critical to protection of the CFRP edge. It has also been shown previously in Fig. 5.3 and Fig. 5.4 that the stress goes beyond UTS in a large portion of resin edge at average test CBS according to the FE analysis. Therefore, the predicted CBS based on resin failure is highly conservative, in particular for EP1330LV. However, it provides an indication of the variation between resins of different mechanical properties.

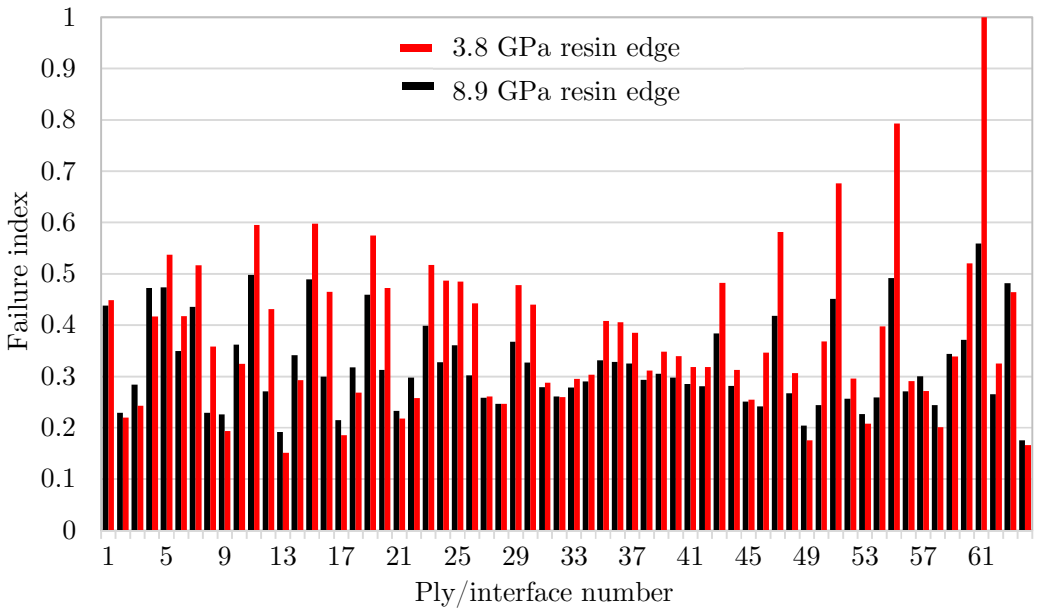

Figure 5.5 Camanho failure criterion through thickness of G64 FE model near CFRP edge-resin treatment boundary with 15.2 kNmm/mm applied running moment. The influence of varying the resin edge treatment modulus is shown by using the properties of EP950G and EP1330LV.

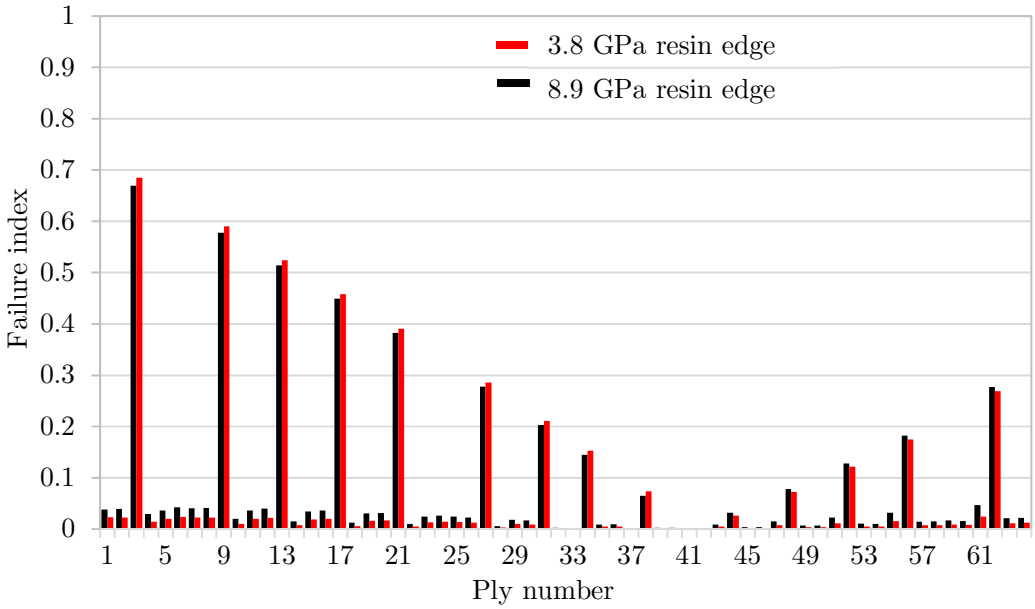

Figure 5.6 Christensen fibre failure criterion through thickness of G64 FE model near CFRP edge-resin treatment boundary with 15.2 kNmm/mm applied running moment. The influence of varying the resin edge treatment modulus is shown by using the properties of EP950G and EP1330LV.

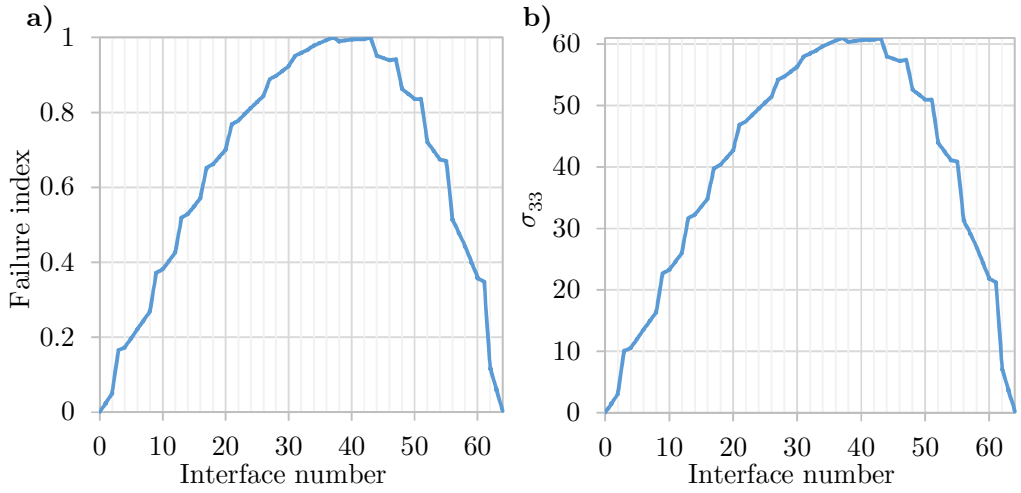

Figure 5.7 From mid-width/apex of G64 model with 8.9 GPa modulus resin edge and 20.6 kNmm/mm applied running moment. **a)** Camanho failure criterion. **b)** σ_{33} stress component.

Resin	Modulus (GPa)	UTS (MPa)	CBS (kNmm/mm)	
			Laminate failure	Resin edge failure*
EP1330LV	8.9	55	20.6	13
EP950G	3.8	66	15.2	30

*highly conservative

Table 5.5 CBS predictions from FE models with different resin edge properties. Failure of the laminate is assessed using Camanho failure criterion as previously. Failure of the resin edge is predicted when the UTS is reached.

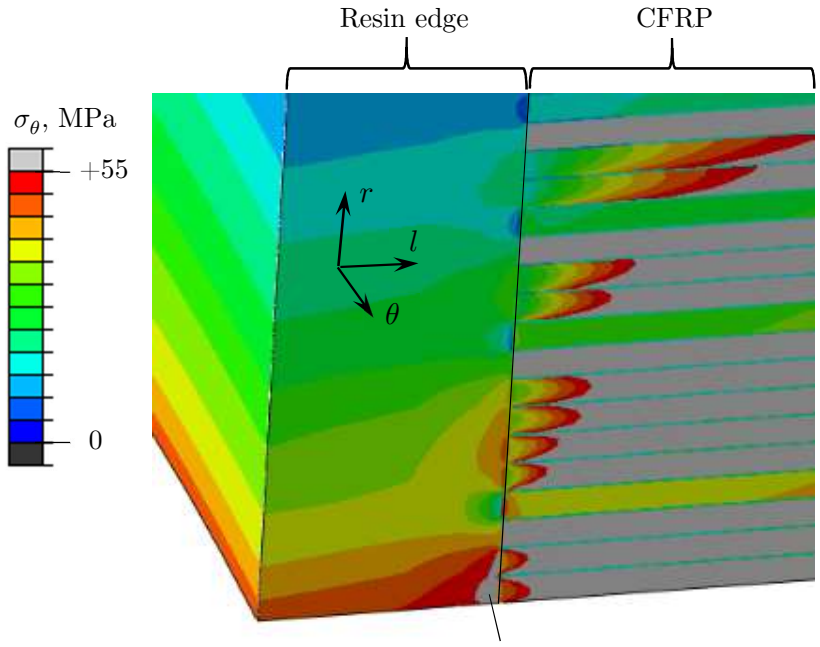

Figure 5.8 FE model of G64 curved laminate with 8.9 GPa modulus resin edge (EP1330LV). Sectioned at apex showing σ_θ stress near the inner radius. 13 kNmm/mm running moment applied.

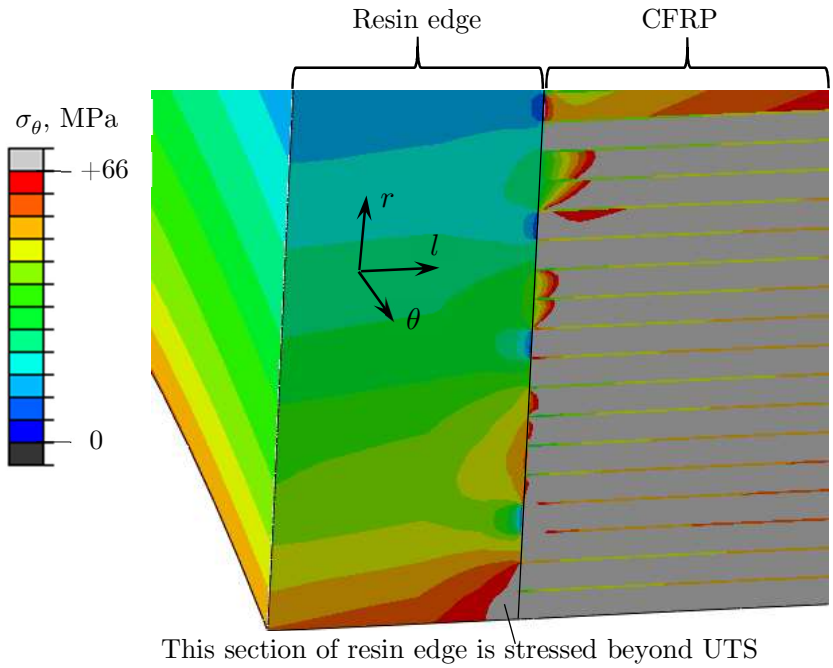

Figure 5.9 FE model of G64 curved laminate with 3.8 GPa modulus resin edge (EP950G). Sectioned at apex showing σ_θ stress near the inner radius. 30 kNmm/mm running moment applied.

5.4.2 Experimental Testing and Results

The G64 specimens were subjected to a 4-point bending test: 3 without resin edge treatment, 3 treated with EP1330LV and 3 treated with EP950G. Accommodating the larger specimens required an alternative test rig from that used previously. The clearance afforded by the roller housing severely limited the amount of resin that could be applied to the free edge of the specimens. Instead of the previously tested 3 mm width-wise resin edge, only approximately 1.5 mm was applied. The treatment could not extend down the specimen limbs beyond the contact point with the upper rollers. Instead it terminated at the junction between the curved section and limb. An illustration of the different resin edge geometry is shown in Fig. 5.10.

The test results are shown in Fig. 5.11, with averages summarised and compared in Table 5.6 for the different resin edge materials. The EP1330LV resin shows a marginal increase in CBS over the untreated specimens, which is relatively insignificant in comparison to the standard deviation for the test results. This is possibly due in part to the limitation on the extent of the resin treatment (Fig. 5.10). Even despite this limitation however, the EP950G resin does show a significant improvement over the untreated specimens. As with previous tests, the EP1330LV resin edge shattered

into many pieces and broke away from the CFRP edge at the point of failure. In contrast, the EP950G remained attached to the CFRP edge. This indicates that a change in failure mode occurred and it is likely the resin edge was not the point of first failure for the EP950G specimens. Comparing the experimental results with the FE predictions from Table 5.5, the EP950G CBS prediction is conservative on the order of 6.7% by laminate failure. Failure of the resin edge is predicted to be the limiting factor for EP1330LV specimens, which was likely the case experimentally; however, the prediction is highly conservative by approximately 14%. As mentioned previously this is expected since the prediction is based upon a highly localised region of stress that is unlikely to cause immediate failure.

Overall it is shown that the mechanical properties of the resin edge material are important and can influence the failure mode of specimens. There is potential for improving the CFRP free edge protection by selecting a resin edge with high strength; and a modulus that is a compromise between minimising the edge effect and limiting the stress attracted by the resin edge. The limitation on resin edge geometry prevents full assessment of the extent of this potential at this stage.

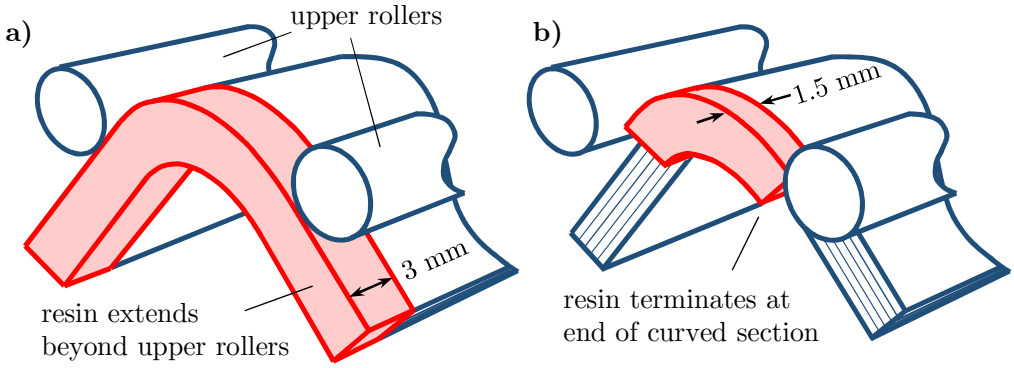

Figure 5.10 Comparison of resin edge geometry. **a)** As per previous specimens. **b)** As per G64 specimens for alternative resin edge study.

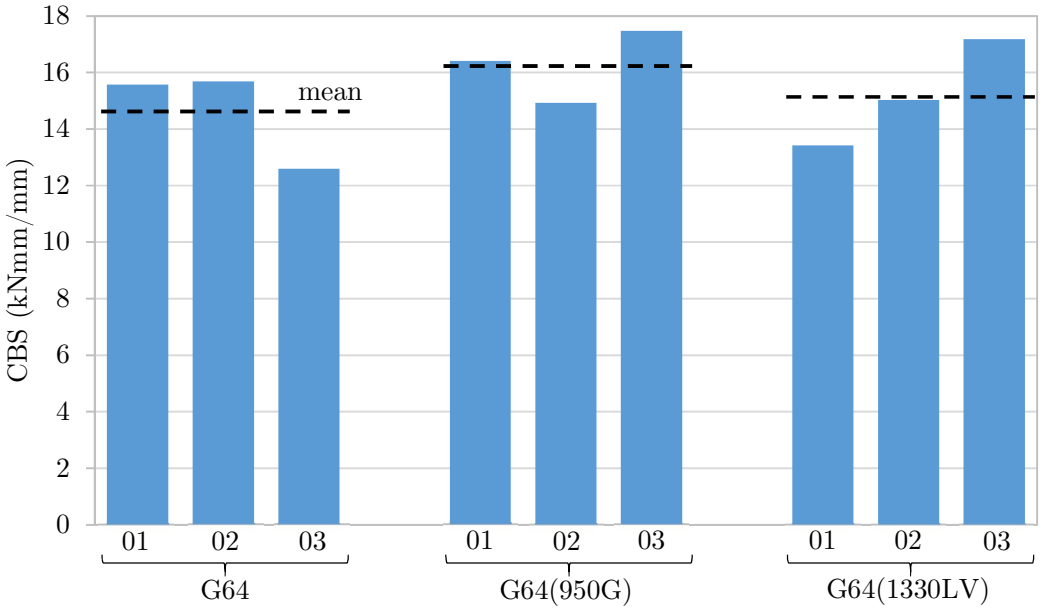

Figure 5.11 G64 specimen test results without resin edge treatment and with two alternative resin edge materials: EP950G and EP1330LV.

Resin edge	(kNmm/mm)		CBS Diff. (%)
	CBS	S.D.	
None	14.6	1.43	baseline
EP1330LV	15.2	1.54	+4.1
EP950G	16.3	1.04	+11.6

Table 5.6 CBS for G64 specimens with different resin edge treatment material. Each result is the average of 3 specimens.

5.5 Flat Laminates

In Chapter 4 the resin edge treatment is developed for curved laminates. The effect on flat laminates is explored in this section via FE models, to show that the treatment can be applied more generally to the free edge of different shaped laminates.

The geometry of the flat laminate models is shown in Fig. 5.12. The principal loading direction for tension and compression due to bending of the curved laminates is the θ-direction in previous chapters. This is the fibre direction of 90° plies. For consistency, the principal loading of flat laminates is in the 90° fibre direction, which is termed the global y-direction. The assumed material properties are that of M21/IMA

considered previously in terms of mechanical behaviour (Table 4.4) and ply/interface thickness (0.23/0.02 mm). Laminates with and without resin treatment applied to the free edges are subjected to identical loading.

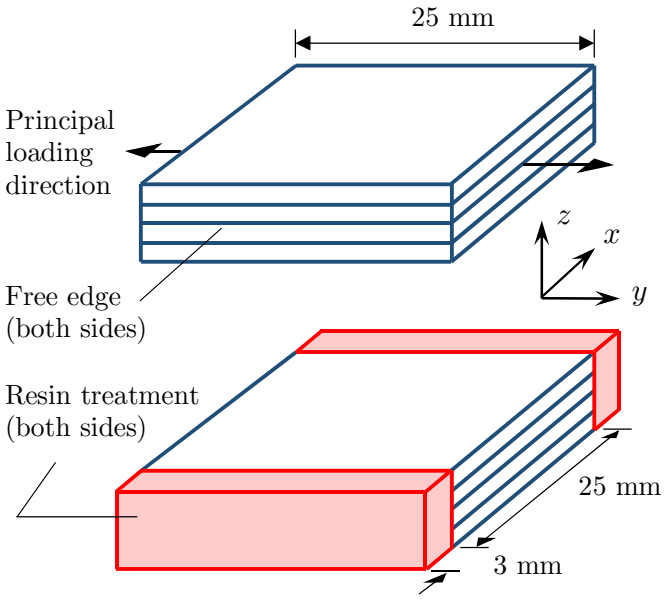

Figure 5.12 Flat laminate model geometry without (top) and with (bottom) resin edge treatment. Note the principal loading is in the y-direction for consistency with previous models.

5.5.1 Shear Mismatch

From classical laminate theory, the $\bar{Q}_{16}$ and $\bar{Q}_{26}$ terms, which couple extension and shear, are equal and opposite in sign for positive and negative angle plies (as discussed in Section 2.1.2). A four ply flat laminate $[\pm 45]_S$ is used to generate a shear mismatch between adjacent plies when subject to axial load. In Section 4.2.1 this is shown to generate in-plane shear $\tau_{l\theta}$ (τ_{xy}) towards the mid-width of the laminates. At the free edge however, this goes to zero and instead interlaminar shear $\tau_{\theta r}$ (τ_{yz}) is generated as explained in Section 4.2.2. The same stress system is found for flat laminates without resin treatment, as shown in Fig. 5.13. Although for treated laminates τ_{xy} still reduces towards the edge, since the stiffness of the resin edge is much less than the fibre reinforced laminate; the addition of the resin edge removes the requirement for stresses in the x-direction to become zero at the CFRP edge (x/b = 1). The benefit of this is that interlaminar shear τ_{yz} is reduced in the vicinity of the CFRP edge, as shown in Fig. 5.13. This reduces stress in the weaker interface layers, which bond the stronger plies together, delaying initiation of delamination by Mode III fracture.

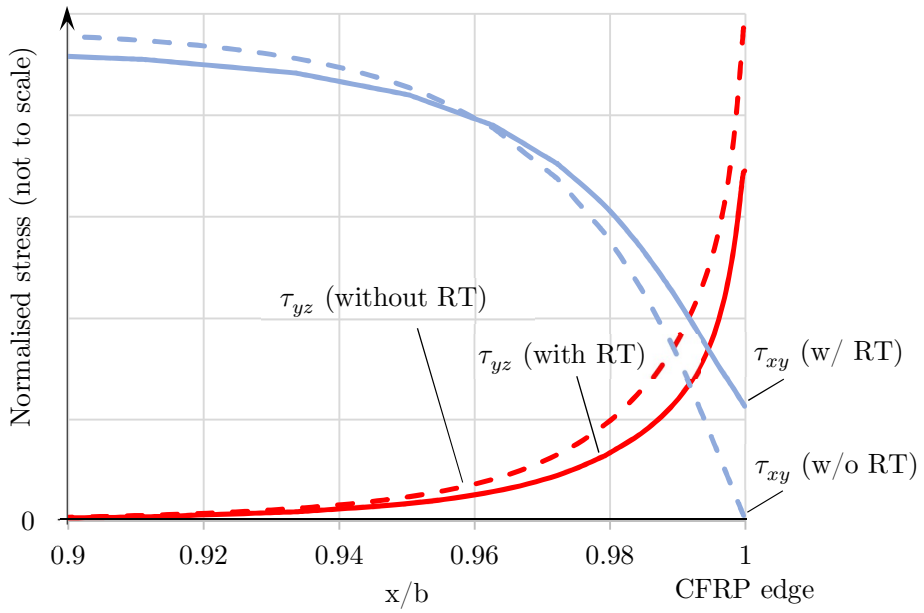

Figure 5.13 Effect of resin treatment (RT) on near-edge stress components in vicinity of ±45° pair. In-plane shear does not go to zero at the CFRP edge and interlaminar shear is reduced with the introduction of a resin edge.

5.5.2 Poisson's Ratio Mismatch

A four ply flat laminate $[0/90]_S$ is used to generate a Possion's ratio mismatch between adjacent plies when subject to axial load. As discussed in Sections 4.2.1 and 4.2.2, this is found to generate interlaminar direct stress σ_z, meanwhile stresses in the x-direction (σ_x and τ_{xz}) must become zero at the CFRP edge. The same behaviour is found for flat laminates without resin edge treatment, as shown in Fig. 5.14. The addition of resin edge treatment enables significantly more transverse stress σ_x to be carried in the vicinity of the CFRP edge. Interlaminar shear τ_{xz} in the interface later is increased and no longer must become zero at the CFRP edge. This has the potential to initiate delamination by Mode II fracture. Interlaminar direct stress σ_z in the vicinity of the edge is greatly reduced however, suppressing the potential for delamination initiation by Mode I fracture, which is known to be a common cause of composite laminate failure.

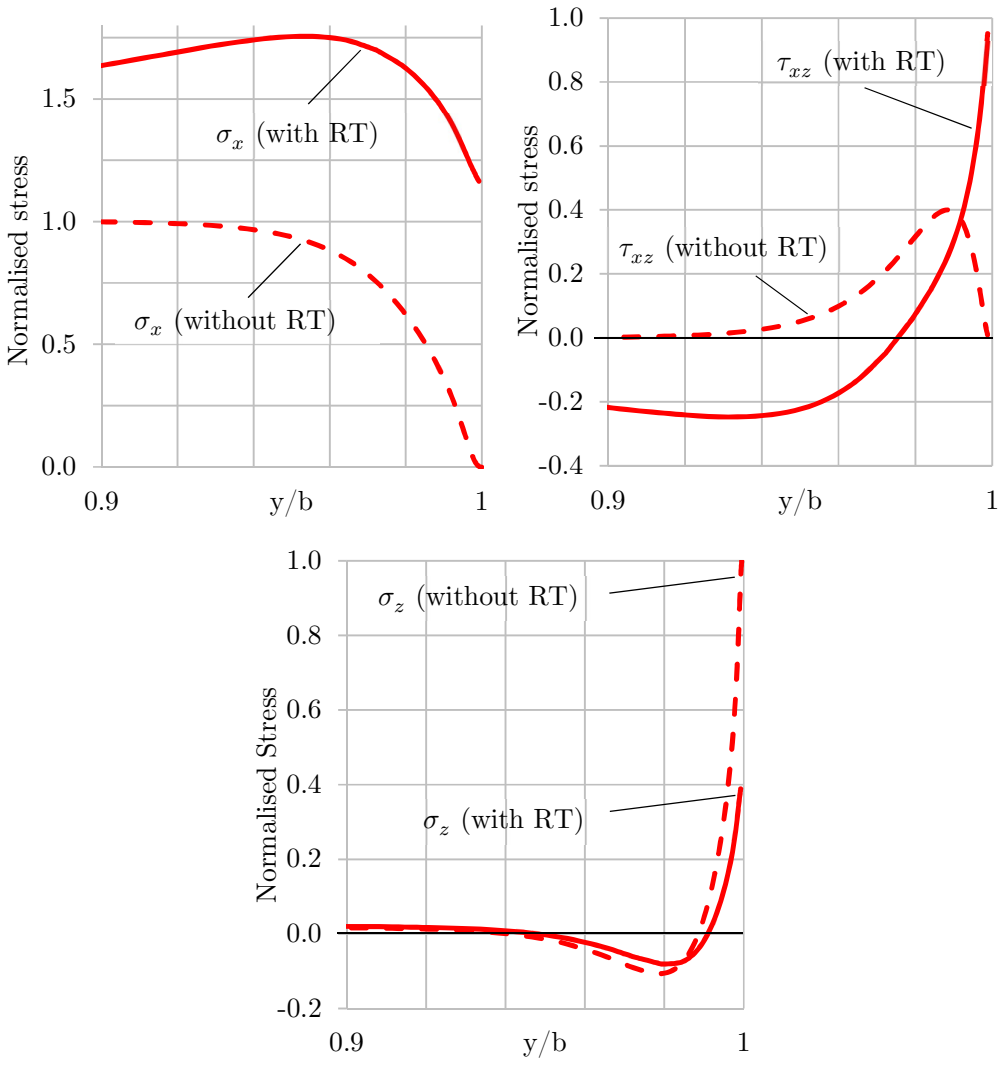

Figure 5.14 Effect of resin treatment (RT) on near-edge stress components in vicinity of 0°/90° pair. Stress components in the x-direction do not go to zero at the CFRP edge and through-thickness direct stress is reduced with the introduction of a resin edge.

5.6 Closing Remarks

The resin edge treatment is found to reduce σ_r (σ_z) at the CFRP laminate edge, with a greater reduction for increasing resin modulus. The treatment increases τ_{lr} (τ_{xz}), since this does not have to decay to zero at the laminate edge as it does for a free edge (without treatment). The FE model is found to be relatively insensitive to specimen geometry and so small variations in corner radius and opening angle are unlikely to have any significant effect on the results. The interface thickness is most important

when failure is predicted by delamination of the interface. As shown in Fig 3.19 and Fig. 3.20, page 85, there is significant variation in the interface thickness of typical laminates and so the potential to cause significant variability in strength.

An alternative resin edge treatment material (EP950G) is modelled and tested experimentally. The reduced modulus and increased strength is found to prevent initial failure in the resin edge, instead initiating in the CFRP laminate. This increases CBS compared against both untreated laminates and those treated with a higher modulus, lower strength resin. The lower modulus resin also improves the repeatability of the test results.

6 DISCUSSION

Many aspects of composite laminates have been considered, including design, manufacture, certification, experimentation, numerical modelling and analytical analysis. All these aspects have been required to understand the behaviour of novel stacking sequences in a broad sense. The comparison between novel stacking sequences and more typical balanced, symmetric ones is a common theme running through the thesis.

The stacking sequence has been shown to have an important impact on the behaviour of a laminate during manufacture; a significant reduction in warpage is possible. Though the **B** (coupling) matrix terms from classical laminate theory, linking in-plane and out-of-plane deflections, are generally considered most important for warpage, this is primarily true of flat laminates. Laminates with complex geometry, such as curvature and taper, can still exhibit warpage with a null **B** matrix. This is shown in Chapter 2 for the balanced, symmetric demonstrator laminate, which has a null **B** matrix by virtue of symmetry, yet exhibits a significant amount of spring-in and twist. This is primarily driven by the curved sections of the laminate, which cause a shift in the neutral plane away from the mid-thickness of the laminate, towards the inner radius. This effect is also evident from the FE analysis when the curved laminates are subjected to corner unfolding, highlighted for example by Fig. 4.32b, page 127. Since the spring-in causes bending of the laminate, bend-twist coupling can in turn lead to twisting. Bend-twist coupling is not removed by virtue of symmetry but is removed by anti-symmetry. The novel, anti-symmetric laminate demonstrates that this type of laminate can be manufactured using typical industrial processes, such as AFP layup and autoclave cure, without producing undesirable effects. Moreover, by tailoring the stacking sequence, less warpage is produced, in the form of spring-in and twist, as compared against the baseline balanced, symmetric demonstrator. The requirement for a symmetric laminate that is fully uncoupled is also shown to severely limit the design space: there are typically more than an order of magnitude more fully uncoupled anti-symmetric laminates (Table 2.5 and Table 2.6, page 43). The increased design space

becomes important when there is a requirement for stacking sequences to conform to particular criteria, such as the design of a protected zone, which is shown to improve consolidation in Chapter 2.

The stacking sequence is also important to the performance of laminates as well as manufacture. The sequence must be designed such that sufficient bending stiffness is produced (D_{11} and D_{22} terms). Again, the increased number of fully uncoupled anti-symmetric laminates offers greater flexibility when designing a laminates stiffness properties. The performance of narrow specimens is typically limited by the free edge effect, which initiates failure. The stacking sequence is important in controlling this, since the effect is driven primarily by the mismatch in mechanical properties between adjacent layers with fibres in different orientations. For example, as shown in Fig. 4.4, page 103 and discussed in Section 4.2.2, the mismatch in Poisson's ratio between a $0/90^\circ$ pair of plies generates interlaminar stress σ_{33} near the free edge. From analysis in Section 4.2.2 and as also shown by [78], switching around a 0° and 90° ply can change the σ_{33} stress generated from tensile to compressive. In turn, compressive σ_{33} is less likely to promote delamination at the interface joining the two plies.

The free edge effect causes narrow witness specimens, cut from production parts for certification purposes, to under represent the true strength of the full-size part. To mitigate this, a resin edge treatment has been developed. This is bonded onto the free edge, which is therefore no longer free, and allows stresses normal to this edge surface. A key benefit of this edge treatment over other methods for mitigating the edge effect, is that it can be retrospectively applied to witness specimens once they are cut from the production part; the production part does not need to be adapted or specially designed in any way that might affect its in-service performance. This treatment is shown to improve the strength of laminates with different dimensions, material properties and stacking sequences (Table 4.1, page 108 and Table 5.6, page 154). The G39B(R) specimens are a 52 mm wide CFRP section, with 3 mm resin applied either side, giving a total width of 58 mm (or an extra 11.5%). However, the average unfolding moment at failure is increased by 15.6%, compared with the untreated G39B specimens. In other words, the 52 mm wide specimen with resin treatment is stronger than would be expected even for a 58 mm wide specimen (all CFRP). This indicates the significance of the edge effect, and the effectiveness of the treatment. By removing or significantly reducing the tendency of a laminated specimen to fail from the free edge, it becomes more representative of the full-size part, which improves certification. It also makes it possible to analyse defects near the specimen mid-width, since failure is no longer

dominated by the free edge. As well as improving the performance of physical test specimens, the resin treatment enables the use of linear FEA to predict laminate strength. A combination of Camanho and Christensen failure criteria are found to give conservative predictions, typically within 2-6% of experimental CBS of curved laminates (Table 4.5, page 131). It is noted that failure during the test due to the loading from the rollers is possible, and the cracks in Fig. 4.15, page 111 would be consistent with this type of failure. This is not predicted by the FE model, which does not include the rollers with contact analysis. If the test is consistently causing failure due to the rollers, then it is not representative of the aircraft loading and hence modelling of this type of failure is not deemed as important as failure in the curved section due to the unfolding moment.

It is found that the balanced, symmetric specimens are generally stronger than those with a novel, anti-symmetric stacking sequence, in particular the S44(R) specimens are significantly stronger than N44(R). The N44(R) specimens consistently fail where there is a pair of 0° plies at interface 34. From Fig. 4.28a, page 123, there is a significant amount of through thickness tensile stress over a wide area, including ply 34, interface 34 and ply 35. This represents a significant amount of energy available to propagate a crack. In contrast, although the highest peak for S44(R) is higher (at ply 41), the area under this peak is smaller than for ply 34-35 in N44(R), representing less energy. Although standard design rules allow for up to 4 plies of the same fibre orientation to be positioned adjacent to one another, this result indicates that positioning even just 2 identical plies together can result in a significant reduction in strength. The novel laminate design could therefore be improved by separating all pairs of 0° plies. There is a trade-off however, since this will reduce the interleaving of continuous and discontinuous plies in the tapered region of a laminate in accordance with maintaining a protected zone. Therefore, a study of the strength of tapered regions would be recommended to determine the importance of interleaving, and whether it should take precedence over removing pairs of 0° plies.

Another important factor for certification besides average strength is the scatter of results. Since material properties are statistical by nature, industry typically works to an FAA tolerance based method for determining material allowables, such as A-basis and B-basis [103]: A-basis (also known as T99) is used where single point failure would result in catastrophic failure, with no redundancy, and requires that 99% of the population meet or exceed a strength with 95% confidence; B-basis (also known as T90) is used where there are multiple load paths providing structural redundancy, and

requires that 90% of the population meet or exceed a strength with 95% confidence [104]. The more scattered the test data, the longer the tails of the population distribution, reducing A- and B-basis. The resin treatment is generally found to reduce the scatter of experimental results compared with untreated specimens, which is therefore beneficial. For the G64 specimens, two alternative resin edge materials are tested. In this case the lower modulus, higher strength EP950G resin increases CBS more than EP1330LV. This is thought to be because EP1330LV fails first, initiating failure of the laminate once protection is lost, whereas EP950G attracts less stress and is stronger so failure is initiated within the laminate. EP950G also results in significantly less scatter than EP1330LV, again beneficial when using A- or B-basis.

In general, the higher the modulus of the resin, the higher the level of protection of the laminate edge (at the expense of higher stress in the resin), and the higher the strength of the resin, the less likely the resin is to fail prior to laminate failure. Therefore, the ideal resin material for the edge treatment is both high strength and high modulus. However, in practice the strength of the resin is limited and so there is an optimum modulus: as high as possible to protect the laminate, without being so high as to promote early failure of the resin edge. The ideal would be for failure of the laminate and resin edge to be coincident.

In this thesis, failure of the resin edge is considered using a maximum stress criterion. A full 3D criterion, such as [105], could be used to predict the failure of the resin under more general loading cases. However, the corner unfolding considered in this thesis results in the tangential stress (σ_θ) dominating, such that the maximum stress criterion gives approximately the same result. The resin is modelled with linear elastic behaviour. In reality the stiffness is non-linear, particularly in shear at high stress. Since the reduction in modulus at high shear stress is not modelled in the FEA, this results in an over-prediction of stress in the resin edge, and hence a conservative prediction for strength based on failure of the resin edge. As the resin edge loses stiffness, more load must be taken up in the CFRP laminate and hence the FE model under-predicts the stress in the laminate. However, since the stiffness of the resin edge is very low compared with the laminate, the stress increase in the laminate will be relatively small, and the FE model is therefore only slightly unconservative when predicting strength based on failure of the laminate.

The in-situ strength of laminate material takes account of ply thickness. It has been observed that thin plies exhibit a higher strength than thicker plies of the same fibre-resin system [106,107]. In general, strength reduces with increasing thickness up

to a point, beyond which the strength plateaus and further increases in ply thickness do not reduce strength. To test the in situ strength plies are commonly stacked together to simulate a thick ply [107] and this has been shown to reduce in situ strength. This is not considered in this thesis but similarities could be drawn against the stacking of two 0° plies in the N24 and N44 samples and how that appears to reduce specimen strength.

Residual stresses are typically generated as composite laminates cure at elevated temperature and then cool. This locks in some thermal stress before any mechanically induced stresses are applied during testing, such as the 4-point bend testing conducted in this work. This effect has been studied specifically for curved laminates [68]. This study shows that residual stress σ_r up to 5 MPa is generated for an r/t ratio of approximately 1, where r is corner radius and t is laminate thickness. However, it is also shown that this residual stress reduces significantly with increasing r/t ratio. For the curved laminates considered in this thesis r/t ranges from 2-7, such that a residual stress σ_r significantly less the 5 MPa can be expected. Since mechanical σ_r tends to dominate failure during testing, residual stress is not considered. However, other components of residual stress can be more significant and could potentially be important for predicting certain failure modes accurately.

7 CONCLUSION

This thesis explores the manufacture and certification of composite laminates. The aerospace industry is using composite materials more extensively with each new generation of aircraft, owing to their high in-plane strength and stiffness to weight-ratio, and reduced waste material during manufacture. For smaller, short-range airliners, the high production volumes demand a high-rate, high-efficiency production process. Improving the consistency of the certification process minimises concessions and the associated production delay and cost.

The stacking sequence is shown to have an important influence on the behaviour of a laminate during manufacture. Equations are derived to efficiently describe the conditions that must be satisfied to achieve a fully uncoupled sequence. These are used by an efficient MATLAB script, which does not require calculation of the full laminate stiffness matrix, and enables solutions for large stacking sequences to be found. A C-section laminate with a novel, anti-symmetric layup is designed and manufactured, which simultaneously removes all coupling terms and positions continuous plies (with fibres running the length of the part) in a protected zone, which remains equidistant from the tool surface. As compared against a balanced, symmetric demonstrator laminate, the novel demonstrator increases consolidation by 8.7% and achieves a cured ply thickness closer to the nominal value quoted by the manufacturer. Not only is it shown that the anti-symmetric layup can be industrially manufactured successfully, but compared with the symmetric design, warpage is significantly reduced: spring-in at web-flange corners by 7.8% and twisting along the web by 48%. Key to this success is the fact that anti-symmetric sequences are significantly easier to fully uncouple than symmetric ones.

Curved laminate specimens are extracted from the C-section demonstrator laminates. When subjected to corner unfolding by a 4-point bending test, the novel laminates are found to fail at lower CBS than the baseline (balanced, symmetric) laminate of equal ply numbers. The 90° plies have fibres going around the corner and hence carry most of the stress due to the unfolding moment. For the novel 24-ply

specimens, the outer-most 90° ply is found to carry greater compressive stress for a given moment, since the neutral plane is closer to the inner radius, as compared with the baseline 24-ply specimens. In turn this causes failure at lower CBS. The pairs of 0° plies closest to the inner radius of the novel 44-ply laminates are found to generate increased interlaminar tension σ_{33} in the resin interface layer between them and failure is seen in this location. This is interesting because well-known guidelines state that no more than 3 plies of the same fibre orientation may be positioned adjacent to one another within a layup to minimise interlaminar stress. The novel 44-ply laminates contain only 2 identical plies together but this appears to reduce strength of curved laminate specimens by 11-25%.

The free edge of specimens is found to cause failure at significantly lower CBS than the plane strain prediction, making closed-form 2D analytical analysis unsuitable and causing a singularity at the edge, which makes numerical modelling challenging. This is overcome with the development of a resin edge treatment, whereby a small band of resin is bonded to the free edge. This is suitable for industrial certification processes, since the resin can be applied retrospectively once a witness specimen is cut from a production part. The treatment is found to increase the CBS of curved laminate specimens by as much as 22%, compared against the equivalent untreated specimens. Treated specimens are therefore a better representation of the strength of the full-size laminate, which is very wide and commonly build into surrounding structure at its ends, such that there is no free edge.

As well as increasing the average CBS, the resin edge treatment is found to produce more consistent results, with lower standard deviation. This is beneficial since industrial certification typically involves use of A- and B-basis, where 99% and 90% of the population, respectively, are required to achieve or exceed a certain strength. When fitting test data to a distribution, increased scatter tends to reduce the strength prediction for the bottom 1-10% of the population.

Accurate prediction of resin treated curved laminate CBS is achieved by modelling a finite-thickness resin interface layer between each ply, taken from micrograph images, and applying a combination of Camanho and Christensen failure criteria. This produces a conservative prediction, typically within 2-6% of average test failure. Without modelling the interface layer with a finite-thickness and 6 elements through thickness, the interlaminar normal stress between the pairs of 0° plies in the novel 44-ply laminate would not be properly captured.

The resin treatment is having a significant industrial impact, by reducing time and cost associated with certification: *"GKN will benefit from reduction in concessions* [and] *in the value of assets to be sacrificed for future test programmes"* [4].

7.1 Future Work

In this thesis, a resin edge treatment to aid certification of composite laminates has been discussed. This has been developed sufficiently that it can be used to protect the free edges of narrow witness specimens, yielding a significant improvement in strength, which is a better representation of the full-size component. However, the nature of research and development means that there are several interesting topics resulting from this work. In this section, potential avenues for further understanding and developing the resin edge treatment are briefly described. It has also been mentioned that the resin edge treatment should aid the study of laminate defects. This, and potential extensions of the Python script, are also considered.

7.1.1 Refinement of Resin Edge Treatment

The resin treatment developed in Chapter 4 produced a significant improvement in CBS; however, it is believed this could be improved further by refining the treatment process. The surface of the CFRP free edge is currently polished to a fine level (as per the untreated specimens), before being plasma treated and the resin applied. It is thought a smooth surface finish to the CFRP edge is important to reduce the potential for seeding a defect. Although this certainly appears to be true for untreated laminates, whether this generates the strongest possible bond between the CFRP and resin edge for treated laminates has not been comprehensively studied. It is observed that resin often adheres better to rough surfaces; smooth moulds are used to assist the release of cured parts, i.e. to reduce the adhesion of resin material during manufacture. There is likely to be a balance between achieving good adhesion of the resin edge, and without seeding a defect at the CFRP edge. This could be verified by experimentally testing various surface finishes, both with and without subsequent plasma treatment. The strength of the laminate-resin edge bond could be tested using a setup similar to the example shown in Fig. 7.1, either under tension (as shown), shear or some combination.

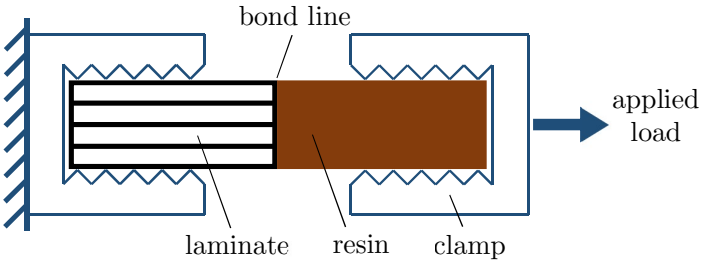

Figure 7.1 Experimental setup to test bond strength between CFRP edge and resin treatment under tension normal to CFRP edge.

The geometry of the resin edge could also be explored. Currently the resin extends down the limbs beyond the upper rollers of the 4-point bending test setup. In this way, the region that experiences the full corner unfolding moment (between the two upper rollers) is protected by resin. As noted in Section 5.3, the resin often debonds from the limbs of the L-shaped laminates during experimental testing, which is likely to alleviate bending stress in the resin edge. There is likely to be an optimum length that the resin treatment extends down the limbs of specimens: protecting the laminate, without attracting a high level of stress in the resin edge treatment. Currently the resin is also applied to the full thickness of the CFRP edge. However, laminates of a particular geometry and stacking sequence are frequently found to fail at particular ply/interface levels. It is possible that selectively applying the resin treatment to known failure locations would protect the CFRP edge sufficiently. This would also help to alleviate the amount of stress attracted by the resin edge treatment and reduce the cost of the treatment by saving resin material, which could become important if the treatment is used on an industrial scale.

7.1.2 Defect Analysis and Quantification

Identifying defects in composite materials and quantifying their effect on component performance is highly important. Due to the nature of the manufacturing process, no two laminates are identical. There will always be some level of voids, resin-rich zones, fibre wrinkles and waviness, tow gaps and overlaps etc. When these are large enough to cause a significant effect on laminate performance, they are typically deemed to be a defect. Small defects can also arise from in-service handling, such as barely visible impact damage (BVID), which has been the focus of many researchers. Testing the effect of defects on the strength of small specimens is challenging when free edges exist. In this case, the free edge often dominates failure rather than the defect. The resin

treatment developed in this thesis has the potential to facilitate testing of narrow specimens with centrally located defects, comparing them against pristine specimens. With the edge effect suppressed, the defect will dominate failure and give a clearer indication of its influence on laminate strength.

The wrinkles in laminates can be quantified by measuring the misalignment of plies against a nominal position. Using the contrast in optical properties between plies of different fibre orientation, lines that trace the plies around the curved section of the L-shaped specimens are generated. At intervals along the length of these lines, the alignment is compared against the nominal design alignment, i.e. the alignment if the specimen were pristine and without wrinkles. The measured misalignment is illustrated in Fig. 7.2 and can be used to quantify the level of ply wrinkling in a specimen.

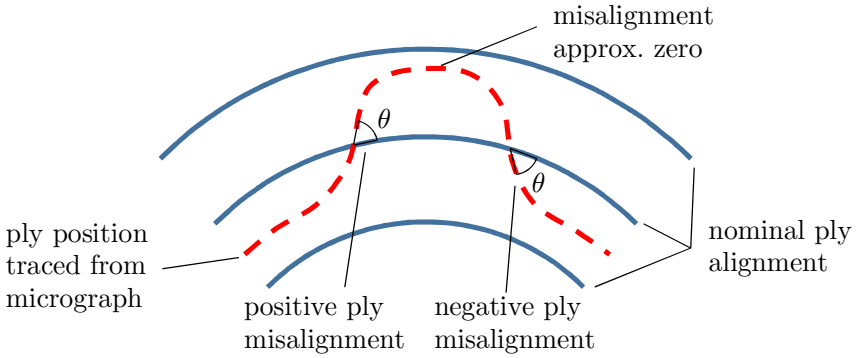

Figure 7.2 Illustration of ply misalignment. Note the peak of the wrinkle is parallel to the nominal alignment.

7.1.3 Extension of Python Script

In order to rapidly adapt the FE model properties, such as part geometry and stacking sequence, a Python script was developed and used to perform the analyses in Chapters 3, 4 and 5. However, this script is currently limited to pre-processing activities; post-processing to extract stresses is a manual process using the graphical user interface (GUI) of Abaqus. The script could be readily extended to extract the relevant stress results and input them into a failure criterion. Results, such as CBS and failure location, could then be printed in a text file for inspection. Removing dependence on the GUI would reduce computation time and the potential for human error if the analysis process was to be adopted by industry.

The use of a fully automated script also offers the potential for significant benefits when analysing a series of FE models, each with subtle variations in properties such defect geometry. It is possible to analyse one FE model with a certain defect, print the

results in a row of the output text file and then iterate the defect properties before adding another row of results in the text file. In this way, a study of the effect of various defect parameters could be rapidly generated. The effect of changing stacking sequence or part geometry could be analysed to assist designers when optimising components constructed from composite laminates.

References

[1] Maio L, Memmolo V, Ricci F, Boffa ND, Monaco E, Pecora R. Ultrasonic wave propagation in composite laminates by numerical simulation. Composite Structures 2015; 121: 64-74.

[2] The Boeing Company. (2008). Boeing 787 [online]. Available: http://www.boeing.com/ commercial/aeromagazine/articles/qtr_4_06/article_04_2.html.

[3] Airbus SAS. (2015). Technology [online]. Available: http://www.airbus.com/aircraftfamilies/passengeraircraft/a350xwbfamily/technology-and-innovation/.

[4] Sahadevan V, Stress Technical Authority, GKN Aerospace. Personal communication. 2016.

[5] Bartholomew P. Ply stacking sequence for laminate plates having in-plane and bending orthotropy. Fibre Science and Technology 1977; 10(4): 239-253.

[6] York CB. Coupled quasi-homogeneous orthotropic laminates. Mechanics of Composite Materials 2011; 47(4): 405-426.

[7] York CB. Characterization of non-symmetric forms of fully orthotropic laminates. Journal of Aircraft 2009; 46(4): 1114-1125.

[8] Vannucci P, Verchery G. A new method for generating fully isotropic laminates. Composite Structures 2002; 58(1): 75-82.

[9] Erland S, Dodwell TJ, Butler R. Characterisation of inter-ply shear in carbon fibre prepreg. Composites Part A: Applied Science and Manufacturing 2015; 77: 210-218.

[10] Larberg Y, Åkermo M. On the interply friction of different generations of carbon/epoxy prepreg systems. Compos Part A - Appl Sci Manuf 2011; 42(9): 1067-1074.

[11] Niu MC. Composite Airframe Structures. Hong Kong: Hong Kong Conmilit Press Ltd, 1992.

[12] Andrews ND. High speed demonstrator – passive (HSDP) design principles; for the smart sixed wing aircraft (SFWA) project. Technical report. Filton, United Kingdom. Airbus Operations Ltd, 2010.

[13] HEXCEL Corporation. HexPly 8552 epoxy matrix (180°C/356°F curing matrix) product data. 2013.

[14] European Aviation Safety Agency. (2016). The Agency [Online]. Available: https://www.easa.europa.eu/.

[15] Department for Defence, United States of America. Composite Materials Handbook MIL-HDBK-17-3F Volume 3 of 5. 2002.

[16] Jolly MR, Prabhakar A, Sturzu B, Hollstein K, Singh R, Thomas S, Foote P, Shaw A. Review of non-destructive testing (NDT) techniques and their applicability to thick walled composites. In: Proceedings of 4th International Conference on Through-life Engineering Services. Procedia CIRP 2015; 38: 129-136.

[17] Gholizadeh S. A review of non-destructive testing methods of composite materials. In: XV Portuguese Conference on Fracture. Procedia Structural Integrity 2016; 1: 50-57.

[18] Amenabar I, Mendikute A, López-Arraiza A, Lizaranzu M, Aurrekoetxea J. Comparison and analysis of non-destructive testing techniques suitable for delamination inspection in wind turbine blades. Composites Part B: Engineering 2011; 42(5): 1298-1305.

[19] Angioni SL, Ciampa F, Pinto F, Scarselli G, Almond DP, Meo M. An analytical model for defect depth estimation using pulsed thermography. Experimental Mechanics 2016; 56(6): 1111-1122.

[20] Krautkrämer J, Krautkrämer H. Ultrasonic Testing of Materials (4th edition). Springer-Verlag Berlin Heidelberg. 1990.

[21] Tan KT, Watanbe N, Iwahori Y. X-ray radiography and micro-computed tomography examination of damage characteristics in stitched composites subjected to impact loading. Composites Part B: Engineering 2011; 42(4): 874-884.

[22] American Society for Testing and Materials. ASTM D6415 / D6415M-06a, 2006. Standard test method for measuring the curved beam strength of a fiber-reinforced polymer-matrix composite.

[23] Jackson WJ, Ifju PG. Through-the-thickness tensile strength of textile composites. In: Deo RB, Saff CR, editors. Composite materials: testing and design, vol. 12, ASTM STP1274. Philadelphia: ASTM, 1996. p 218-238.

[24] Kedward KT, Wilson RS, McLean SK. Flexure of simply curved composite shapes. Composites 1989; 20(6): 527-536.

[25] Olsson R. A survey of test moethods for multiaxial and out-of-plane strength of composite laminates. Composites Science and Technology 2011; 71(6): 773-783.

[26] Uniform Building Code, 1982 Edition, International Conference of Building Officials, 5360 South Workman Mill Road, Whittier, California. p 205.

[27] Mabson GE, Neall EP. Analysis and testing of composite aircraft frames for interlaminar tension failure. National Specialist's Meeting on Rotary Wing Test Technology of the American Helicopter Society, Bridgeport, 1988.

[28] Kenward KT, Wilson RS, McLean SK. Flexture of simply curved composite shapes. Composites 1989; 20(6): 527-536.

[29] Ko WL. Delamination stresses in semicircular laminated composite bars. NASA Technical Memorandum 4026. 1988.

[30] Airbus UK Ltd. A400M spar development: inter-laminar shear and through-thickness direct stresses in laminated composites. 2004.

[31] Lekhnitskii, SG. Anisotropic Plates. New York: Gordon & Breach, 1968.

[32] Roymech. (2013). Curved Beams [Online]. Available: http://www.roymech.co.uk/Useful_Tables/Beams/Curved_beams.html.

[33] Yamada SE, Sun CT. Analysis of laminate strength and its distribution. J Compos Mater 1978; 12(3): 275-284.

[34] Kim RY, Soni SR. Experimental and analytical studies on the onset of delamination in laminated composites. J Compos Mater 1984;18(1):70-80.

[35] Roylance D. Transformation of stresses and strains. Massachusetts Institute of Technology, 2001.

[36] HEXCEL Corporation. HexPly M21 180°C (356°F) curing epoxy matrix product data. 2010.

[37] Berthe J, Deletombe E, Brieu M, Portemont G, Paulmier P. Dynamic characterization of CFRP composite materials – toward a pre-normative testing protocol – application to T700GC/M21 material. Procedia Eng 2014; 80: 165-182.

[38] Ersoy N, Garstka T, Potter K, Wisnom MR, Porter D, Clegg M, Stringer G. Development of the properties of a carbon fibre reinforced thermosetting composite through cure. Compos Part A - Appl Sci Manuf 2010; 41(3): 401-409.

[39] Sahadevan V, Stress Technical Authority, GKN Aerospace. Personal communication. 2015.

[40] Ankersen J, GKN Aerospace. Personal communication. 2015.

[41] Murthy PLN, Chamis CC. Free-edge delamination: laminate width and loading conditions effects. NASA Technical Memorandum 100238, 1987.

[42] Zienkiewicz OC, Taylor RL. The Finite Element Method (5^{th} edition) Volume 1: The Basics. Oxford, United Kingdom: Butterworth-Heinemann, 2000.

[43] Massachusetts Institute of Technology. (2014). Eight-node brick element [online]. Available: http://web.mit.edu/calculix_v2.7/CalculiX/ccx_2.7/doc/ccx/node26 .html.

[44] Prathap G. Finite Element Analysis as Computation. New Delhi, India, 2005.

[45] Massachusetts Institute of Technology. (2014). Eight-node brick element with reduced integration [online]. Available: http://web.mit.edu/calculix_v2.7/CalculiX/ccx_2.7/doc/ccx/node27.html.

[46] Livermore Software Technology Corporation. (2016). Hourglass [online]. Available: http://www.dynasupport.com/howtos/element/hourglass.

[47] Belytschko T, Ong JS-J, Liu WK, Kennedy JM. Hourglass control in linear and nonlinear problems. Computer Methods in Applied Mechanics and Engineering 1984; 43(3): 251-276.

[48] Schulz JC. Global mode hourglassing control. Computer Methods in Applied Mechanics and Engineering 1987; 64(1-3): 553-566.

[49] Esquej R, Castejon L, Lizaranzu M, Carrera M, Miravete A, Miralbes R. A new finite element approach applied to the free edge effect on composite materials. Compos Struct 2013; 98: 121-129.

[50] Raju IS, Crews JH. Interlaminar stress singularities at a straight free edge in composite laminates. Computers and Structures 1981; 14(1-2): 21-28.

[51] Dassault Systèmes Simulia Corp., Providence, USA. ABAQUS 6.12-3 User's Manual. 2012.

[52] Dassault Systèmes Simulia Corp., Providence, USA. ABAQUS 6.14 User's Manual. 2016.

[53] Fletcher TA, Reinarz AK, Dodwell TJ, Butler R, Scheichl R, Newley R. Efficient modelling and accurate certification of curved aerospace laminates. In: Proceedings of the 17th European Conference on Composite Materials, Munich, Germany, 26-30 June 2016.

[54] Tsai SW. Strength characteristics of composite materials. NASA CR-224, 1965.

[55] Tsai SW, Wu EM. A general theory of strength for anisotropic materials. Journal of Composite Materials 1971; 5(1): 58-80.

[56] Hashin Z. Failure criteria for unidirectional fibre composites. Journal of Applied Mechanics 1980; 47(2): 329-334.

[57] Cui WC, Wisnom MR, Jones M. A comparison of failure criteria to predict delamination of unidirectional glass/epoxy specimens waisted through the thickness. Composites 1992; 23(3): 158-166.

[58] Marklund E. Literature survey of 3D failure criteria. TR10-002. Swerea SICOMP AB, Piteå, Sweden. 2010.

[59] Eckold GC. Failure criteria for use in the design environment. Composites Science and Technology 1998; 58(7); 1095-1105.

[60] Hart-Smith LJ. Predictions of the original and truncated maximum-strain failure models for certain fibrous composite laminates. Composites Science and Technology 1998; 58(7): 1151-1178.

[61] Camanho PP. Failure criteria for fibre-reinforced polymer composites. Section of Applied Mechanics, Department of Mechanical Engineering and Industrial Management, Faculty of Engineering, University of Porto, 2002.

[62] Hinton MJ, Kaddour AS, Soden PD. Failure criteria in fibre reinforces polymer composites: the world-wide failure exercise. Elsevier 2004.

[63] Liu PF, Xing LJ, Zheng JY. Failure analysis of carbon fiber/epoxy composite cylindrical laminates using explicit finite element method. Composites Part B: Engineering 2014; 56: 54-61.

[64] Hallal A, Younes R. Improvement in failure prediction algorithm for textile composites. International Journal of Damage Mechanics, 5 July 2016.

[65] Hinton MJ, Soden PD. Predicting failure in composite laminates: the background to the exercise. Composites Science and Technology 1998; 58(7): 1001-1010.

[66] Hinton MJ, Kaddour AS, Soden PD. Predicting failure in fibre composites: lessons learned from the word-wide failure exercise. In: Proceeding of the 13th International Conference on Composite Materials (ICCM13), Beijing, China, 25-29 June 2001. Paper 1198.

[67] Sun CT, Quinn BJ, Tao J, Oplinger DW. Comparative Evaluation of Failure Analysis Methods for Composite Laminates. NASA, DOT/FAA/AR-95/109, 1996.

[68] González-Cantero JM, Graciani E, París F, López-Romano B. Stacking sequence optimization of curved UD-CFRP laminates for improving unfolding strength considering thermal residual stresses. In: Proceedings of the 17th European Conference on Composite Materials (ECCM17), Munich, Germany, 26-30 June 2016.

[69] Camanho PP, Dávila CG, De Moura MF. Numerical simulation of mixed-mode progressive delamination in composite materials. Journal of Composite Materials 2003; 37(16): 1415-1438.

[70] Bower AF. (1997). EN224 Linear Elasticity [online]. Brown University. Available: https://www.brown.edu/Departments/Engineering/Courses/EN224/anis_general/anis_general.htm.

[71] FEI Visualization Sciences Group. Avizo 8 User's Manual. 2013.

[72] Mittelstedt C, Becker W. Free-edge effects in composite laminates. Appl Mech Rev 2007; 60(5): 217-245.

[73] Kant T, Swaminathan K. Estimation of transversely inter-laminar stresses in laminated composites – a selective review and survey of current developments. Compos Struct 2000; 49(1): 65-75.

[74] Andakhshideh A, Tahani M. Free-edge stress analysis of general rectangular composite laminates under bending, torsion and thermal loads. Eur J Mech A-Solids 2013; 42: 229-240.

[75] Helenon F, Wisnom MR, Hallet SR, Allegri G. An approach for dealing with high local stresses in finite element analyses. Compos Part A - Appl Sci Manuf 2010; 41(9): 1156-1163.

[76] Panigrahi SK, Pradhan B. Delamination damage analyses of FRP composite spar wingskin joints with modified elliptical adhesive load coupler profile. Appl Compos Mater 2008; 15(4): 189-205.

[77] Vidal P, Gallimard L, Polit O. Assessment of variable separation for finite element modelling of free edge for composite plates. Compos Struct 2015; 123: 19-29.

[78] Lessard LB, Schmidt AS, Shokrieh MM. Three-dimensional stress analysis of free-edge effects in a simple composite cross-ply laminate. International Journal on Solids and Structures 1996; 33(15): 2243-2259.

[79] Datoo MH. Interlaminar stresses – free edge effects. In: Design of thin walled composite sections, (IGDS module SA.1, Aerospace Composites Design). London South Bank University, 11-15 September 1995.

[80] Kim RY. Prevention of free-edge delamination. In: Proceedings of the 28th National SAMPE Symposium and Exhibition, Azusa, 12-14 April 1983. p. 200-209.

[81] Heyliger PR, Reddy JN. Reduction of free edge stress concentration. J Appl Mech 1983; 52: 801-805.

[82] Howard WE, Gossard Jr T, Jones RM. Composite laminate free-edge reinforcement with U-shaped caps. Part I: Stress analysis. AIAA J 1989; 27: 610-616.

[83] Howard WE, Gossard Jr T, Jones RM. Composite laminate free-edge reinforcement with U-shaped caps. Part II: Theoretical-experimental correlation. AIAA J 1989; 27: 617-623.

[84] Vizzini AJ. Prevention of free-edge delamination via edge alteration. Paper no. 88-2258. In: Proceedings of the AIAA/ASME/ASCE/AHS 29th Structures, Structural Dynamics and Materials Conference, Williamsburg, April 18-20 1988. p. 365-370.

[85] Mignery LA, Tan TM, Sun CT. The use of stitching to suppress delamination in laminated composites. ASTM Symposium on delamination and debonding of materials. In: Proceedings of ASTM STP 876, American Society for Testing and Materials, Pittsburgh, 1985, p. 371-385.

[86] W.S. Chan, C. Rogers, S. Aker. Improvement of edge delamination strength of composite laminates using adhesive layers. Composite materials: testing and design (7th conference). In: Proceedings of ASTM STP 893, American Society for Testing and Materials, Philadelphia, 1986, p. 265-285.

[87] Chan WS, Rogers C, Cronkhite JD, Martin J. Delamination control of composite rotor hubs. J Am Helicopter Soc 1986; 31(3): 60-69.

[88] Shiau L-C, Chue Y-H. Free edge stress reduction through fibre volume fraction variation. Compos Struct 1991; 19(2): 145-165.

[89] Resinlab LLC. Technical data sheet EP1330 & EP1330LV. 2010.

[90] Olsson R. Analytical prediction of damage due to large mass impact on thin ply composites. Composites Part A: Applied Science and Manufacturing 2015; 72: 184-191.

[91] Kaddour AS, Hinton MJ. Input data for test cases used in benchmarking triaxial failure theories of composites. Journal of Composite Materials 2012; 46(19-20): 2295-2312.

[92] Makeev A, Seon G, Nikishkov Y, Lee E. Methods for assessment of interlaminar tensile strength of composite laminates. Journal of Composite Materials 2015; 49(7): 783-794.

[93] National Institute for Aviation Research. Hexcel 8552 AS4 unidirectional prepreg at 190 gsm & 35% RC qualification material property data report. FAA special project number SP46114WI-Q. NCAMP test report number CAM-RP-2010-002 Rev A. 2011.

[94] Dávila CG, Camanho PP, Rose CA. Failure criteria for FRP laminates. Journal of Composite Materials 2005; 39(4): 323–45.

[95] Pinho ST, Dávila CG, Camanho PP, Iannucci L, Robinson P. Failure Models and Criteria for FRP Under In-Plane or Three-Dimensional Stress States Including Shear Non-Linearity. NASA/TM-2005-213530. NASA Langley Research Center. Hampton, VA 2368. 2005.

[96] Pinho ST, Iannucci L, Robinson P. Physically-based failure models and criteria for laminated fibre-reinforced composites with emphasis on fibre kinking: Part I: development. Composites Part A: Applied Science and Manufacture 2006; 37(1): 63-73.

[97] Puck A, Schürmann H. Failure analysis of FRP laminates by means of physically based phenomenological models. Composites Science and Technology 1998; 58(7): 1045-1067.

[98] HEXCEL Corporation. HexPly M21 epoxy matrix (180°C/356°F curing matrix) product data. 2007.

[99] Ye J, Zhang D. Prediction of failure envelopes and stress-strain curves of fiber composite laminates under triaxial loads. Journal of Composite Materials 2012; 46(19-20): 2417-2430.

[100] Christensen RM. Stress based yield/failure criteria for fiber composites. International Journal of Solids and Structures 1997; 34(5): 529-543.

[101] Christensen RM. (2008). Failure criteria for anisotropic fiber composite materials [online]. Available: http://www.failurecriteria.com/Media/Failure_ Criteria_for _Anisotropic_Fiber_Composite_Materials.pdf.

[102] Resinlab LLC. Technical data sheet EP950G gray. 2012.

[103] Abdi F, Surdenas J, Munir N, Housner J, Keshavanarayana R. Virtual Testing and Predictive Modeling, Chapter 6: Computational Approach Toward Advanced Composite Material Qualification and Structural Certification. USA: Springer, 2009. p 137.

[104] Alpha STAR Corporation. (2008). A novel approach to determine A- and B-basis allowables for composite materials [online]. Available: http:// www.ascgenoa.com/newsletter/12/index.jsp.

[105] Caddell RM, Raghava RS, Atkins AG. A yield criterion for anisotropic and pressure dependent solids such as oriented polymers. Journal of Materials Science 1973; 8(11): 1641-1646.

[106] Camanho PP, Dávila CG, Pinho ST, Iannucci L, Robinson P. Prediction of in situ strengths and matrix cracking in composites under transverse tension and in-plane shear. Composites Part A: Applied Science and Manufacturing 2006; 37(2): 165-176.

[107] Sebaey TA, Costa J, Maimi P, Batista Y, Blanco N, Mayugo JA. Measurement of the in situ transverse tensile strength of composite plies by means of the real time monitoring of microcracking. Composites Part B: Engineering 2014; 65: 40-46.

Appendices

Appendix A: Proofs for Chapter 2

This appendix provides a complete list of calculation steps for equations derived in Chapter 2.

The calculation steps for Eq. (2.10) are

$$\frac{1}{3}\Big({z_k}^3 - {z_{k-1}}^3 \Big) = \frac{1}{12}\Big(4{z_k}^3 - 4{z_{k-1}}^3 \Big)$$

$$= \frac{1}{12}\Big(3{z_k}^3 + 3{z_k}^2 z_{k-1} - 3z_k\ {z_{k-1}}^2 - 3{z_{k-1}}^3 \Big)$$
$$+ \frac{1}{12}\Big({z_k}^3 - 3{z_k}^2 z_{k-1} + 3z_k\ {z_{k-1}}^2 - {z_{k-1}}^3 \Big)$$

$$= \Big(z_k - z_{k-1} \Big)\Big(\frac{{z_k}^2 + 2z_k\ z_{k-1} + {z_{k-1}}^2}{4} \Big) \tag{A.1}$$
$$+ \frac{1}{12}\Big(z_k - z_{k-1} \Big)\Big({z_k}^2 - 2z_k\ z_{k-1} + {z_{k-1}}^2 \Big)$$

$$= \Big(z_k - z_{k-1} \Big)\Big(\frac{z_k + z_{k-1}}{2} \Big)^2 + \frac{1}{12}\Big(z_k - z_{k-1} \Big)^3$$

$$= t_k\ {\bar{z}_k}^2 + \frac{{t_k}^3}{12} \quad .$$

The calculation steps for Eq. (2.29) are

$$
\begin{aligned}
\varepsilon &= \frac{l_{post}}{l_{pre}} - 1 \\
&= \frac{\sqrt{{l_r}^2 + \left(y'_f - y'_p\right)^2}}{\sqrt{{l_r}^2 + (y_f - y_p)^2}} - 1 \\
&= \frac{\sqrt{{l_r}^2 + \left(\Delta t + \rho t_f(1-c) - \rho t_p(1-c)\right)^2}}{\sqrt{{l_r}^2 + (\Delta t + \rho t_f - \rho t_p)^2}} - 1 \\
&= \frac{\sqrt{{l_r}^2 + \left(\Delta t + \rho(1-c)(t_f - t_p)\right)^2}}{\sqrt{{l_r}^2 + \left(\Delta t + \rho(t_f - t_p)\right)^2}} - 1 \\
&= \frac{\sqrt{{l_r}^2 + \left(\Delta t + \rho(1-c)(-\Delta t)\right)^2}}{\sqrt{{l_r}^2 + \left(\Delta t + \rho(-\Delta t)\right)^2}} - 1 \\
&= \frac{\sqrt{{l_r}^2 + \left(\Delta t\big(1 - \rho(1-c)\big)\right)^2}}{\sqrt{{l_r}^2 + \left(\Delta t(1-\rho)\right)^2}} - 1 \\
&= \frac{\sqrt{{l_r}^2 + \left(\Delta t(1 - \rho + \rho c)\right)^2}}{\sqrt{{l_r}^2 + \left(\Delta t(1-\rho)\right)^2}} - 1 \quad .
\end{aligned}
\tag{A.2}
$$

The calculation steps for Eq. (2.31) are

$$
\begin{aligned}
\varepsilon &= \frac{\sqrt{(R\Delta t)^2 + \left(\Delta t(1 - \rho + \rho c)\right)^2}}{\sqrt{(R\Delta t)^2 + \left(\Delta t(1-\rho)\right)^2}} - 1 \\
&= \frac{\sqrt{R^2\Delta t^2 + \Delta t^2(\ 1 - \rho + \rho c\ )^2}}{\sqrt{R^2\Delta t^2 + \Delta t^2(\ 1-\rho\ )^2}} - 1 \\
&= \frac{\sqrt{\Delta t^2(R^2 + (\ 1 - \rho + \rho c\ )^2\ )}}{\sqrt{\Delta t^2(R^2 + (1-\rho)^2\ )}} - 1 \\
&= \frac{\sqrt{R^2 + (\ 1 - \rho + \rho c\ )^2}}{\sqrt{R^2 + (\ 1-\rho\ )^2}} - 1 \quad .
\end{aligned}
\tag{A.3}
$$

Appendix B: Experimental Test Results

This appendix contains detailed tables of results for each individual curved laminate test specimen (Tables B.1 through B.14).

Specimen ID	CBS (kNmm/mm)	Failure location
G39A-01	8.08	ply 17-38
G39A-02	7.89	ply 17-38
G39A-03	7.60	ply 16-37
Average	7.86	-
S.D.	0.20	-

Table B.1 G39A test specimen results.

Specimen ID	CBS (kNmm/mm)	Failure location
G39B-01	7.56	ply 16-38
G39B-02	7.19	ply 17-37
G39B-03	7.71	ply 23-38
Average	7.49	-
S.D.	0.22	-

Table B.2 G39B test specimen results.

Specimen ID	CBS (kNmm/mm)	Failure location
S24-01	2.09	ply 1-3
S24-02	2.00	ply 3-4
S24-03	1.86	ply 3-4
S24-04	1.78	ply 1-3
S24-05	2.03	ply 8-24
S24-06	2.02	ply 7-24
S24-07	2.07	ply 4-24
S24-08	2.13	ply 7-24
S24-09	2.00	ply 3-24
S24-10	2.07	ply 1-9
S24-11	2.30	ply 8-24
S24-12	2.13	ply 3-4
Average	2.04	-
S.D.	0.12	-

Table B.3 S24 test specimen results.

Specimen ID	CBS (kNmm/mm)	Failure location
S44-01	4.06	ply 22-42
S44-02	4.13	ply 22-42
S44-03	4.19	ply 24-44
S44-04	4.62	ply 34-44
S44-05	4.40	ply 18-44
Average	4.28	-
S.D.	0.20	-

Table B.4 S44 test specimen results.

Specimen ID	CBS (kNmm/mm)	Failure location
N24-01	1.76	ply 1-8
N24-02	1.54	ply 3-4
N24-03	1.77	ply 3-4
N24-04	1.72	ply 1-4
N24-05	1.90	ply 3-4
N24-06	1.88	ply 1-4
N24-07	2.02	ply 1-4
N24-08	1.78	ply 2-4
N24-09	1.77	ply 1-3
N24-10	1.71	ply 3-4
N24-11	1.68	ply 1-4
N24-12	1.96	ply 1-4
N24-13	2.13	ply 1-3
Average	1.82	-
S.D.	0.15	-

Table B.5 N24 test specimen results.

Specimen ID	CBS (kNmm/mm)	Failure location
N44-01	3.68	ply 28-36
N44-02	3.15	ply 30-36
N44-03	4.36	ply 29-36
N44-04	3.99	ply 29-36
Average	3.79	-
S.D.	0.45	-

Table B.6 N44 test specimen results.

Specimen ID	CBS (kNmm/mm)	Failure location
G39B(R)-01	8.70	ply 3-36
G39B(R)-02	8.60	ply 3-36
G39B(R)-03	8.66	ply 3-36
Average	8.65	-
S.D.	0.04	-

Table B.7 G39B(R) test specimen results.

Specimen ID	CBS (kNmm/mm)	Failure location
S24(R)-01	2.32	ply 1-24
S24(R)-02	2.16	ply 8-24
S24(R)-03	2.43	ply 1-3
Average	2.30	-
S.D.	0.11	-

Table B.8 S24(R) test specimen results.

Specimen ID	CBS (kNmm/mm)	Failure location
S44(R)-01	4.66	internal
S44(R)-02	5.29	ply 30-44
S44(R)-03	5.75	ply 24-44
Average	5.23	-
S.D.	0.45	-

Table B.9 S44(R) test specimen results.

Specimen ID	CBS (kNmm/mm)	Failure location
N24(R)-01	1.93	ply 3, int. 3
N24(R)-02	2.07	ply 9-24
N24(R)-03	1.94	ply 1-5
N24(R)-04	2.03	ply 1-21
N24(R)-05	2.02	ply 3, int. 3
Average	2.00	-
S.D.	0.05	-

Table B.10 N24(R) test specimen results.

Specimen ID	CBS (kNmm/mm)	Failure location
N44(R)-01	3.86	ply 28-37
N44(R)-02	3.94	ply 26-37
N44(R)-03	3.98	ply 28-36
N44(R)-04	3.90	ply 28-37
Average	3.92	-
S.D.	0.04	-

Table B.11 N44(R) test specimen results.

Specimen ID	CBS (kNmm/mm)	Failure location
G64-01	15.6	ply 29-64
G64-02	15.7	ply 45-64
G64-03	12.6	ply 33-39
Average	14.6	-
S.D.	1.43	-

Table B.12 G64 test specimen results (no resin treatment).

Specimen ID	CBS (kNmm/mm)	Failure location
G64(1330LV)-01	13.4	ply 3-56
G64(1330LV)-02	15.0	ply 3-55
G64(1330LV)-03	17.2	ply 32-44
Average	15.2	-
S.D.	1.54	-

Table B.13 G64(1330LV) test specimen results.

Specimen ID	CBS (kNmm/mm)	Failure location
G64(950G)-01	16.4	ply 32-61
G64(950G)-02	14.9	ply 23-61
G64(950G)-03	17.5	ply 22-37
Average	16.3	-
S.D.	1.04	-

Table B.14 G64(950G) test specimen results.